



**NTNU – Trondheim**  
Norwegian University of  
Science and Technology

# Sulfide Stress Corrosion Cracking Resistance of Modified ASTM A694 F60 Low Alloy Steel for Subsea Applications

**Camilla A Stridsklev**

Materials Technology

Submission date: June 2013

Supervisor: Jan Ketil Solberg, IMTE

Co-supervisor: Roy Johnsen, IPM  
Torstein Lange, SINTEF

Norwegian University of Science and Technology  
Department of Materials Science and Engineering



## **Preface**

This project was initiated by GE Oil & Gas in Sandvika, in conjunction with the master thesis in the course TMT 4905, at Department of materials science and engineering at the Norwegian University of Science and Technology (NTNU). This master thesis is the sequel of a project work, which was carried through during the fall 2012, in which impact toughness and microstructure of a modified F60 steel was investigated and documented. The aim of this study has been to characterize the SSC resistance of the same two low alloy steels used in hub connectors subsea.

The supervisor and co-supervisor at NTNU for this thesis has been Professor Jan Ketil Solberg and Professor Roy Johnsen, co-supervisor at SINTEF was Research Scientist Torstein Lange. I would like to thank them all for follow-up, feedback and helpful discussions. I would especially like to thank Torstein Lange for extensive assistance in the laboratory. Thanks to Nils-Inge Nilsen at SINTEF for assistance in the laboratory and Robert Karlsen at the engineering workshop at the Faculty of Natural Sciences and Technology at NTNU for all the help regarding machining of specimens. I would also like to thank SINTEF for performing the tensile tests.

In GE Oil & Gas I would like to thank Atle Helge Qvale and Fredrik Rosenqvist for making this project possible and for feedback and discussions.

Trondheim, 20.06.2013

---

Camilla Abelsen Stridsklev



## Abstract

The resistance to sulfide stress corrosion cracking (SSC) of modified ASTM A694 F60 low alloy steel, produced by two different manufacturers, was studied by four-point bend-testing. The two materials are named material A and material B in this report. Both materials were tested in two different environments with different severity, one “sweet-transition region” test and one “sour service” test. The test conditions were controlled by the H<sub>2</sub>S partial pressure (pH<sub>2</sub>S) and pH. These parameters were varied in the two tests. Resistance to SSC was investigated on the base materials and on thermally weld-simulated and notched materials. The thermal weld simulation was performed to provide an intercritically reheated CGHAZ, leading to a microstructure containing brittle constituents. The tests were performed in autoclaves at room temperature with a pressure of 10 bars.

The microstructure and Vickers hardness (HV) of both base materials and the heat-affected zones (HAZ) were studied as these parameters affect the SSC susceptibility. The hardness of material B is higher than of material A, being respectively 249±2 HV and 214±5 HV. The hardness of the simulated HAZ of the two materials were similar, both reaching 400 HV. The microstructure of base material A mainly consists of bainite and ferrite/pearlite while material B mainly consists of acicular ferrite and bainite. The microstructure of the intercritically reheated CGHAZ is characterized by bainite laths inside large prior austenite grains. At the grain boundaries, M-A constituents had crown in a “necklace” formation.

The base materials did not reveal cracking in the sweet-transition test, however, localized corrosion caused by CO<sub>2</sub> and H<sub>2</sub>S was found along the stressed side of the specimens. Base material B was more severely attacked than material A, based on the depth and density of the corrosion pits. In the “sour service” test, severe general and localized corrosion and cracking were observed in both base materials. The materials are therefore considered unsuitable for “sour service” applications.

In the HAZ specimens, of both material A and B, severe cracking was observed in both tests. The specimens were fully separated by cracking in the “sour service” test. The welded materials are therefore considered highly susceptible to SSC when a notch exists in the intercritically reheated CGHAZ. The HAZ hardness is higher than the maximum hardness requirement for SSC resistance according to ISO 15156-2. It would therefore be beneficial to perform additional testing of the HAZ, with hardness levels within the requirements.

The cracking appeared as transgranular and was often initiated at the prior austenite grain boundaries, near the M-A constituents in the HAZ.



## Sammendrag

Motstand mot sulfid spenningskorrosjon (SSC) til to modifiserte ASTM A694 F60 lavlegerte stål ble undersøkt ved firepunkts bøyetesting. De to materialene er navngitt material A og material B i rapporten. Begge materialene ble testet i to ulike miljø med ulik alvorlighetsgrad. En relativt mild test og en «sur service» test ble gjennomført. Testforholdene ble bestemt og kontrollert ut i fra partialtrykket til H<sub>2</sub>S (pH<sub>2</sub>S) i testgassen og pH i løsningen, disse parameterne var ulike i de to testene. Motstanden mot sulfid spenningskorrosjon ble testet både på grunnmaterialene og på sveisesimulert materiale med ilagt kjerv. Testene ble gjennomført i ved 10 bar trykk i autoklav ved romtemperatur.

Mikrostruktur og Vickers hardhet (HV) til materialene, både grunnmaterialer og varmpåvirket sone, ble studert for å gi informasjon om materialfaktorer som påvirker SSC motstanden. Hardheten til grunnmateriale B er høyere enn for grunnmateriale A og hardhetsverdiene er henholdsvis 249±2 HV og 214±5 HV. Hardheten i den varmpåvirkede sonen er lik for begge materialene og når et maksimum over 400 HV i senter av den varmpåvirkede sonen. Mikrostrukturen i grunnmateriale A består hovedsakelig av bainitt og ferritt/perlitt, mens mikrostrukturen i grunnmateriale B består av asikulær ferritt og bainitt. Sveisesimuleringen ble gjennomført slik at man oppnådde interkritisk gjentatt oppvarming av den grovkornede varmpåvirkede sonen. Mikrostrukturen i den varmpåvirkede sonen i begge materialene består av bainitt i store tidligere austenittkorn. M-A faser har blitt dannet langs de tidligere austenittkorngransene.

Grunnmaterialene var ikke utsatt for oppsprekking i den milde testen, men lokal korrosjon som skyldes CO<sub>2</sub> og H<sub>2</sub>S ble observert langs den nedbøyde siden av prøven. Basert på antallet og lengden på angrepene regnes grunnmateriale B som mer utsatt for CO<sub>2</sub>/H<sub>2</sub>S korrosjon enn grunnmateriale A. I «sur service» testen ble begge materialene utsatt for stor grad av generell og lokal CO<sub>2</sub>/H<sub>2</sub>S korrosjon og oppsprekking grunnet sulfid spenningskorrosjon. Grunnmaterialene er på grunnlag av disse observasjonene regnet som uegnet for «sur service» anvendelser.

Testingen av varmpåvirket sone viste at begge materialene er utsatt for sulfid spenningskorrosjon i begge miljøene. I «sur service» testen ble prøvene fullstendig separert grunnet oppsprekking. De sveisesimulerte materialene er derfor regnet om svært utsatt for SSC dersom et kjerv, eller tilsvarende sveisefeil, eksisterer i den interkritisk gjentatt oppvarmede CGHAZ. Hardheten til den varmpåvirkede sonen ligger langt over kravet til maksimal hardhet for SSC motstand. Det vil være en fordel å utføre ytterligere testing av varmpåvirket sone med hardhet innenfor kravene.

Transkrystallinsk sprekkvekst var dominerende for begge materialene. Korrosjonsangrepene og sprekke i varmpåvirket sone var ofte initiert ved de tidligere austenittkorngransene på M-A faser.





# List of Content

|   |            |
|---|------------|
| <b>Preface</b> .....  | <b>I</b>   |
| <b>Abstract</b> .....   | <b>III</b> |
| <b>Sammendrag</b> .....   | <b>V</b>   |
| <b>List of Content</b> .....  | <b>VII</b> |
| <b>List of Abbreviations</b> .....                                    | <b>XI</b>  |
| <b>1. Introduction</b> .....  | <b>1</b>   |
| <b>2. Theory</b> .....  | <b>3</b>   |
| 2.1. H <sub>2</sub> S corrosion.....                                  | 3          |
| 2.2. Stress corrosion cracking.....                                   | 4          |
| 2.3. Sulfide stress corrosion cracking .....                          | 4          |
| 2.4. Factors affecting sulfide stress corrosion cracking.....         | 5          |
| 2.4.1. Environmental factors.....                                     | 5          |
| 2.4.2. Metallurgical factors.....                                     | 7          |
| 2.5. Welding of low-alloy steel .....                                 | 8          |
| 2.5.1. Microstructural changes during welding .....                   | 8          |
| 2.5.2. Weld defects .....   | 11         |
| <b>3. Experimental methods</b> .....                                  | <b>13</b>  |
| 3.1. ASTM A694 F60 low alloy steel.....                               | 13         |
| 3.2. Modifications for the oil and gas industry .....                 | 13         |
| 3.3. Specimen sampling.....   | 14         |
| 3.4. Tensile test.....  | 16         |
| 3.5. Thermal weld simulation .....                                    | 17         |
| 3.6. Testing of resistance to sulfide stress corrosion cracking ..... | 19         |
| 3.6.1. Four point bend test .....                                     | 19         |
| 3.7. Vickers hardness testing .....                                   | 27         |
| 3.8. Micro-hardness testing .....                                     | 28         |
| 3.9. Microstructure characterization .....                            | 28         |
| <b>4. Results</b> .....   | <b>29</b>  |
| 4.1. Tensile properties .....   | 29         |
| 4.2. Microstructure characterization .....                            | 31         |

|           |  |           |
|-----------|--|-----------|
| 4.2.1.    | Microstructure of base materials .....                   | 31        |
| 4.2.2.    | Microstructure of the heat-affected zone.....            | 33        |
| 4.3.      | Hardness measurements .....                              | 35        |
| 4.3.1.    | Vickers hardness of base materials.....                  | 35        |
| 4.3.2.    | Vickers hardness profile of the heat-affected zone ..... | 36        |
| 4.3.3.    | Micro-hardness measurements .....                        | 36        |
| 4.4.      | Sulfide stress corrosion cracking.....                   | 37        |
| 4.4.1.    | Test 1: Sweet - Transition zone .....                    | 38        |
| 4.4.2.    | Test 2: Sour service region .....                        | 44        |
| <b>5.</b> | <b>Discussion .....</b>                                  | <b>55</b> |
| 5.1.      | General discussion.....                                  | 55        |
| 5.1.1.    | Yield point phenomena.....                               | 55        |
| 5.1.2.    | Hardness .....   | 55        |
| 5.2.      | SSC resistance .....                                     | 56        |
| 5.2.1.    | Base materials.....                                      | 56        |
| 5.2.2.    | Heat-affected zone .....                                 | 57        |
| 5.3.      | Fracture morphology .....                                | 58        |
| 5.4.      | Effect of various factors on SSC resistance.....         | 58        |
| 5.4.1.    | Hardness and strength.....                               | 58        |
| 5.4.2.    | Microstructure .....                                     | 59        |
| 5.4.3.    | Stress level.....  | 60        |
| 5.4.4.    | Environmental parameters .....                           | 60        |
| 5.4.5.    | Other factors .....                                      | 61        |
| <b>6.</b> | <b>Conclusions.....</b>                                  | <b>63</b> |
| <b>7.</b> | <b>References.....</b>                                   | <b>65</b> |

**Appendix A: Achieved Strains Recorded by Extensometer**

**Appendix B: Test Gas Certificates**

**Appendix C: pH Calibration Curve for SSC Test 2**

**Appendix D: Stress-Strain Curves from Tensile Testing**

**Appendix E: Results from Vickers Hardness Measurements**

**Appendix F: Macro Photos of Cracked Specimens**

**Appendix G: Micrographs of All SSC Specimens, Test 1 and 2**



## List of Abbreviations

|                             |   |
|-----------------------------|---|
| AYS                         | Actual Yield Strength                             |
| CE                          | Carbon Equivalent                                 |
| CGHAZ                       | Coarse Grained HAZ                                |
| EFC                         | European Federation of Corrosion Publications     |
| FPB                         | Four-Point Bend (test)                            |
| F60                         | Forged steel grade, minimum yield strength 60 ksi |
| GB                          | Grain Boundary                                    |
| HAZ                         | Heat-Affected Zone                                |
| HIC                         | Hydrogen Induced Cracking                         |
| ICCGHAZ                     | Intercritical Coarse Grained HAZ                  |
| LBZ                         | Local Brittle Zones                               |
| P <sub>H<sub>2</sub>S</sub> | Partial Pressure of H <sub>2</sub> S              |
| SCC                         | Stress Corrosion Cracking                         |
| SMYS                        | Specified Minimum Yield Strength                  |
| SSC                         | Sulfide Stress Corrosion Cracking                 |

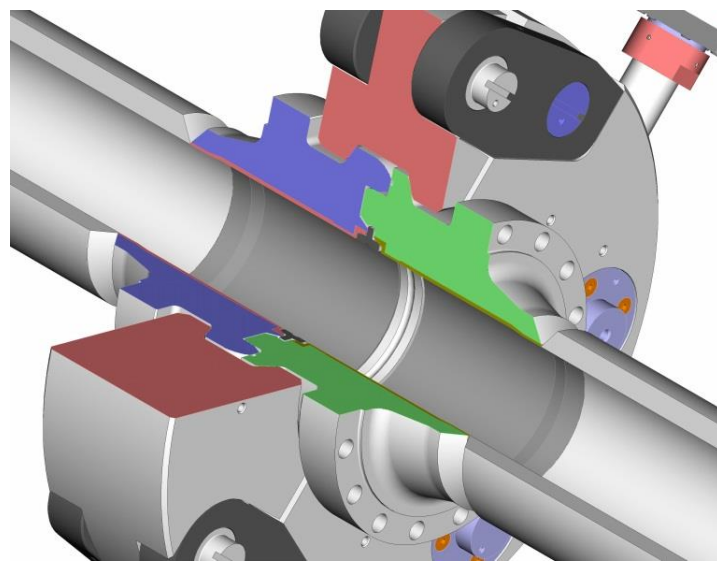
### Microstructure constituents

|     |                      |
|-----|----------------------|
| AF  | Acicular Ferrite     |
| B   | Bainite              |
| EF  | Equiaxed Ferrite     |
| M-A | Martensite-Austenite |
| P   | Pearlite             |



# 1. Introduction

As the exploration of new oilfields at deep water increase, oil companies are looking at subsea installation developments to substitute fixed platforms. The subsea installations are placed on the seabed and they are tied up to process facilities located on floating installations, existing platforms or onshore. From the seabed, the oil and gas produced are transported through pipelines to the process facilities. The pipelines are connected to the subsea installation through a connection system that consists of two flanges, the male and female. These are also known as hub connectors. The female and male hubs are made up mechanically by a clamp connector, with a metal seal ring between, to assure proper sealing. Figure 1 illustrates a cross-section of the female and male hubs, including the clamp connector.



**Figure 1: Cross section of a connection system showing female (blue) and male (green) hubs, and clamp connector (red). [Provided by GE Oil&Gas]**

A hub connector is an essential and critical item in a subsea installation. Hubs are forged to shape and manufactured in low alloy steels according to ASTM A694 F60 (later called F60) with a modified chemistry. The F60 steel is a bainitic low alloy steel with good strength-toughness balance. These steels require modifications such as control of cooling conditions, decrease of carbon content and increase of alloying elements to obtain high toughness. Subsea components, such as hub connectors are exposed to seawater on the outside and well fluid on the inside. The well fluid contains corrosive species like  $\text{CO}_2$  and  $\text{H}_2\text{S}$ .  $\text{H}_2\text{S}$  and  $\text{CO}_2$  are dissolved in aqueous environments to form acidic, corrosive solutions, usually referred to as sour service. Sulfide stress corrosion cracking (SSC) may occur in  $\text{H}_2\text{S}$  containing environments when a tensile stress is present and is a phenomenon of particular concern for the oil and gas industry. Failure by SSC, in  $\text{H}_2\text{S}$  containing oil and gas production environments, poses a risk to the environment, the equipment and to the health and safety of the personnel and the public. Resistance to SSC is therefore required for steels in these

applications. However, it is difficult to reach high strength, good toughness and adequate resistance to SSC, since the SSC resistance of steels decreases with increasing strength. As the conditions in the piping systems for oil and gas production are becoming increasingly sour, due to increasing H<sub>2</sub>S content, SSC is one of the major failure problems that occur in steels in oil and gas production systems. Depending on the temperature, pressure and pH of the environment, aqueous environments containing H<sub>2</sub>S and CO<sub>2</sub> is aggressive to carbon and low-alloy steels by causing severe cracking. The cracking process is very rapid and may cause catastrophic failure. [1-7]

This thesis was established to investigate the SSC resistance of modified ASTM A694 F60 low alloy steel forgings, from two independent manufacturers. The tests were performed according to the standards “ISO 15156: Petroleum and Natural Gas Industries – Materials for use in H<sub>2</sub>S-Containing Environments in Oil and Gas Production, Part 2: Cracking-Resistant Carbon and Low-Alloy Steels, and the use of Cast Irons”, and “NACE TM0177: Laboratory Testing of Metals for Resistance to Sulfide Stress Cracking in H<sub>2</sub>S Environments” and the European Federation of Corrosion Publications (EFC) number 16 “Guidelines on Materials Requirements for Carbon and Low Alloy Steels for H<sub>2</sub>S-Containing Environments in Oil and Gas Production”. The test specimens were machined from positions as close to the inner surface of the hub connectors as possible to investigate the properties of the material subjected to the well-fluids. The testing was conducted in environments with different severity, by varying the pH and the H<sub>2</sub>S partial pressure (pH<sub>2</sub>S), to study the resistance of the steels to SSC. The two environments tested in this project represent the transition between the sweet region and the transition zone, named “test 1” in the report, and the sour service region test, named “test 2” in the report. ISO 15156-2 provides requirements for selection and classification of carbon and low alloy steels for service in H<sub>2</sub>S containing oil and natural gas production and treatment environments. The requirements and recommendations in the standard can be applied to avoid costly corrosion and cracking damage on the equipment.

The purpose of the thermal weld simulations was to obtain a microstructure containing brittle phases. The thermal weld simulations were performed in two cycles, where the second cycle provided an intercritical reheating of the coarse grained HAZ produced by the first thermal weld cycle. The microstructure in the HAZ of the specimens tested in this work provides a “worst case” simulated weld. The hardness of this HAZ region is high which is conflicting with the hardness requirements for SSC resistance which will be discussed in the report.



## 2. Theory

### 2.1. H<sub>2</sub>S corrosion

Corrosion in aqueous hydrogen sulfide (H<sub>2</sub>S) containing environments is a result of an electrochemical reaction, equation 4, between the metal (Fe) and the corrosive medium (H<sub>2</sub>S). The anodic iron reaction (equation 1) and the cathodic hydrogen sulfide reactions (equation 2 and 3) contribute to the net H<sub>2</sub>S reaction. In the net H<sub>2</sub>S reaction, FeS scales are formed and atomic hydrogen is produced on the steel surface. The FeS scales formed by the hydrogen sulfide may or may not be protective, depending on conditions such as pH, temperature and H<sub>2</sub>S partial pressure. H<sub>2</sub>S accelerates the corrosion reaction and for low alloy steels the corrosion rate increase with decreasing pH of the acidic H<sub>2</sub>S containing environment. [3, 8-11]

Anodic reaction:



Cathodic reactions:



Net reaction:



The H<sub>2</sub>S corrosion is affected by both the generation of hydrogen and the diffusion of hydrogen into the steel. Therefore, the role of H<sub>2</sub>S is considered to be two-fold. It increases the rate of corrosion of steel in aqueous solutions and it prevents the hydrogen recombination reaction. In H<sub>2</sub>S containing environments, the absorption of atomic hydrogen into the metal is enhanced by the effect of sulfur containing species to prevent hydrogen recombination. Corrosion of low alloy steels in H<sub>2</sub>S containing environments commonly occur as localized corrosion forms such as pitting. These pits are often the initiation site for SSC cracks. [1, 3, 5]

H<sub>2</sub>S in aqueous environments may contribute to several forms of embrittlement. Among others it may contribute to SSC, hydrogen induced cracking (HIC) and stress oriented hydrogen induced cracking (SOHIC). The main difference between SSC, HIC and SOHIC is that SSC results from atomic hydrogen in the metal, while HIC and SOHIC involve

recombination of atomic hydrogen to molecular hydrogen at weak interfaces in the material. In the contrary to SSC, HIC can also occur when there is no applied stress present. However, when applied or residual stresses are present HIC can form a number of short blisters; this is referred to as SOHIC. [1]

## 2.2. Stress corrosion cracking

Stress corrosion cracking (SCC) is covering both the initiation and propagation of cracks that are induced by the environment. The cracks initiate at weak points of the surface, e.g. at crevices or pits. The cracks may follow intergranular, transgranular path as in Figure 2 or it may follow a mixed path. The cracks exist in the direction perpendicular to the applied stress. Generally, intergranular cracking appears in high strength steels, while transgranular cracking or a mixed path appears in lower strength steels. Two types of mechanism have been suggested for SCC. These are related to the anodic and cathodic reactions. Cracks may grow because of anodic dissolution along a susceptible path, the so-called active path corrosion. The cathodic reaction on the other hand, may cause hydrogen embrittlement cracking where the crack growth is controlled by absorption of atomic hydrogen into the steel. When investigating SCC some important factors must be included. These are the severity of the environment, susceptibility of the material and the stress level which the material is subjected to. [11-15]

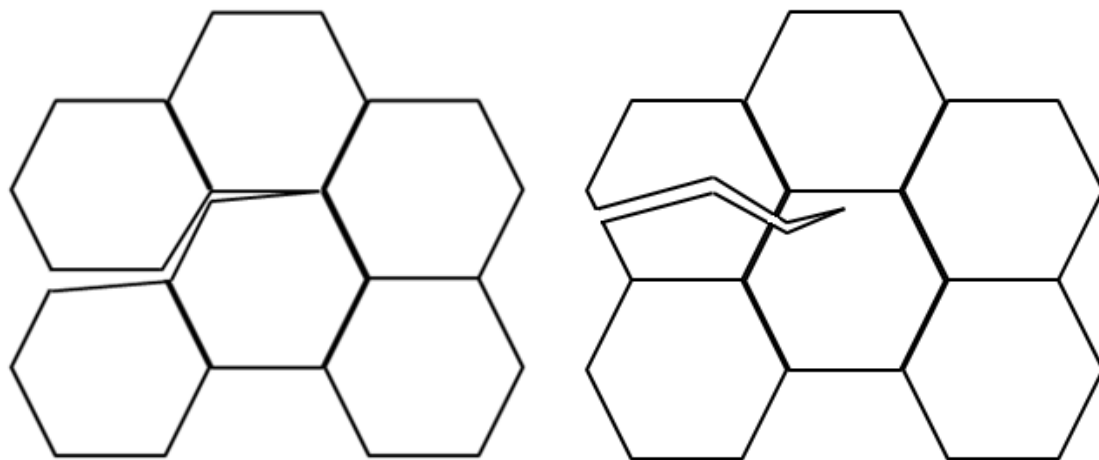


Figure 2: Intergranular (left) and transgranular (right) paths for cracking.

## 2.3. Sulfide stress corrosion cracking

When  $H_2S$  is present in oil and gas pipelines, HIC and SSC may occur. SSC is a form of hydrogen stress-cracking which is assisted by hydrogen embrittlement (HE), and it occurs in  $H_2S$  containing media, under both applied and residual tensile stress. According to Ifezue, D and F. Tobins [16], SSC is commonly observed in high tensile strength steels and generally not observed in steels with tensile strengths below 504 MPa. SSC is one of the most common

H<sub>2</sub>S corrosion cracking problems and is closely related to hydrogen production and diffusion. [3, 7, 17-19]

SSC results from corrosion in the presence of H<sub>2</sub>S followed by diffusion of atomic hydrogen into the steel. When hydrogen is evolved on the surface of the metal in the H<sub>2</sub>S corrosion process, the presence of H<sub>2</sub>S causes hydrogen atoms to enter the metal, rather than to form hydrogen molecules and bubble off. The role of H<sub>2</sub>S in SSC is two-fold, it increases the corrosion rate of steel and it “poisons” the hydrogen recombination reaction and thereby prevents the atomic hydrogen to recombine and form H<sub>2</sub> (g). Sulfides also promote the entry of hydrogen atoms into the material. This causes more hydrogen to enter the steel where it will cause cracking. In the metal, hydrogen atoms diffuse to regions of high internal stress such as grain boundaries, inclusions and regions of high triaxial stress, where they become trapped and cause embrittlement. There is a critical hydrogen uptake rate or concentration in the steel for the cracking to initiate. [5, 20] Below this critical rate or concentration, cracking does not occur. SSC is dependent upon a number of parameters. The most important are H<sub>2</sub>S partial pressure, pH and temperature. These parameters are discussed further in section 2.4. SSC is also controlled by the applied and residual stresses. [3, 16, 17, 21, 22]

SSC may appear as both intergranular and transgranular cracking in low alloy steels. According to R.D. Kane it is observed that SSC in high strength steels (> 700 MPa yield strength) appear as intergranular cracking, while in lower strength steels (< 700 MPa yield strength) SSC appear as transgranular cracking or mixed paths. [11]

When evaluating and selecting materials for sour environments, possibly providing SSC, failure modes such as hydrogen blistering, HIC and pitting corrosion must also be considered. [22]

## **2.4. Factors affecting sulfide stress corrosion cracking**

The susceptibility of steels to SSC depends on both environmental and metallurgical factors. The most important parameters are H<sub>2</sub>S partial pressure (p<sub>H<sub>2</sub>S</sub>) and pH of the solution. Other factors with an effect on SSC in low alloy steels are among others temperature and mechanical properties such as hardness and strength. Iron sulfide chemistry is very complex and minor changes in test conditions may lead to significantly different results. [3, 7, 23, 24]

### **2.4.1. Environmental factors**

The three most important environmental factors affecting SSC are pH, temperature and H<sub>2</sub>S partial pressure (p<sub>H<sub>2</sub>S</sub>). [1, 21]

The test temperature affects the cracking susceptibility as SSC is a temperature dependent phenomenon. For carbon and low alloy steels, the susceptibility to SSC reaches a maximum at about room temperature and the SSC resistance increases with increasing temperature. The temperature dependency is illustrated in Figure 3, where the time to failure is related to temperature for a C-Mn-steel. At low temperatures the diffusion rate of hydrogen is so slow that the critical concentration for SSC is never reached. While at higher temperatures, the

diffusion rate is so high that the hydrogen passes through the material in such a rapid manner that the critical concentration is not reached. [1, 3, 20-22]

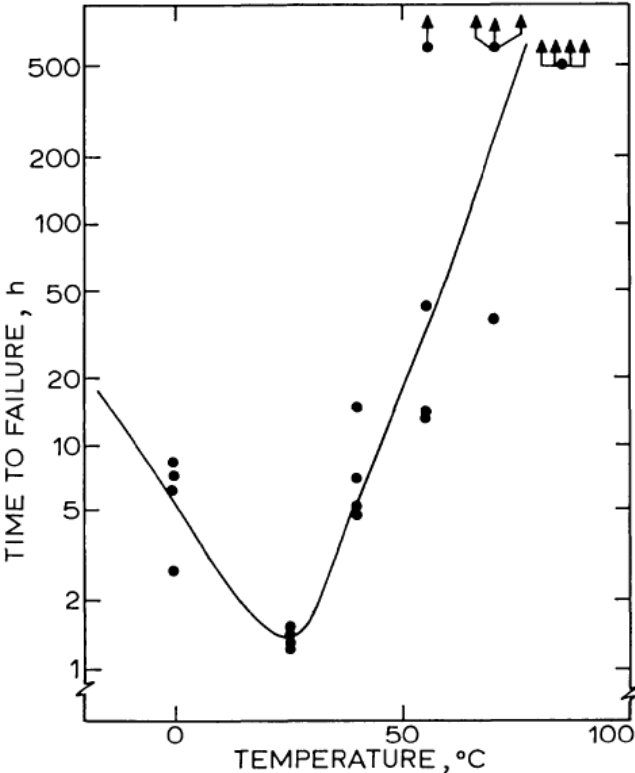


Figure 3: Time to failure by SSC versus temperature for a C-Mn steel, showing maximum susceptibility to SSC at about 25°C. [1]

The partial pressure of hydrogen sulfide ( $p_{H_2S}$ ) also affects the corrosion process. An increase in  $H_2S$  partial pressure in the corrosive environment will increase the materials susceptibility to SSC. In sour corrosion, general corrosion rate decreases and pitting occurs with increasing partial pressure of  $H_2S$ . If the  $H_2S$  partial pressure of the corrosive environment is increased, other parameters, such as hardness of the steel or the pH of the solution, must be adjusted to obtain the same SSC resistance. [17, 25]

The severity of the two and most important parameters,  $H_2S$  partial pressure and pH, are expressed in the  $p_{H_2S}$  – pH diagram (Figure 4). Based on the three regions in the diagram, it shows that the susceptibility to SSC increases with decreasing pH and increasing  $p_{H_2S}$ . The diagram represents the general guidelines for the occurrence of SSC in carbon and low alloy steels. It is divided into three regions based on the severity of the environment. In region 1, SSC does not occur and it may be referred to as “sweet corrosion”. Region 2 is the transition zone where consideration has to be made regarding critical metallurgical requirements for the materials selected. Region 3 is the sour service region and represents the most severe

environmental conditions where SSC may occur. Steels applied for environments in the third region shall be resistant to SSC, according to EFC publication number 16. [1, 3]

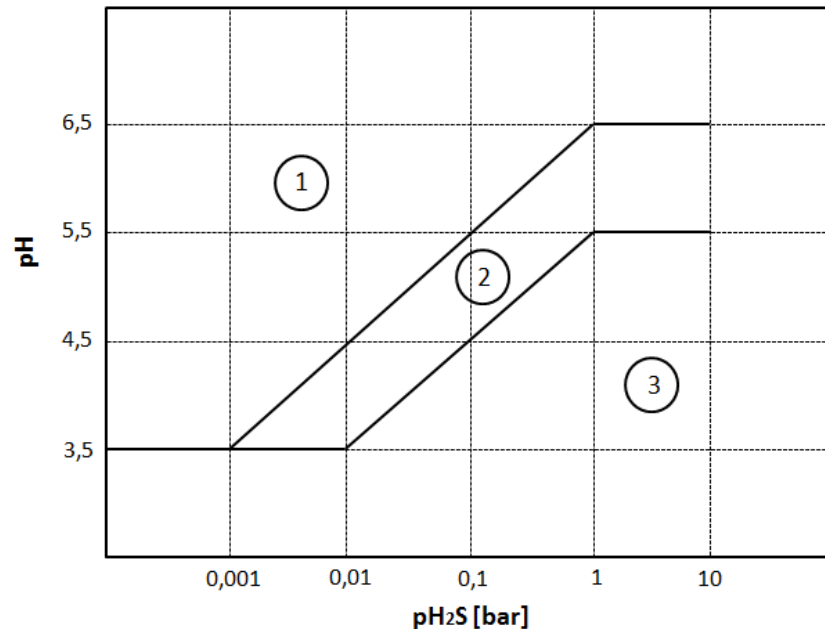


Figure 4: pH – pH<sub>2</sub>S diagram indicating the three regions of severity of the corrosive medium on SSC for carbon and low alloy steels. [7]

#### 2.4.2. Metallurgical factors

Mechanical properties, such as strength and hardness level, affect the susceptibility of steels to SSC. According to ISO 15156-2, carbon and low alloy steels with hardness levels below 250 HV (22 HRC) are usually not susceptible to SSC. This requirement regarding maximum hardness also applies to the heat-affected zone (HAZ) of the material, when welding. However, this requirement may be overly conservative for steels with low carbon content and high toughness. The hardness is regarded as a rough index describing the susceptibility to hydrogen stress-cracking. Therefore, this critical hardness level is not adequate to assess the susceptibility to SSC. The hardness level at which steels are susceptible to SSC also depends upon the severity of the environment. An increased strength level of steels increases the susceptibility to SSC in wet H<sub>2</sub>S environments. Below a certain ratio between the applied stresses and the yield stress, SSC will not occur. The susceptibility to SSC may vary between the various microstructures, even if the hardness level is equal. SSC may be prevented by limiting the strength and thereby eliminating crack sensitive microstructures. [2, 3, 5, 7, 17, 23, 26]

The microstructure of the steel affects the hydrogen uptake and the transportation of hydrogen. Therefore, the microstructure has a strong effect on SSC resistance. The susceptibility to SSC increases by the presence of hard microstructures such as untempered and partly tempered martensite and bainite. Hard microstructures may also be introduced

when welding and particularly in the HAZ. According to Zhao M.-C., *et al.*[5], an acicular ferrite dominated microstructure possesses better SSC resistance than ultrafine ferrite and ferrite-pearlite structures. The acicular ferrite structure is also more resistant to SSC than bainite, possibly due to the high dislocation density of acicular ferrite, as dislocations may act as hydrogen traps which hinder diffusion of hydrogen in the steel. The influence of chemical elements and grain size in the microstructure is not completely understood and the effect may vary from one alloy to another. [1, 3, 17, 27, 28]

## 2.5. Welding of low-alloy steel

SSC may occur both in the base material and in welded material. The metallurgical changes that occur when welding low alloy steels affect the susceptibility to SSC, because the HAZ is hardened and thereby becomes more susceptible to SSC. When welding, the stress level is increased and hard microstructures or local brittle zones (LBZ) may occur. These two factors may promote formation of cracks in the fusion zone and in the HAZ, causing the SSC susceptibility to increase in the welded regions. [7, 17, 29, 30]

According to Omweg, G. *et al.*, HAZ regions have shown heightened susceptibility to SSC in both service and laboratory experiments. The martensite-austenite (M-A) constituents with low HAZ toughness contributes to the lower SSC resistance in the HAZ. [2]

Factors affecting the weldability of steel are among others, the chemical composition of the steel, the peak temperature and the cooling rate. A high cooling rate will cause microstructures which are susceptible to SSC, such as martensite. The chemical composition also affects the microstructure in the HAZ. In welding, the effect of the chemical composition may be expressed as the carbon equivalent (CE) of the steel. [17] A reduction in the CE leads to improved weldability and increased resistance to SSC. The carbon equivalent should be kept below 0,45 for good weldability. The CE may be calculated as in equation 5. [30-32]

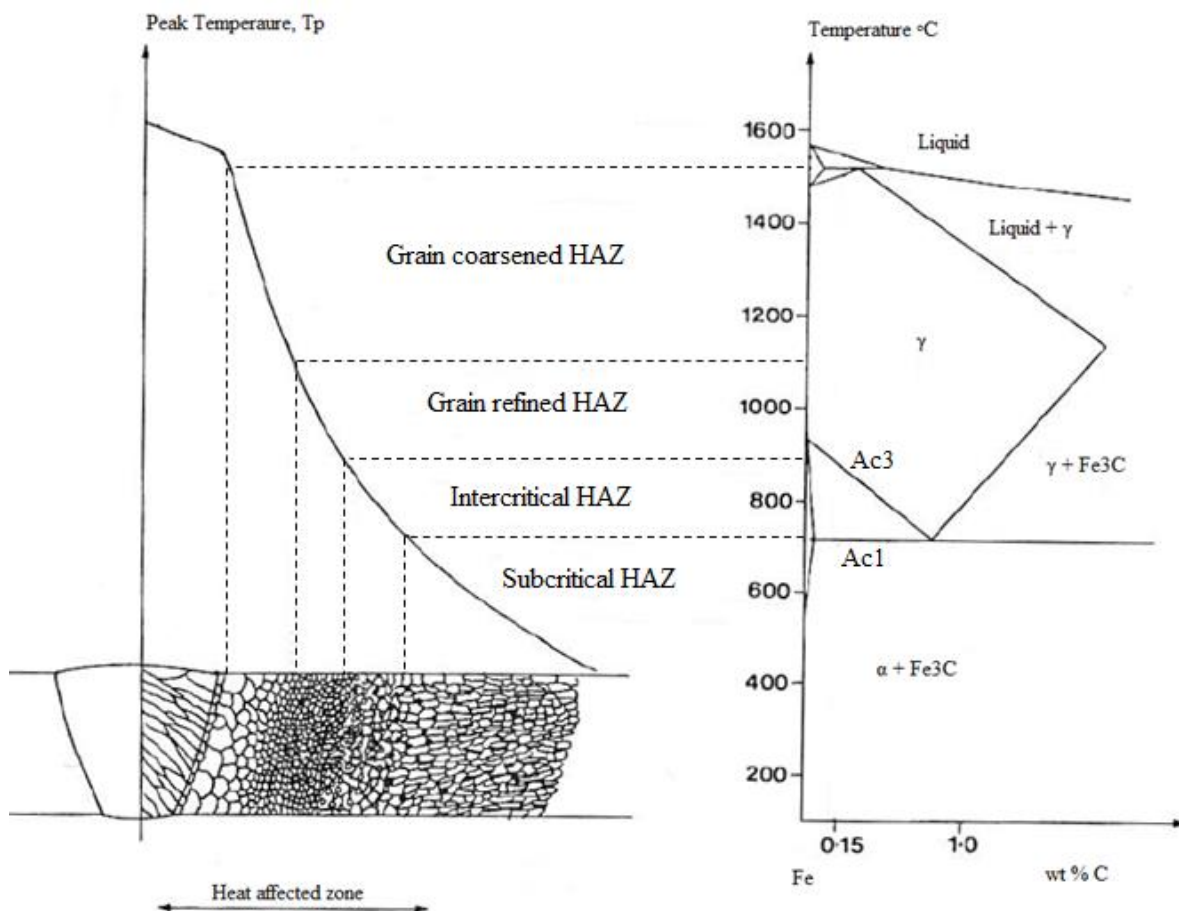
An empirical relationship for CE is given by:

$$CE = C + \frac{Mn}{6} + \left( \frac{Cr+Mo+V}{5} \right) + \left( \frac{Ni+Cu}{15} \right) \quad (5)$$

### 2.5.1. Microstructural changes during welding

The HAZ is the part of the material on the boarder to the fusion zone that has been heated sufficiently to cause changes in microstructure and properties. The HAZ may be divided into different regions towards falling temperature. Four characteristic regions are defined for the HAZ. The four regions, with corresponding temperatures, are as illustrated in Figure 5, the coarse grained region, the fine-grained region, the intercritical region and the subcritical region. The regions are determined by the peak temperature in which the various regions of the material was exposed to during the weld thermal cycle. Closest to the weld zone and at the highest temperature, the coarse grained HAZ (CGHAZ) exists, where austenite grains are

developed during heating. These austenite grains coarsen due to annealing during heating. At lower temperatures, the grain refined HAZ is found. In this region the size of the austenite grains are significantly finer, providing mechanical properties superior to the CGHAZ. At lower temperatures, between the Ac3 line and the Ac1 line (Figure 5), the intercritical HAZ (ICHAZ) is found. In this region, the structure only partially transform to austenite. The part that does not transform to austenite becomes tempered. At even lower temperatures, the subcritical HAZ exists. The peak temperature in this region is not high enough to cause formation of austenite. The only effect on the microstructure in this region, is tempering. [33-35]



**Figure 5: Definition of regions in the heat-affected zone (HAZ). [34]**

During multi-pass welding, the HAZ formed by the first thermal cycle is modified by the following thermal cycle (Figure 6). By the second thermal cycle, local brittle zones (LBZ) are formed in the intercritically reheated CGHAZ, highlighted in Figure 6. The martensite-austenite (M-A) constituents, formed after multi-pass welding, in the intercritically reheated CGHAZ is an example of such LBZs. When heating, the austenite islands become enriched in carbon, as carbides at the grain boundaries dissolve and enter into the austenite. During cooling, diffusion of carbon is slow due to a low heating temperature, this provides

boundaries rich in carbon and M-A constituents are formed. The intercritically reheated CGHAZ is the region that possesses the lowest HAZ toughness. [36, 37]

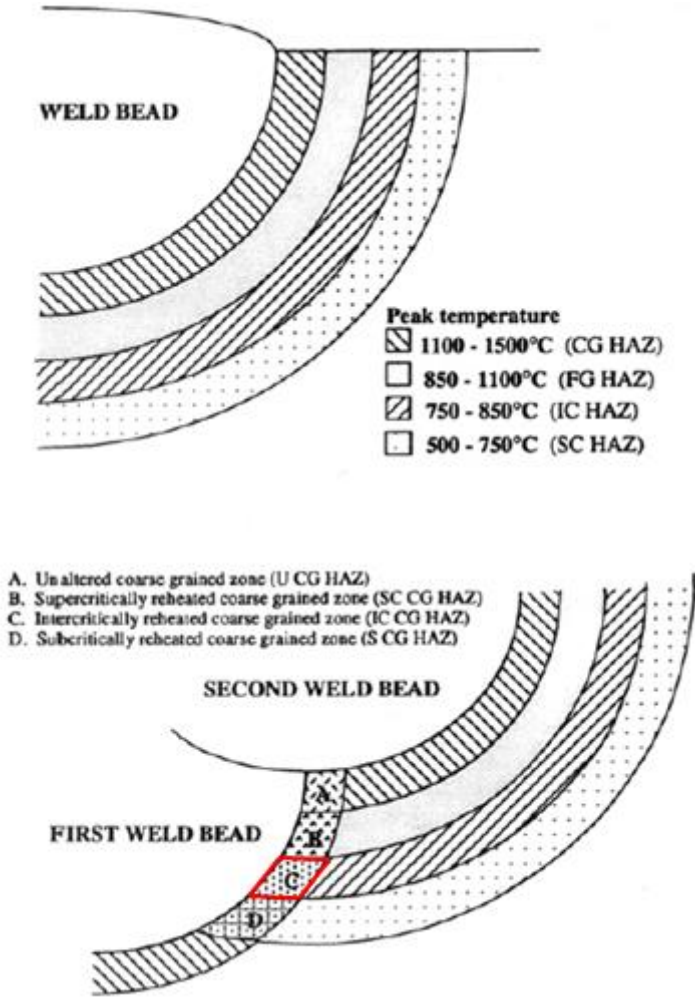


Figure 6: Microstructural changes of the HAZ by the first and second weld thermal cycle. [38]

For low alloy steels the coarse CGHAZ formed after the first weld bead consists of bainite having a large prior austenite grain size developed during heating. During the second thermal cycle or the intercritical reheating of the steel into the austenite and ferrite two phase region, austenite nucleates and grows along the bainite lath boundaries and at the prior austenite grain boundaries. These austenite islands become enriched in carbon and transform to hard and brittle phases such as the M-A constituents during cooling. Micro-hardness indentations may reveal M-A constituents in the microstructure as the hardness of these constituents are between HV 400 to HV 600. The formation of M-A constituents is dependent on the chemical composition of the steel and the amount of austenite within the island decrease as the size of the constituent increase. [34, 39]



### **2.5.2. Weld defects**

The welding process creates defects, stress concentration and higher residual stresses in the steel. These defects may be present both in and around the weldment and the weld defects create local stresses, which may increase the risk of brittle fracture. Stresses caused by welding influence the structural behavior. However, there are some differences between the various stresses caused by welding. Stresses caused by welding defects are directly proportional to the applied stress, while the residual stresses may exist in absence of applied loads, implying that the residual stress distributions in welds are complex. [37, 40]



### 3. Experimental methods

#### 3.1. ASTM A694 F60 low alloy steel

The standard ASTM A694 F60 low alloy steel is alloyed with elements such as carbon, manganese and silicon among others. Requirements to chemical composition according to the standard ASTM A694 are presented in Table 1. The steel is mechanically hot worked to reach a wrought structure throughout the section thickness, followed by one of the following heat treatment processes: normalizing, normalizing and tempering, or quenching and tempering. In this project, modified F60 low alloy steel is tested. [41, 42]

**Table 1: Requirements to chemical composition of ASTM A694 F60 steel [wt%]. [41]**

|            | <b>Carbon</b> | <b>Manganese</b> | <b>Phosphorus</b> | <b>Sulfur</b> | <b>Silicon</b> |
|------------|---------------|------------------|-------------------|---------------|----------------|
| <b>Min</b> | -             | -                | -                 | -             | 0.15           |
| <b>Max</b> | 0.26          | 1.60             | 0.025             | 0.025         | 0.35           |

According to ASTM A694, the mechanical properties of F60 steel are as described in Table 2, all values are minimum values.

**Table 2: Mechanical properties of the F60 low alloy steel according to ASTM A694. [41]**

| <b>Material</b> | <b>Yield strength [MPa]</b> | <b>Tensile strength [MPa]</b> | <b>Elongation %</b> |
|-----------------|-----------------------------|-------------------------------|---------------------|
| <b>F60</b>      | 415                         | 515                           | 20.0                |

#### 3.2. Modifications for the oil and gas industry

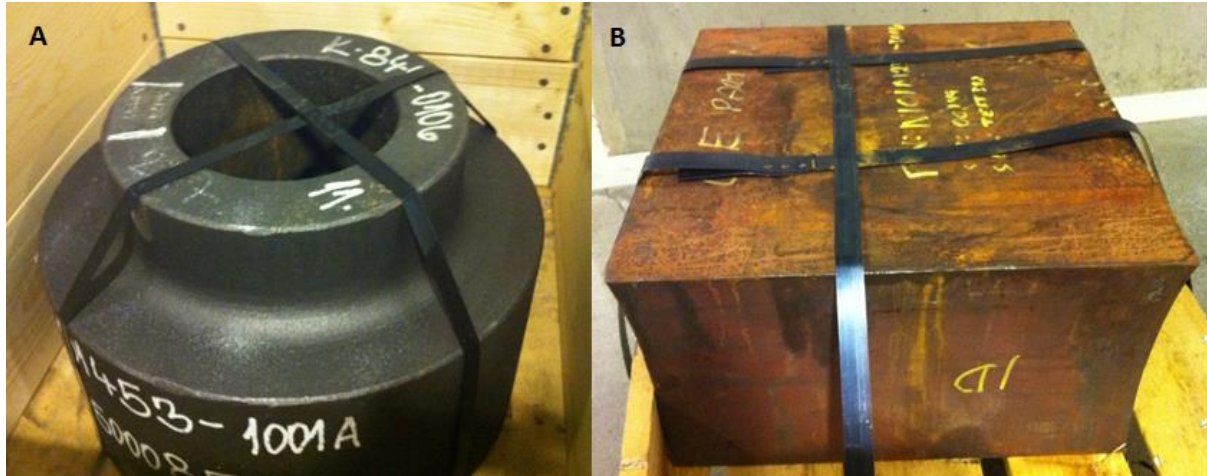
The chemical composition of the ASTM A694 F60 steel is modified with chromium, nickel, molybdenum and micro alloying elements. These elements are added to improve through-hardening properties in heavy wall forgings, as well as for improved low temperature properties. The carbon content is reduced to improve the weldability. Typical applications within the oil and gas industry for the modified F60 low alloy steel are hub connectors, flanges and valve bodies. [43]

The modified F60 steel is similar to the low alloy steel of ASTM SA508 grade 3 class 2 and the French standard 16MND5. Such steels are typically used for heavy section forgings of pressure vessels. [44, 45]

The two materials tested in this project are named material A and material B in the report, as the manufacturers of the steels are considered confidential by GE Oil & Gas. Photos of the materials are presented in Figure 7. The wall thickness of the two materials is 135 mm for material A and 350 mm for material B. Further dimensions are presented in section 3.3. Chemical composition and heat numbers of the two alloys are presented in Table 3.

**Table 3: Chemical composition of material A and material B.**

|          | C    | Mn   | Si   | P     | S     | Cr   | Ni   | Mo   | V     | Nb    | Ti     | Cu   | Al    | N      | B      | Heat nr. |
|----------|------|------|------|-------|-------|------|------|------|-------|-------|--------|------|-------|--------|--------|----------|
| <b>A</b> | 0.10 | 1.12 | 0.26 | 0.003 | 0.001 | 0.14 | 0.66 | 0.21 | 0.03  | 0.034 | 0.004  | 0.13 | 0.025 | 0.0048 | -      | 36174    |
| <b>B</b> | 0.10 | 1.12 | 0.28 | 0.005 | 0.004 | 0.18 | 0.87 | 0.28 | 0.032 | 0.035 | 0.0025 | 0.08 | 0.032 | 0.0032 | 0.0001 | 00149    |



**Figure 7: Hub forging of material A (left) with wall-thickness 135 mm. Section of hub forging of material B (right) with wall thickness 350 mm.**

### 3.3. Specimen sampling

All test specimens were machined from metallurgical equivalent positions, i.e. same orientation with nearly the same microstructure and mechanical properties. Since the H<sub>2</sub>S-containing well fluid is in contact with the inner surface of the hub connectors, all specimens, both for tensile testing and four-point bend-testing, were machined from positions as close to the inner surface of the hub connectors as possible.

Thirteen four-point bend (FPB) specimens were machined from both material A and material B to provide 3 parallel specimens of both materials for the various conditions in the two test environments. The additional specimen of each material was machined for microstructure and hardness studies of the base materials and the HAZ. The specimens for the tensile test were machined from positions in between the FPB-specimens to provide as representative results as possible from the mechanical testing. The sampling of FPB-specimens and tensile specimens from material A and material B is illustrated in Figure 8 and Figure 9. The rectangular specimens with a length of 120 mm, are the FPB-specimens, while the cylindrical specimens with a length of 70 mm are the tensile specimens.

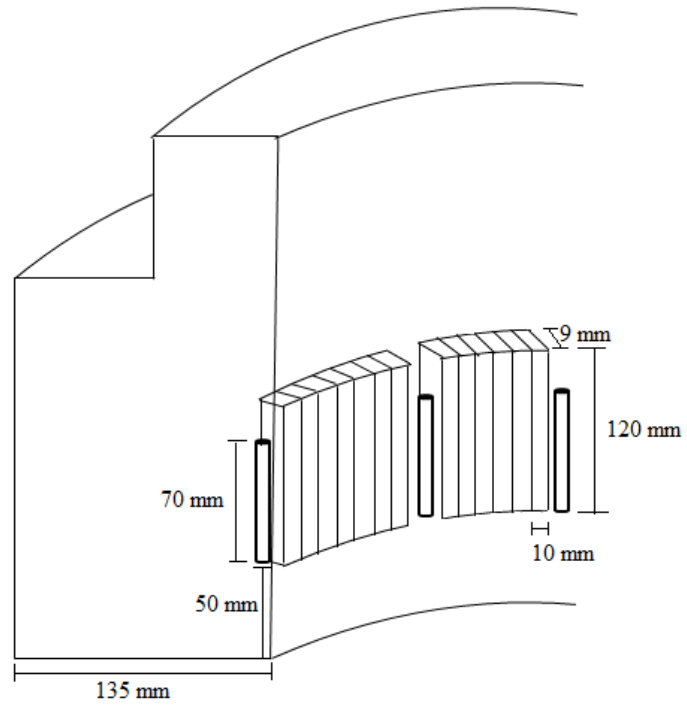


Figure 8: Sampling of tensile specimens and four-point bend-specimens from material A.

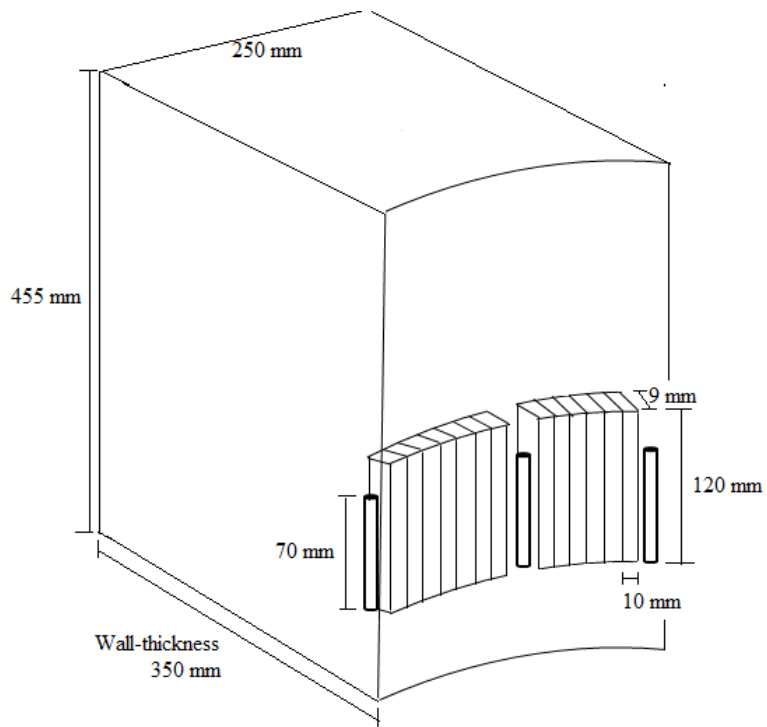


Figure 9: Sampling of tensile specimens and four-point bend-specimens from material B.

### 3.4. Tensile test

Tensile testing was performed to determine the actual yield strength (AYS) of the materials at room temperature. The yield strength of a metallic material is the minimum stress level which is needed to initiate plastic deformation of the material. The actual yield strength was determined by the offset method, applied on the obtained stress-strain curves. When discontinuous yielding occurred, the lower yield strength and upper yield strength was determined from the stress-strain curves. The lower and upper yield strengths are respectively the minimum stress recorded during discontinuous yielding and the first maximum stress recorded during discontinuous yielding at or near the initiation of plastic deformation. The test involved straining of the test specimens to fracture by a tensile force on a Zwick 30kN universal test machine, model Z030 in Figure 10. An MTS extensometer, model 634.31F-25 with an HBM amplifier, model Scout55 was employed to record the strain. Three parallel specimens of each material were pulled, and the results were averaged. Dimensions of the cylindrical tensile specimens are as illustrated in Figure 11, with a total length of 70 mm. [46, 47]



Figure 10: Zwick 30kN universal test machine, model Z030, used for tensile testing. [Zwick Roell]

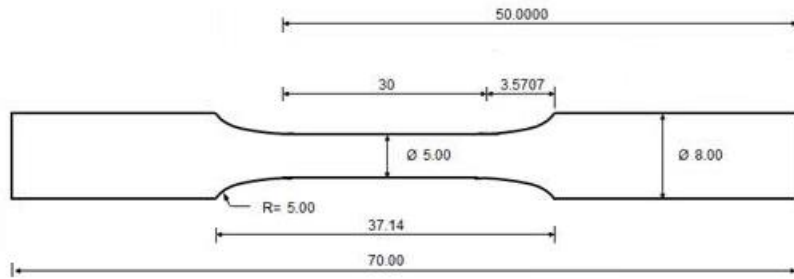


Figure 11: Dimensions of tensile test specimens, in mm. [Provided by SINTEF]

### 3.5. Thermal weld simulation

The microstructure of the HAZ significantly affects the SSC resistance, and the microstructure of a thermally weld simulated material depends upon heat input, peak temperature and cooling time. Thermal weld simulation may provide rapid heating, inhomogeneous cooling and high peak temperatures. This simulates the continuous changes in microstructure and properties in the HAZ. A fixed distance into the HAZ may therefore be recreated by thermal weld simulation. A certain volume with the expected microstructure is thereby created in the material. The thermal weld simulation tests are an economical and reproducible method for analyzing the microstructure and properties of the HAZ.[36, 48]

The thermal weld simulations were performed on a SMITHWELD Thermal Cycle Simulator Model 1405 (Figure 12). The thermocouples were spot welded onto the center of the FPB-specimens before they were mounted into the instrument.

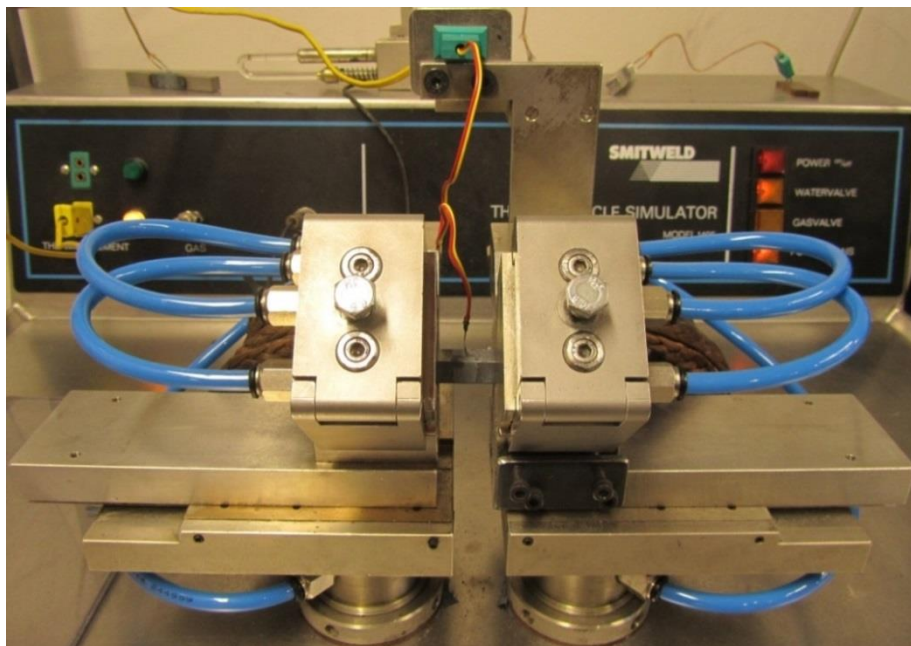


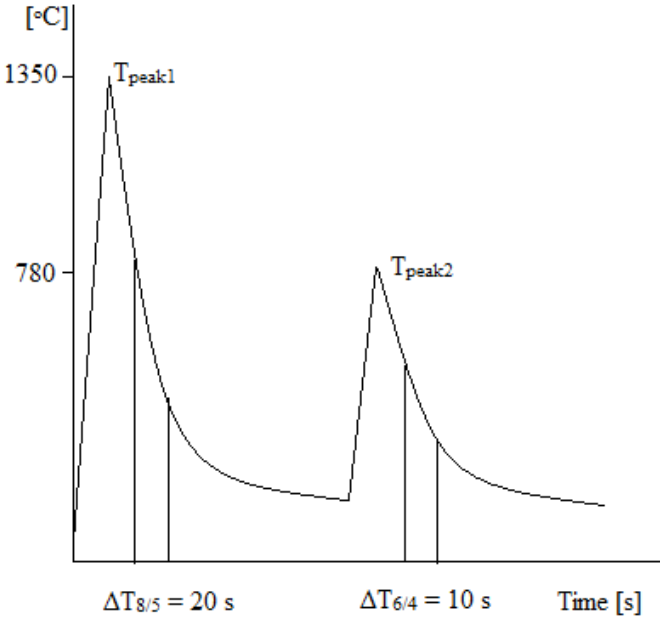
Figure 12: Equipment used for the thermal weld simulation, SMITHWLED Thermal Cycle Simulator.

The thermal weld simulations were performed in two cycles, with parameters as described in Table 4. The specimens were first heated to a peak temperature of 1350°C, with a cooling time ( $\Delta t_{8/5}$ ) of approximately 20 seconds from 800°C to 500°C, before reheated to a peak temperature of 780°C with a cooling time ( $\Delta t_{6/4}$ ) of approximately 10 seconds from 600°C to 400°C. The actual thermal weld simulation parameters varied from the predetermined theoretical parameters. The achieved peak temperatures were all within a few degrees Celsius from the predetermined temperatures, while all the cooling times were slightly shorter than the predetermined times.

**Table 4: Applied parameters for the thermal weld simulation of FPB-specimens.**

| Cycle | $T_{peak}$<br>[°C] | $\Delta T_{8/5}$ [s] | $\Delta T_{6/4}$ [s] | Clamp distance<br>[mm] | Uprate limit<br>[°C/s] |
|-------|--------------------|----------------------|----------------------|------------------------|------------------------|
| 1     | 1350               | 20                   | -                    | 24                     | 100                    |
| 2     | 780                | -                    | 10                   | 24                     | 100                    |

The parameters are illustrated in Figure 13, by a schematic graph, where temperature versus time is plotted. The heating and cooling sequence of the program are described and shows the peak temperatures and cooling times of both cycles.

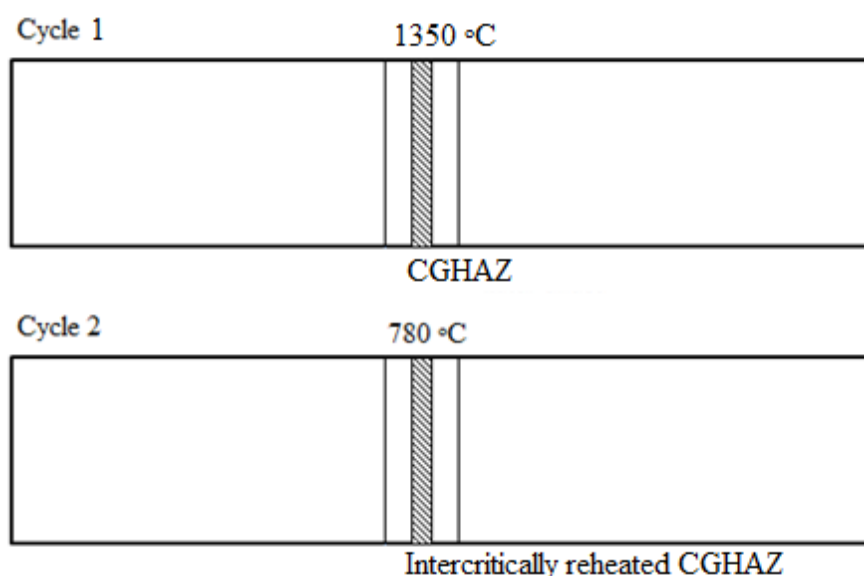


**Figure 13: Thermal weld simulation in two cycles.**

After the thermal weld simulations were completed, the electrodes and scales were removed, before the specimens were machined to the appropriate dimensions for the SSC testing and notches were machined into the center of the simulated welds. This thermal weld simulation



program was selected on the basis that it provides an unfavorable microstructure, with the intercritically reheated CGHAZ in the center of the specimens. The first cycle, provides a brittle bainitic structure, as in the CGHAZ, while the second thermal cycle results in an intercritically reheated CGHAZ at the center of the specimens in the HAZ (Figure 14). In this region hard M-A constituents are formed in the microstructure.



**Figure 14: HAZ regions of the specimens after the first thermal cycle (CGHAZ) and the second thermal cycle (intercritically reheated CGHAZ).**

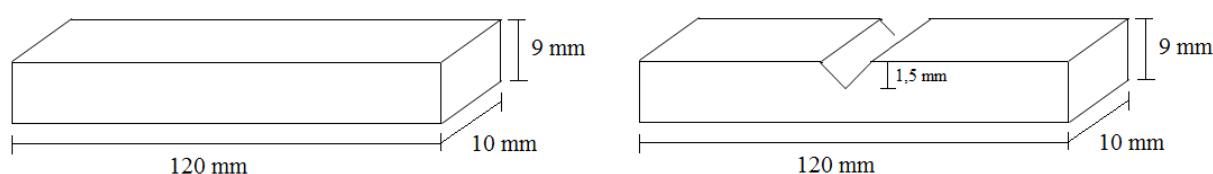
### **3.6. Testing of resistance to sulfide stress corrosion cracking**

The most common test methods for testing of steel resistance to SSC are tensile testing with either constant or increasing load, bend tests and fracture mechanics testing. In this project a four-point bend-test (FPB-test) was selected to evaluate the SSC resistance of the two materials. The bend test is a constant strain test, where the applied stress decreases as the crack grows. Constant strain tests are common since they are usually relatively simple and cheap. The possibility for a compact size of the test specimen makes testing of small, localized areas possible. The four point loading provides a relatively large area of uniform longitudinal stress on the deflected surface, representing the process wetted side surface of the specimen, between the inner supports. The stress decreases linearly to zero from the inner supports to the outer supports. The FPB test provides a failure/no-failure test as it is loaded to a particular stress. [17, 22, 49-51]

#### **3.6.1. Four point bend test**

The characterization of the resistance to SSC was performed according to the NACE standard TM0177, ISO 15156-2 and EFC 16. The test consisted in exposing the steels to a specific H<sub>2</sub>S-containing environment, while the specimens were stressed in a four-point jig.

The FPB-specimens were 120 mm long, 10 mm wide and 9 mm thick as illustrated schematically in Figure 15 and documented by a photo in Figure 16. The 10 mm long side of the specimens, pointing up in Figure 15, represents the inner surface of the hub, which is exposed to the well fluid. The thermal weld simulated specimens were notched to concentrate the applied stress at the center. The notch depth of the thermal weld simulated specimens was 1.5 mm. The presence of a machined notch in the middle of the strained surface induced a triaxial stress and caused an actual bending stress at the root of the notch which is higher than for the un-notched specimens by a factor of approximately 6 for this particular test. The increase in stress is dependent on the notch geometry. The specimens were ground on abrasive papers to mesh size 320 and rinsed thoroughly before they were loaded and exposed to the corrosive test environment. [52]



**Figure 15: Sketches of four-point bend-specimens of base material (left) and thermal weld simulated material (right) with dimensions 9x10x120 mm and a notch depth of 1.5 mm.**



**Figure 16: Notched four-point bend-specimen, the notched side is pointing up.**

The identifications of the parallel specimens are presented in the test matrix (Table 5) and are as follows. In test 1, the thermal weld simulated specimens are named A1 and B1 for material A and material B respectively. The specimens of base material in test 1 are named A2 and B2. The three parallels of each material are distinguished by the suffixes a, b and c, to illustrate that they are parallels of the same material under the same conditions. The same naming applies to test 2, where specimens named A3 and B3 are the thermal weld simulated specimens, while A4 and B4 are the specimens of the base materials. These are also followed by the suffixes a, b and c to be able to distinguish the three parallels.

The environmental parameters applied for the two SSC tests are described in the test matrix in Table 5. A test period of 720 h was used to evaluate the SSC resistance. Prolonging the test could cause pitting and grooving at the surface which may give false results by providing stress raisers and local sources of hydrogen. The tests were carried out at room temperature, which is expected to be the “worst case” for the occurrence of SSC in low alloy steels. [3] The H<sub>2</sub>S partial pressure and the pH of the two tests were selected to represent widely different

environments. In test 1, the transition between the sweet region and the transition region was investigated (Figure 17). The aim of the test was to assure that the materials are resistant to cracking under conditions that normally will not give SSC, as SSC is not expected to occur in the sweet region. If the materials would fail under these conditions, the area of application for these materials should be reconsidered. Test 2 was a test of high severity, a “worst case” test (Figure 17). The environment was sour and the high H<sub>2</sub>S partial pressure and low pH of the test was assumed to be detrimental for the materials. In test 1 a stress level of 90 % of the actual yield strength (AYS) was applied to the materials. The stress level represents the test requirements from the standard ISO 15156-2. In test 2, the base material and the thermal weld simulated materials were subjected to different stress levels. The stress level on the base material was kept the same as in test 1, while the thermal weld simulated material was subjected to a stress level equal to two-thirds (67%) of the specified minimum yield strength (SMYS) which is at 415 MPa, defined in the standard ASTM A694 “Standard Specification for Carbon and Alloy Steel Forgings for Pipe Flanges, Fittings, Valves and Parts of High-Pressure Transmission Service”. [41]

**Table 5: Test matrix for the four-point bend-tests, “test 1” and “test 2”.**

| <b>Material</b>                | <b>Test 1: Transition zone (region 2)</b>          |               |              |               | <b>Test 2: Sour service (region 3)</b>                |               |              |               |
|--------------------------------|--|---------------|--------------|---------------|---|---------------|--------------|---------------|
|                                | A  |               | B            |               | A   |               | B            |               |
| <b>Condition</b>               | HAZ, notched                                       | Base material | HAZ, notched | Base material | HAZ, notched  | Base material | HAZ, notched | Base material |
| <b>Parallels</b>               | 3  | 3             | 3            | 3             | 3   | 3             | 3            | 3             |
| <b>Names</b>                   | A1a,b,c  | A2a,b,c       | B1a,b,c      | B2a,b,c       | A3a,b,c   | A4a,b,c       | B3a,b,c      | B4a,b,c       |
| <b>Solution</b>                | 5 % NaCl and 0,4 % CH <sub>3</sub> COONa (acetate) |               |              |               | 5 % NaCl and 0,5 % CH <sub>3</sub> COOH (acetic acid) |               |              |               |
| <b>H<sub>2</sub>S-pressure</b> | 0,1 bar  |               |              |               | 1 bar   |               |              |               |
| <b>Total Pressure</b>          | 10 bar   |               |              |               | 10 bar  |               |              |               |
| <b>pH</b>                      | 5,5  |               |              |               | ≤4  |               |              |               |
| <b>Stress level</b>            | 90 % av AYS  |               |              |               | 90 % of AYS   | 2/3 of SMYS   | 90 % of AYS  | 2/3 of SMYS   |
| <b>Test duration</b>           | 720 h (30 days)                                    |               |              |               |   |               |              |               |
| <b>Temp.</b>                   | Room temperature                                   |               |              |               |   |               |              |               |

The severity of the corrosive mediums of test 1 and test 2 is expressed in the pH-pH<sub>2</sub>S diagram in Figure 17, showing that test 1, with a pH of 5.5 and a pH<sub>2</sub>S of 0.1 bar, represented the transition between region 1 and region 2, respectively the sweet region and the transition region, while test 2, with a pH ≤ 4 and pH<sub>2</sub>S of 1 bar, lies within region 3 which is the sour service region.

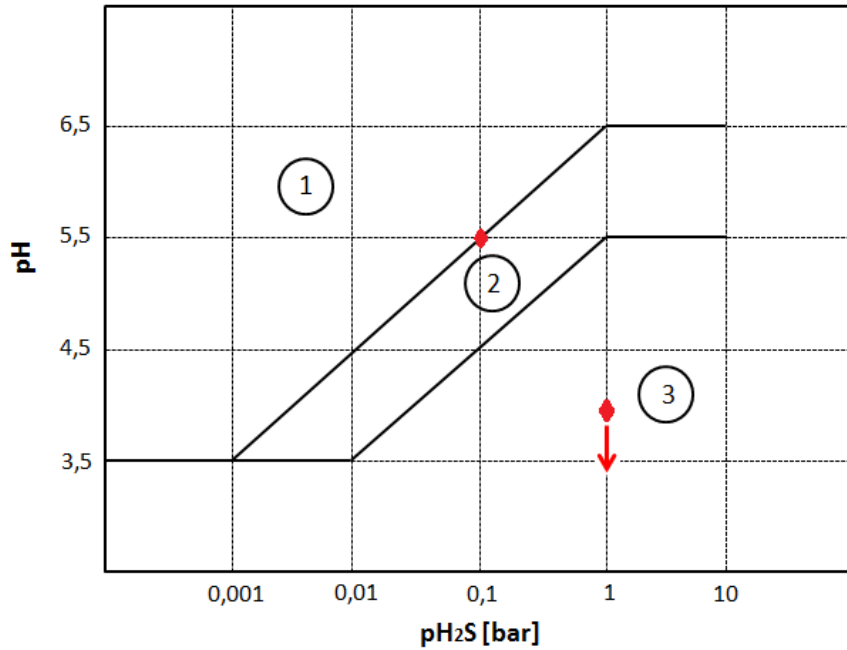


Figure 17: Environmental parameters for SSC test 1 and 2.

The electrolyte for test 1 was prepared by mixing NaCl (2000 g) and CH<sub>3</sub>COONa (160 g) with distilled water, in a titanium container, 40 liters of electrolyte was prepared. For test 2, 30 liters of electrolyte was prepared by mixing NaCl (1500 g) and CH<sub>3</sub>COOH (150 g) with distilled water in a titanium container. Both electrolytes were purged with nitrogen overnight to remove oxygen before the oxygen level was measured with an oxygen sensor on the Obisphere 410 equipment. The oxygen level shall be below 10 ppb, and was measured to 4.6 ppb in the electrolyte for test 1 and 2.4 ppb in the electrolyte for test 2, as documented in Figure 18.



Figure 18: Documentation of oxygen level of 4.6 ppb in electrolyte for test 1 (left) and an oxygen level of 2.4 ppb in the electrolyte for test 2 (right). The O<sub>2</sub>-level was measured on the Obisphere 410 instrument.

A schematic illustration of the SSC test set-up is illustrated in Figure 19. The actual “in laboratory test set-up” is presented in Figure 20. The gas cylinder, containing H<sub>2</sub>S and CO<sub>2</sub> gas was connected to the autoclave where the specimens were submerged in the electrolytes. The gas was led out to an exhaust bottle containing sodium hydroxide (10 % NaOH) for destruction of the gas.

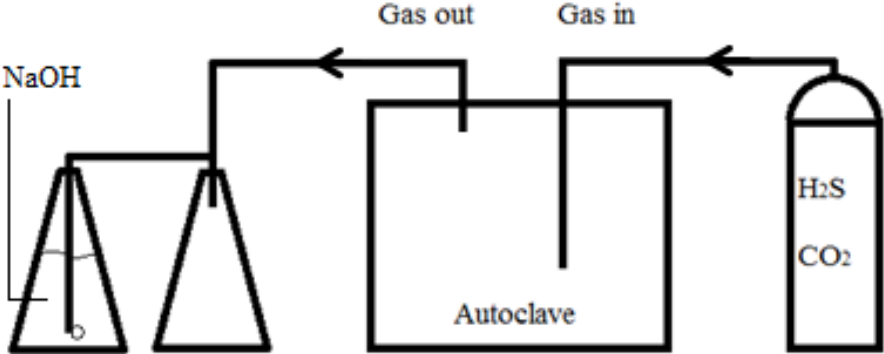


Figure 19: Schematic test set-up including test gas (right), autoclave and destruction of test gas (left).

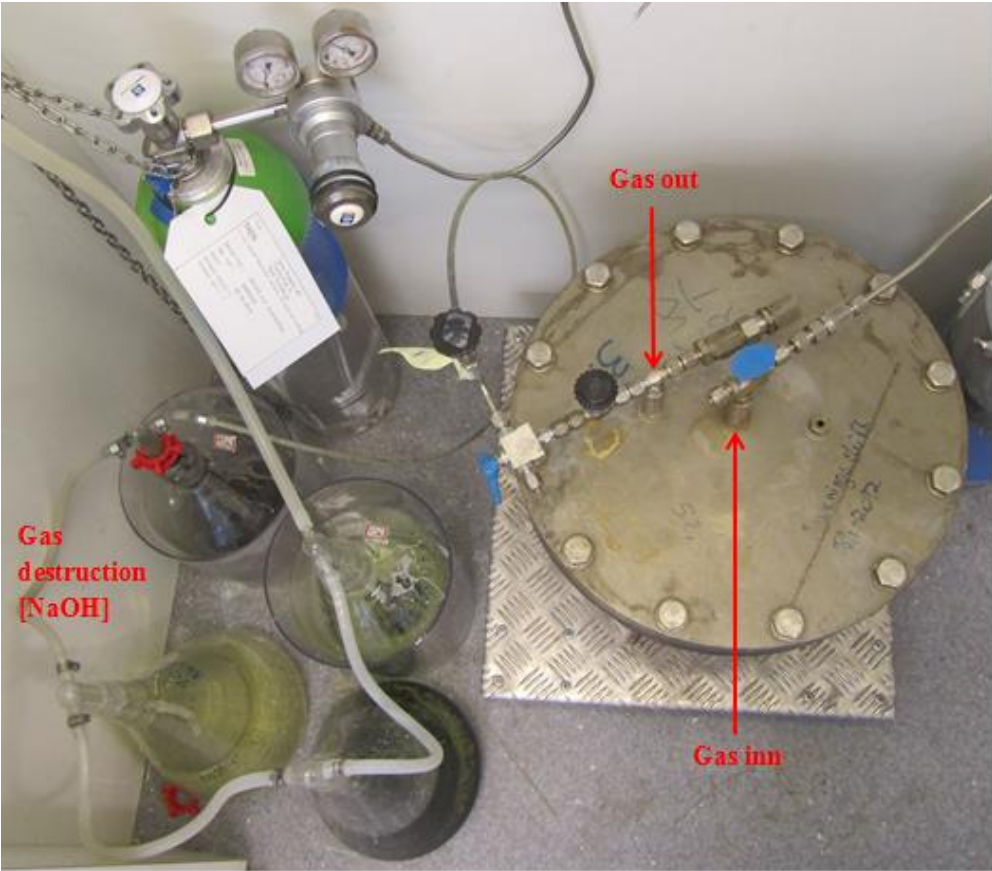


Figure 20: In laboratory test set-up, gas cylinder to the upper left, autoclave to the right and H<sub>2</sub>S gas destruction system to the lower left.

All specimens were stressed in separate jigs for FPB testing (Figure 21). The side of the specimens corresponding to the inner surface of the hub was deflected in the jig, as that side corresponds to the material that would be exposed to the well fluids. Loading of the FPB-specimens, by four-point bending in the jigs, was performed with an extensometer strapped to the specimen, recording the achieved strain. The extensometer was mounted at the center position of the base material specimens and some millimeters on the side of the notch on the thermally weld simulated specimens because the elastic strain in that area is approximately linear and can be directly related to the tensile data for the materials. 90 % of AYS and at two-thirds of the design SMYS were the target strains, while the achieved strains were recorded and documented for each specimen (Table 6). Documentation of the achieved strains is found in the photos in Appendix A. When the specimens were deflected in the jig, the specimens were rinsed carefully with acetone and arranged in the autoclave. [52]

**Table 6: Target strain and achieved strain for all specimens in both test 1 and 2.**

| <b>Specimen</b>   | <b>Condition</b> | <b>Target strain [%]</b> | <b>Achieved strain [%]</b> | <b>Specimen</b> | <b>Target strain [%]</b> | <b>Achieved strain [%]</b> |
|-------------------|------------------|--------------------------|----------------------------|-----------------|--------------------------|----------------------------|
| <b>Material A</b> |                  | <b>Test 1</b>            |                            | <b>Test 2</b>   |                          |                            |
| <b>1a</b>         | HAZ              | 0.2103                   | 0.2105                     | <b>3a</b>       | 0.1337                   | 0.1345                     |
| <b>1b</b>         |                  | 0.2103                   | 0.2100                     | <b>3b</b>       | 0.1337                   | 0.1334                     |
| <b>1c</b>         |                  | 0.2103                   | 0.2106                     | <b>3c</b>       | 0.1337                   | 0.1339                     |
| <b>2a</b>         | Base             | 0.2103                   | 0.2104                     | <b>4a</b>       | 0.2103                   | 0.2103                     |
| <b>2b</b>         | material         | 0.2103                   | 0.2102                     | <b>4b</b>       | 0.2103                   | 0.2113                     |
| <b>2c</b>         |                  | 0.2103                   | 0.2104                     | <b>4c</b>       | 0.2103                   | 0.2115                     |
| <b>Material B</b> |                  |                          |                            |                 |                          |                            |
| <b>1a</b>         | HAZ              | 0.2870                   | 0.2883                     | <b>3a</b>       | 0.1343                   | 0.1343                     |
| <b>1b</b>         |                  | 0.2870                   | 0.2875                     | <b>3b</b>       | 0.1343                   | 0.1345                     |
| <b>1c</b>         |                  | 0.2870                   | 0.2872                     | <b>3c</b>       | 0.1343                   | 0.1345                     |
| <b>2a</b>         | Base             | 0.2870                   | 0.2872                     | <b>4a</b>       | 0.2870                   | 0.2872                     |
| <b>2b</b>         | material         | 0.2870                   | 0.2878                     | <b>4b</b>       | 0.2870                   | 0.2875                     |
| <b>2c</b>         |                  | 0.2870                   | 0.2876                     | <b>4c</b>       | 0.2870                   | 0.2878                     |

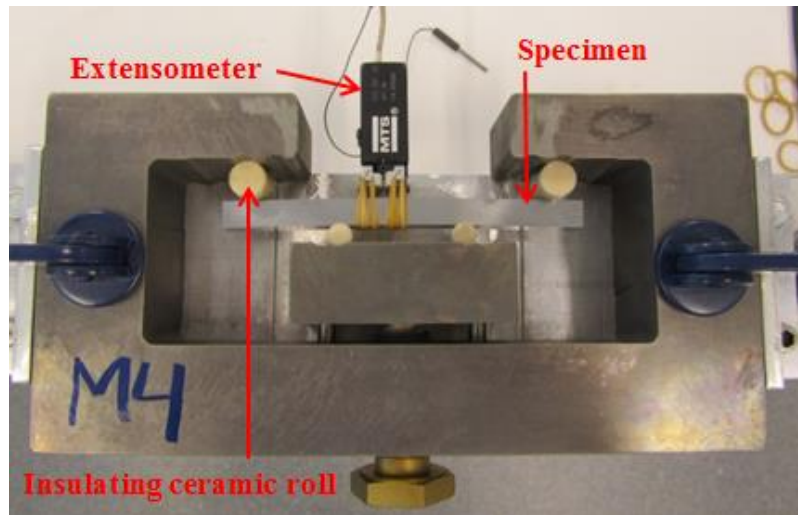


Figure 21: Specimen stressed in a jig with the extensometer strapped to the center of the specimen.

When all the jigs had been arranged in the autoclave, the autoclave was sealed and purged with nitrogen over night to remove the oxygen. The electrolyte was then transferred to the autoclave, through steel tubing to keep the system free of oxygen, and the autoclave was again purged with nitrogen for four hours. The electrolyte was saturated with CO<sub>2</sub> up to 9 bars before the test gas was connected to the autoclave. Certificates for both test gases are found in Appendix B. After bubbling of the test gas through the electrolyte, the sulfide content and the initial pH were measured.

According to SI Chemical Data the theoretical solubility of H<sub>2</sub>S ( $\frac{sol.}{g/100g}$ ) is 0.33. The solubility at 25°C is at a total pressure, for the gas plus H<sub>2</sub>O, of 1 atm. [53]

In test 1, the partial pressure of H<sub>2</sub>S (pH<sub>2</sub>S) in the gas was 1 % providing a solubility of sulfide in the solution of:

$$Sol. = 0.33 * \frac{0.01}{100} = 0.000033 = 33 \text{ ppm} \quad (6)$$

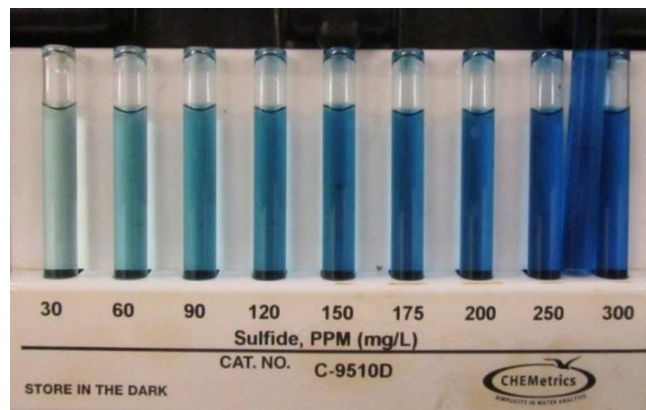
In test 2, pH<sub>2</sub>S of the gas is equal to 10 %, providing a solubility of sulfide in the solution of:

$$Sol. = 0.33 * \frac{0.1}{100} = 0.00033 = 330 \text{ ppm} \quad (7)$$

The sulfide content was measured on the CHEMetrics equipment and was compared both to the 0 – 30 ppm scale and the 30 – 300 ppm scale in Figure 22. The sulfur content of the electrolyte for test 1 was approximately 30 ppm, corresponding to the theoretical content calculated in equation 6. The pH was measured on the PHM210 Standard pH meter which provided an initial pH of 5.46 for test 1, while the final pH was 5.60. The bubbling of test gas through the electrolyte was reduced to approximately one bubble in the exhaust bottle per minute for the entire test time. In test 2, the sulfide content of the electrolyte was about 300 ppm as in Figure 23, corresponding to the theoretical content calculated in equation 7. The initial pH of test 2 was 3.0, and the final pH was measured at 3.73.



**Figure 22: Sulfide content of electrolyte in test 1 at about 30 ppm, on a scale from 0 – 30 ppm and 30 – 300 ppm.**



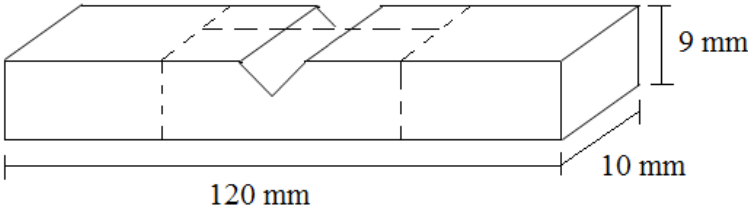
**Figure 23: Sulfide content of electrolyte in test 2 at about 300 ppm, on a scale from 30-300 ppm.**

The pH value of the electrolyte was measured once every week during test 1, and was kept within 0.1 pH units from the initial pH. When the pH deviate more than 0.1 units from the initial pH, HCl (10%) was added to a small amount of electrolyte in a separate autoclave, purged with N<sub>2</sub> and added to the test autoclave. The amount of HCl was based on expected effect on the pH. In test 2, the pH was measured frequently and was kept below pH 4.0. The amount of HCl added to the autoclave, when pH adjustments were necessary, was based on a calibration curve made by adding a known amount of HCl (10%) to a predetermined amount of the electrolyte from the test autoclave. The pH calibration curve is found in Appendix C.

On completion of the test the final pH and sulfide content were measured before the H<sub>2</sub>S gas was removed, and nitrogen was purged through the autoclave for several hours to remove any H<sub>2</sub>S left. The autoclave was opened and the specimens were cleaned for two minutes in an acidic solution prepared from distilled water (500 ml), hydrochloric acid (37 %, 500 ml) and the corrosion inhibitor hexamethylenetetramine (35 g). The specimens were cleaned in ethanol and dried before they were examined optically in order to reveal surface cracking. The specimens were then sectioned along the dash lines in to Figure 24 to provide a core section in



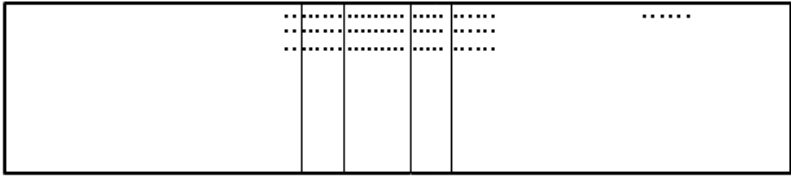
the length direction for further examinations. All specimens were ground, polished and etched before they were studied in a light microscope in both the polished and the etched condition. Crack depths were measured optically on the microscope by means of a SONY LH51 display unit.



**Figure 24:** Sectioning of the specimens was performed along the dotted lines, providing a core section in the length direction for examinations.

**3.7. Vickers hardness testing**

Vickers hardness testing of both materials was performed in a Matsuzawa DVK-1S with a force of HV5 (5 kgf). A pyramidal diamond indenter was forced into the surface of the material, by the predetermined force. After removal of the force, the diagonals of the diamond impression were measured through a measuring microscope. The hardness of the base material and the thermal weld simulated area was measured, providing a hardness profile of the HAZ. Generally, for un-welded material, the precise location and the size of the hardness impression is less important than for welds. Accurate assessments of HAZ regions require careful attention to location and size of the hardness impressions. As thermal weld simulations provide an isolated area of the HAZ, rather than a conventional weld, the hardness survey methods according to standards such as ISO 15156-2 are not be applicable to this case. Therefore, a different method for providing a hardness profile was selected and applied. The hardness impressions were made along three lines with a 1 mm interval between each measurement, starting and ending in the base metal on either side of the thermally weld simulated area as in Figure 25. [3, 54]



**Figure 25:** Position of Vickers hardness impressions in both material A and B.

### **3.8. Micro-hardness testing**

Micro-hardness testing was performed in a Leica VMHT Mot at 10gf, using a 100X objective lens. The force of 10gf was selected so that the size of the impression was smaller than the M-A constituents. If the impressions were large, the measured hardness would have been affected by the microstructure constituents surrounding the M-A constituents. The micro-hardness measurements were carried out to establish whether M-A constituents were present in the structure as Vickers hardness testing at HV5 (5 kgf) will not detect these small hard zones in the HAZ. The significance of these small hard zones in connection with SSC resistance is not well understood. Ten measurements were recorded for each material in various M-A constituents in the center of the HAZ. [7]

### **3.9. Microstructure characterization**

The sample preparation was performed in three grinding steps and three polishing steps before etching in 2 % Nital (2 % HNO<sub>3</sub>, 98 % C<sub>2</sub>H<sub>5</sub>OH). Grinding was performed on abrasive papers in the three steps listed below. Polishing was also performed in three steps on magnetic discs with diamond precipitate. After polishing, the specimens were etched for 15-18 seconds in 2 % Nital. The etchant, Nital, reveals the ferrite grain boundaries and ferrite constituents.

#### **Grinding:**

- Fine: mesh size 320
- Fine: mesh size 500
- Finish: mesh size 1200

#### **Polishing:**

- Struers Mol: 6 μm grit size
- Struers Mol: 3 μm grit size
- Struers Mol: 1 μm grit size

#### **Etching:**

- 2 % Nital (2 % HNO<sub>3</sub>, 98 % C<sub>2</sub>H<sub>5</sub>OH)

The microstructure of the base materials and the HAZ was studied by light microscopy, in a LEICA MEF4 attached with a JENOPTIK ProgRes C10 plus digital camera. The image processing program ImageAccess EasyLab was utilized to acquire images.

## 4. Results

### 4.1. Tensile properties

The average yield strength, tensile strength and the total elongation at the highest tensile force determined through tensile testing of three parallel specimens for material A and material B are in Table 7. The yield strength ( $R_{p0.2}$ ) of material A was 488 MPa, while the yield strength of material B was 576 MPa. The values are an average of the three parallel specimens tested. The yield strength and the tensile strength of both materials are above the minimum requirements for mechanical properties for F60 steels in ASTM A694, while the measured total elongation of material B is below the requirements.

**Table 7: Average results from tensile testing of material A and B.**

|                   | <b>Yield strength [MPa]</b> | <b>Tensile strength [MPa]</b> | <b>Total elongation [%]</b> |
|-------------------|-----------------------------|-------------------------------|-----------------------------|
| <b>Material A</b> | 488                         | 593                           | 20                          |
| <b>Material B</b> | 576                         | 667                           | 18                          |

From the tensile tests, stress-strain curves were recorded. The stress-strain curves reveal that material A and material B behave differently. Material A shows an upper and lower yield point, while material B shows a smooth curve. This is illustrated in the stress-strain curves of material A and material B in Figure 26 and Figure 27. In the stress-strain curves, the pale green dash line represents the yield point at 0.5 % total elongation ( $R_{t0.5}$ ), the dark green dash line represents the offset yield strength or yield strength ( $R_{p0.2}$ ), the dark blue dash line represents the upper yield point ( $R_{eH}$ ), and the pale blue dash line represents the lower yield point ( $R_{eL}$ ). The complete stress-strain curves are presented in Appendix D.

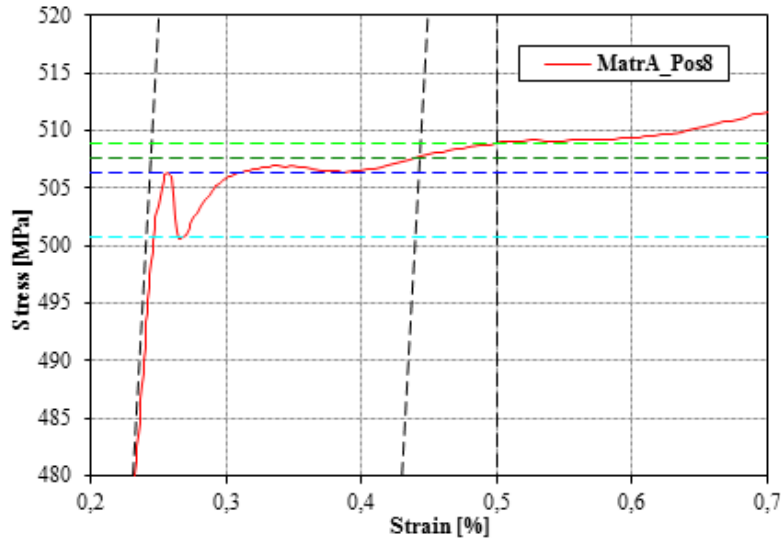


Figure 26: The yield point phenomena in a section of a stress-strain curve for material A.

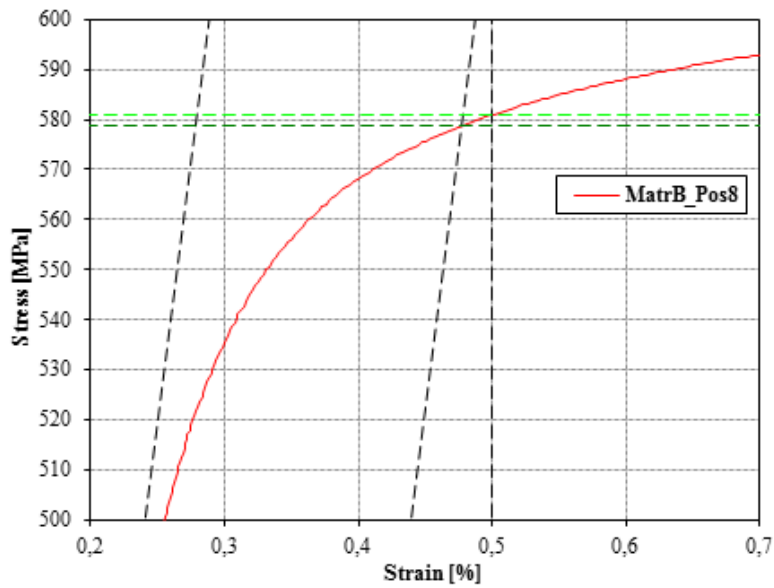


Figure 27: Section of a stress-strain curve for material B, showing a smooth curve.

Based on the stress-strain curves, the actual yield strength (AYS) of both material A and material B was determined, and two-thirds of the design SMYS of 415 MPa was found. The value for two-thirds of the design SMYS was 277 MPa. In the stress-strain curves, the AYS and the SMYS provide information about the corresponding strain. The average strain value at two-thirds of the design SMYS was similar for the two materials at 0.1337 for material A and 0.1343 for material B, while the strain at 90 % of AYS was 0.2103 for material A and 0.2870 for material B. The result from each parallel and the average values are listed in Table 8. These parameters were used when stress was applied to the FPB-specimens.

**Table 8: Two-thirds of design SMYS and 90 % of the actual yield strength (AYS) of material A and B determined from stress-strain curves.**

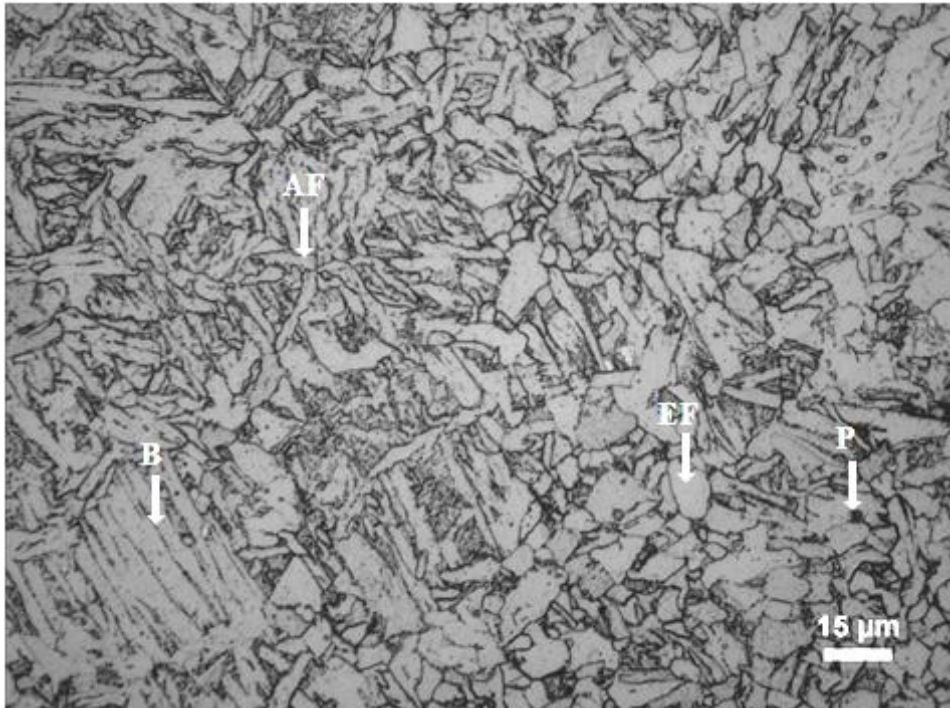
|                   | <b>Material A</b>  |                    | <b>Material B</b>  |                    |
|-------------------|--------------------|--------------------|--------------------|--------------------|
|                   | <b>2/3 of SMYS</b> | <b>90 % of AYS</b> | <b>2/3 of SMYS</b> | <b>90 % of AYS</b> |
| <b>Parallel 1</b> | 0.132              | 0.196              | 0.135              | 0.293              |
| <b>Parallel 2</b> | 0.135              | 0.219              | 0.133              | 0.278              |
| <b>Parallel 3</b> | 0.134              | 0.216              | 0.135              | 0.290              |
| <b>Average</b>    | <b>0.1337</b>      | <b>0.2103</b>      | <b>0.1343</b>      | <b>0.2870</b>      |

## 4.2. Microstructure characterization

### 4.2.1. Microstructure of base materials

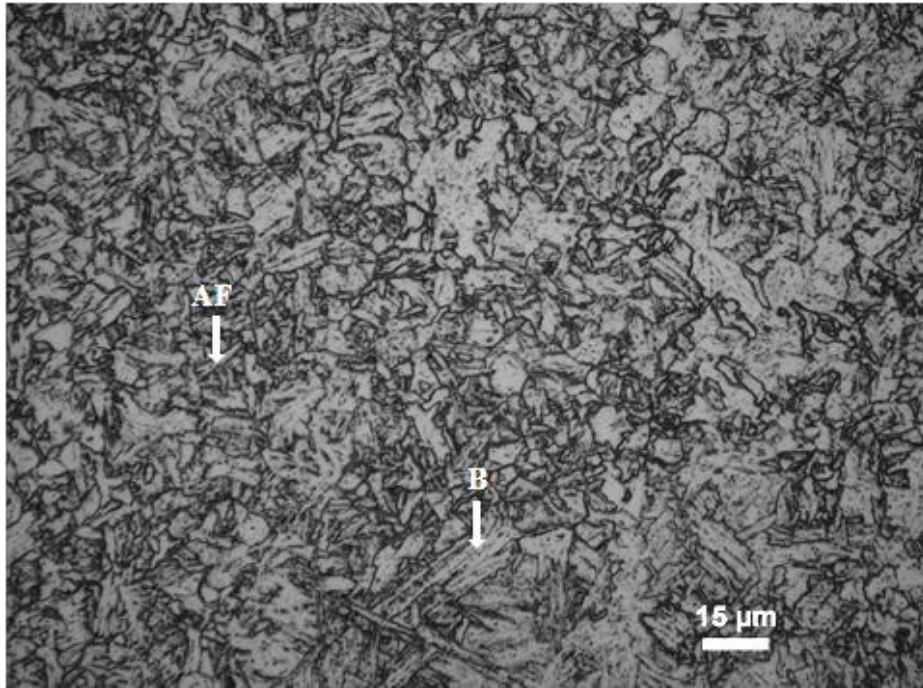
The microstructure of the base materials was documented as background for the SSC investigations, as the microstructure is an important factor for the SSC resistance of a material. The base material microstructure was also studied for reference purpose for the microstructures of the HAZ of material A and B. Micrographs were obtained by the 50X objective lens, as that pointed out the microstructure constituents most clearly. The microstructure characterization of the base materials is based upon the extensive characterization performed in the project work which led to this thesis.

The microstructure of material A at the position closest to the inner surface of the hub connector is illustrated in the micrograph in Figure 28. The microstructure mainly consists of acicular ferrite (AF), equiaxed ferrite (EF) with pearlite (P) and some bainite (B). Examples of the microstructure constituents are pointed out in the micrograph. Both acicular ferrite and bainite have lath like microstructures with a high degree of disorder, this is recognized in the micrographs. Acicular ferrite is distinguished from bainite as the laths of acicular ferrite are shorter than of bainite. The ferrite appears as rounded white grains, and the pearlite is observed as the small dark areas between the equiaxed ferrite grains.



**Figure 28: Microstructure of material A, base material. Main constituents are acicular ferrite (AF), equiaxed ferrite (EF) with pearlite (P) and some bainite (B).**

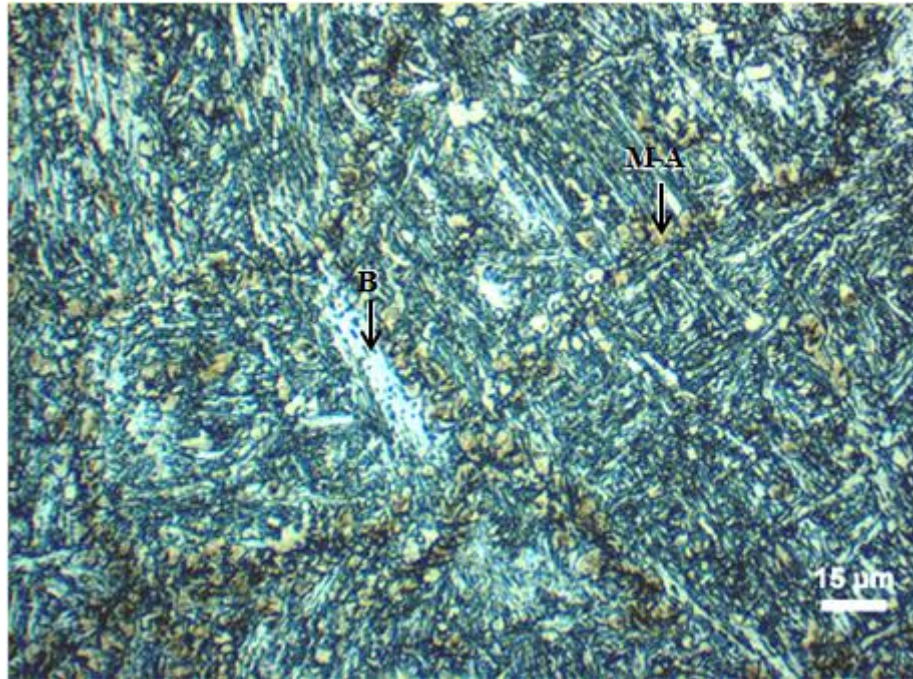
The microstructure of material B, at the position closest to the inner surface of the hub connector, is illustrated in Figure 29. The microstructure mainly consists of acicular ferrite (AF) and bainite (B) which is pointed out in the micrograph. The acicular ferrite and bainite are distinguished by the lath length. The microstructure of material B is more fine-grained, with a higher degree of disorder, than the microstructure of material A.



**Figure 29: Microstructure of material B, base material. Main constituents are acicular ferrite (AF) and bainite (B).**

#### **4.2.2. Microstructure of the heat-affected zone**

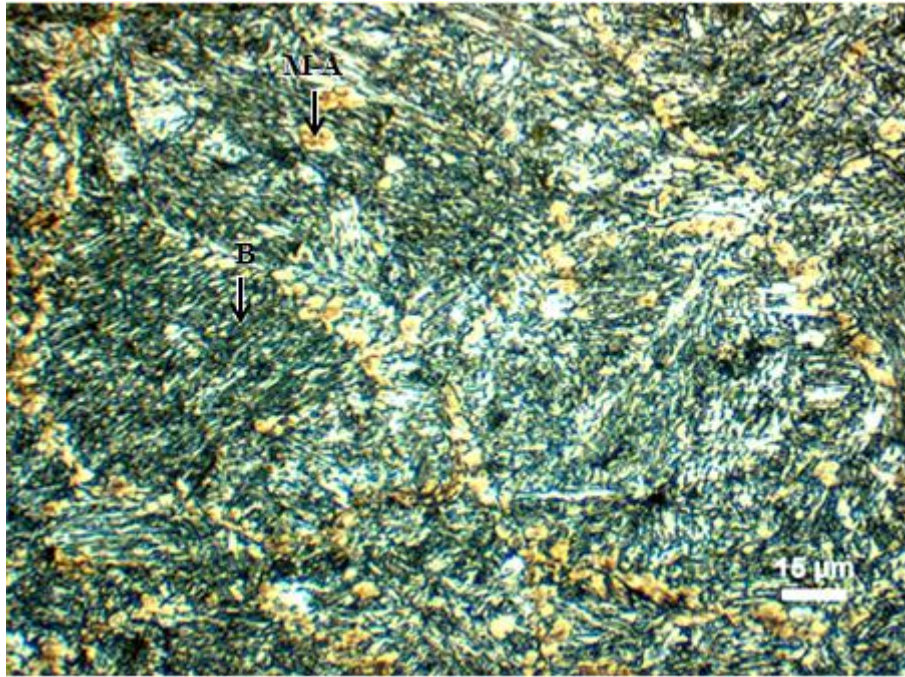
The microstructure at the center of the HAZ of material A is presented in Figure 30. The structure consists of large prior austenite grains with a lath-like structure inside the grains. The lath-like structure inside the grains is mostly identified as bainite as the laths follow the same direction. Slightly brown grains have grown along the prior austenite grain boundaries. These brown constituents are assumed to be M-A constituents, this was confirmed by micro-hardness measurements (section 4.3.3). The M-A constituents have grown in a “necklace” formation on the prior austenite grain boundaries. There is also some M-A constituents inside the grains which have grown from the lath boundaries of the bainite. The main microstructure constituents are pointed out in the micrograph. The microstructural features observed corresponds to the expected microstructure of the intercritically reheated CGHAZ.



**Figure 30: Microstructure of the HAZ of material A. Main constituents are bainite and M-A constituents along the prior austenite grain boundaries.**

The microstructure at the center of the HAZ of material B is presented in Figure 31. The microstructure consists of the same elements as the HAZ of material A, where the main constituents are bainite laths inside the large prior austenite grains. On the prior austenite grain boundaries M-A constituents have grown in a “necklace” formation. In this structure there is also some M-A constituents inside the grains, as pointed out in the micrograph, which have grown from bainite lath boundaries.





**Figure 31: Microstructure of the HAZ of material B. Main constituents are bainite and M-A constituents along the prior austenite grain boundaries.**

### 4.3. Hardness measurements

Results of the Vickers hardness measurements of the base materials, the HAZ as well as the micro-hardness measurements are presented in the following sections.

#### 4.3.1. Vickers hardness of base materials

The Vickers hardness measurements and average values of the hardness measurements of both materials are presented in Table 9. The values are an average of six measurements made with 1 mm distance. The hardness of material A is  $HV\ 214\pm5$ , while material B has a hardness of  $HV\ 249\pm2$ .

**Table 9: Vickers hardness values for both base materials.**

| <b>Parallel</b> | <b>Material A</b> | <b>Material B</b> |
|-----------------|-------------------|-------------------|
| <b>1</b>        | 214               | 242               |
| <b>2</b>        | 232               | 251               |
| <b>3</b>        | 202               | 251               |
| <b>4</b>        | 215               | 246               |
| <b>5</b>        | 214               | 252               |
| <b>6</b>        | 209               | 254               |
| <b>Average</b>  | <b>214</b>        | <b>249</b>        |

### 4.3.2. Vickers hardness profile of the heat-affected zone

The hardness profiles of the HAZ of material A and B are illustrated in Figure 32. These results indicate that the hardness profiles of material A (blue) and material B (red) in the HAZ are similar and that the hardness is highest in the center of the HAZ for both materials, in the intercritically reheated CGHAZ. Each point on the curves is an average of three parallel measurements. There are some large variations in hardness values at positions close to each other. This may be a result of the various phases in the microstructure with different hardness levels. This is further studied by the micro-hardness testing. The data for the measured hardness of both materials are presented in Appendix E. The notches in the thermal weld simulated FPB-specimens were located at the center of the specimens and thereby at the region of the highest hardness of the HAZ.

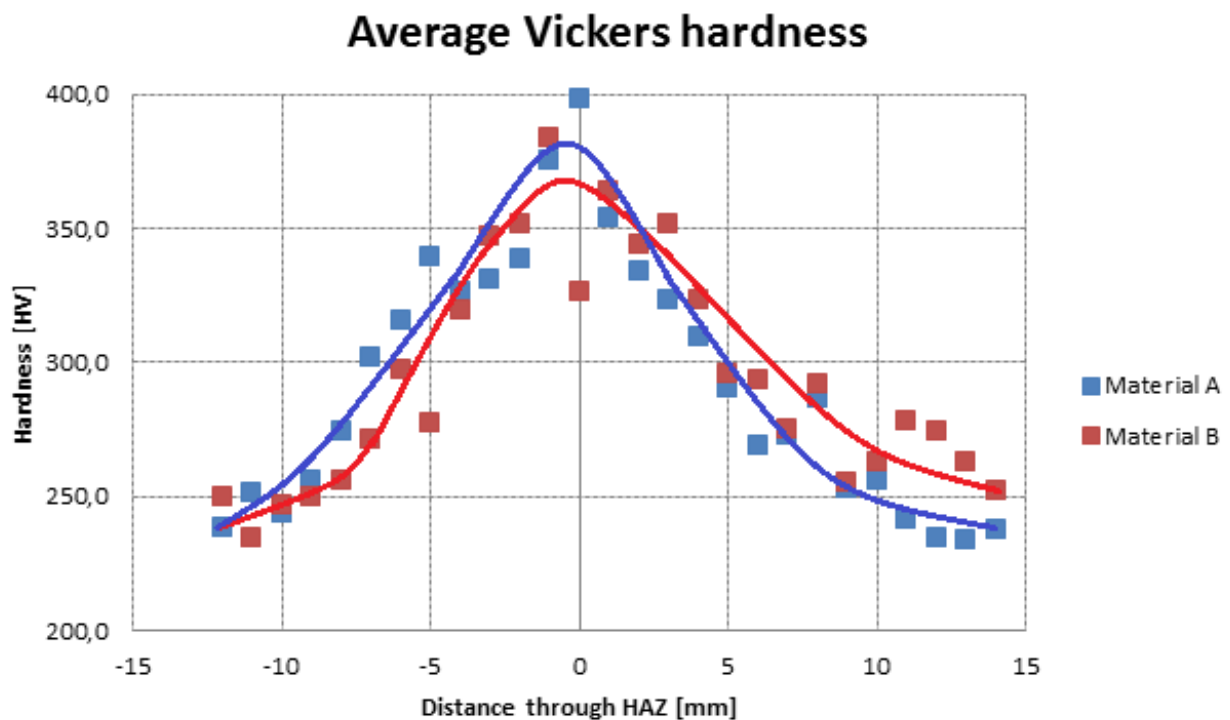


Figure 32: Vickers hardness (HV5) profile of the heat-affected zone of material A and B.

### 4.3.3. Micro-hardness measurements

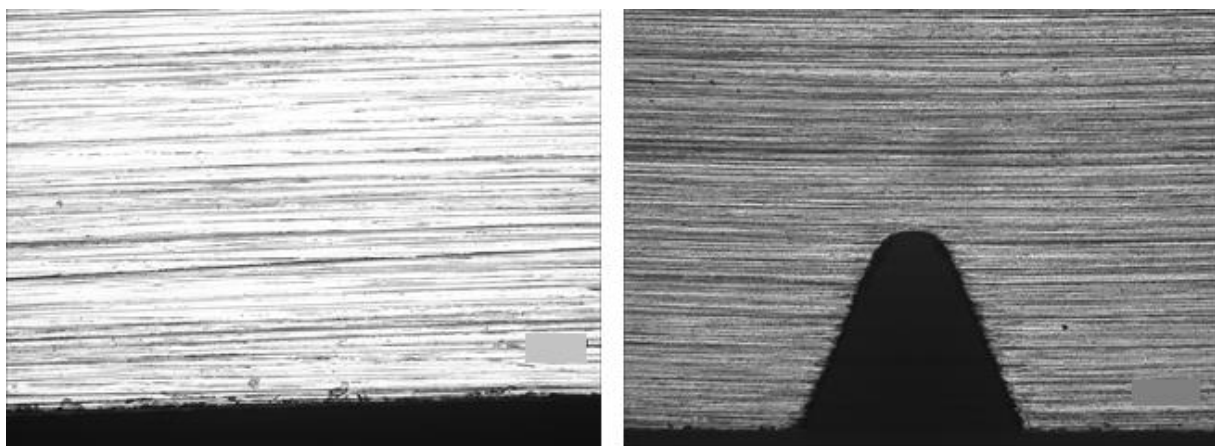
The results of Vickers micro-hardness measurements of the M-A constituents in the HAZ of both materials are presented in Table 10. The results, recorded with 10gf, range within HV 444 to HV 627 for material A and HV 467 to HV 655 for material B. The average values of the hardness of the M-A constituents in material A and material B are respectively HV 541 and HV 578.

**Table 10: Results from Vickers micro-hardness measurements of M-A constituents at 10gf.**

| <b>Material A [HV]</b> | <b>Material B [HV]</b> |
|------------------------|------------------------|
| 444                    | 467                    |
| 467                    | 525                    |
| 488                    | 534                    |
| 522                    | 538                    |
| 528                    | 580                    |
| 549                    | 607                    |
| 572                    | 610                    |
| 601                    | 623                    |
| 611                    | 640                    |
| 627                    | 655                    |
| <b>541</b>             | <b>578</b>             |

#### **4.4. Sulfide stress corrosion cracking**

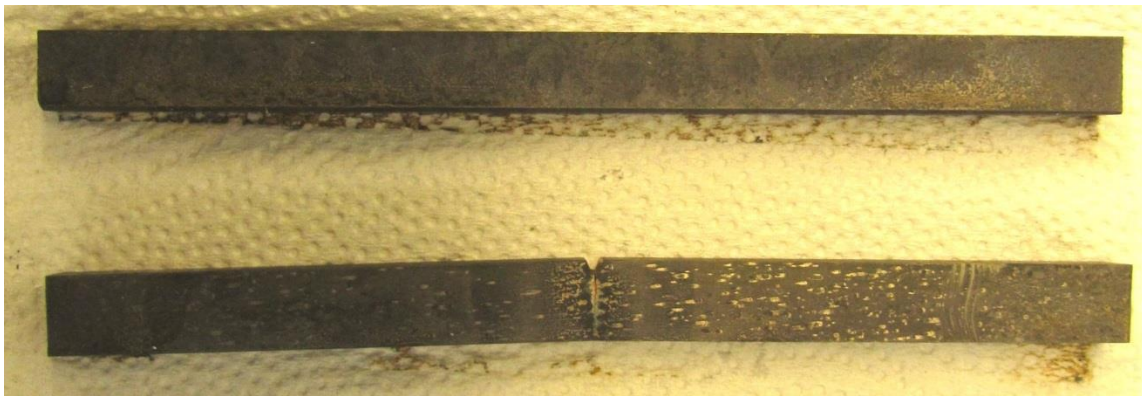
For carbon and low alloy steels, it can be difficult to distinguish SSC from localized corrosion attacks caused by CO<sub>2</sub> and H<sub>2</sub>S. General and localized corrosion caused by CO<sub>2</sub> and H<sub>2</sub>S will also take place in or near the cracks when no corrosion inhibitor is used. According to NACE TM0177 [22], the test environment may also corrode some alloys that normally would not corrode in the field environment and thereby induce failures in materials that would not have failed in service. However, specimens containing cracks after testing shall be considered failed. In NACE TM0177 it is stated that “Failure is cracking of the specimen” and “Because corrosion products may obscure cracks, a careful examination shall be made”. The standard does not state any characteristics of cracks or corrosion attacks. Nor does it provide limits for critical crack length or corrosion depth. Micrographs of one parallel of each material in each condition are included in the report. Micrographs of the further specimens are found in Appendix G. Prior to testing the process wetted side surface and the sides next to this side was free of cracks, as illustrated in Figure 33.



**Figure 33: Ground surface of base material (left) and area around notch (right) prior to testing.**

#### 4.4.1. Test 1: Sweet - Transition zone

Test 1 represented an environment in the transition between the sweet region and the transition region, providing a relatively mild test. Specimens as received from the autoclave are shown in Figure 34. The upper specimen is a sample of the base material where no cracking is observed, while the lower specimen is thermal weld simulated and notched. In the welded and notched specimen, severe cracking is observed at the notch. These two specimens represent the appearance of all the specimens of material A and material B as received from the autoclave.



**Figure 34: Specimens as received from the autoclave in test 1. Upper specimen of base material, lower specimen is thermal weld simulated and notched.**

Localized corrosion attacks with depths up to 50  $\mu\text{m}$ , were observed in two of the three parallels of base material A. In the third parallel of material A, no general or localized corrosion or cracks were observed. In base material B, localized corrosion attacks with depths up to 130  $\mu\text{m}$  were observed in all parallel specimens.

The cracks initiated in the notched samples with a simulated weld, of both material A and material B, had propagated throughout almost the entire specimen thickness. For both material A and material B, the lengths of the cracks initiated at the notches were in the range 6.5 mm to 6.85 mm. In the core section of the thermal weld simulated specimens, on both sides of the notch, some localized corrosion was observed in material A, while localized corrosion attacks and cracks were found in the core section of all parallels of material B.

The observations made by visual examination and by light microscopy are summarized in Table 11, where the crack lengths and corrosion depths listed are based on the deepest cracks and corrosion attacks measured on each specimen. All micrographs, corrosion depths and crack lengths listed are based on the findings in the core section of the specimens. The core section provides information about corrosion attacks initiated at the stressed surface of the material, which is the only surface exposed to the well fluid in service.

**Table 11: Results matrix for test 1, material A and B in the sweet/transition region.**

| <b>Material A</b> | <b>Thermal weld simulated</b> | <b>Crack lengths [mm]</b> | <b>Corrosion depths [<math>\mu\text{m}</math>]</b> | <b>Fracture morphology</b>                 |
|-------------------|-------------------------------|---------------------------|--|--|
| <b>1a</b>         | Yes                           | 6.50                      | 50   | Transgranular path and localized corrosion |
| <b>1b</b>         |                               | 6.50                      | 25   |  |
| <b>1c</b>         |                               | 6.85                      | 25   |  |
| <b>2a</b>         | No                            | -                         | 25   | Localized corrosion                        |
| <b>2b</b>         |                               | -                         | -  | No attacks                                 |
| <b>2c</b>         |                               | -                         | 50   | Localized corrosion                        |
| <b>Material B</b> |                               |                           |  |  |
| <b>1a</b>         | Yes                           | 6.70                      | 130  | Transgranular path and localized corrosion |
| <b>1b</b>         |                               | 6.70                      | 80   |  |
| <b>1c</b>         |                               | 6.55                      | 150  |  |
| <b>2a</b>         | No                            | -                         | 80   | General                                    |
| <b>2b</b>         |                               | -                         | 130  | and  |
| <b>2c</b>         |                               | -                         | 60   | localized corrosion                        |

### **Base materials**

Some general and localized corrosion caused by  $\text{CO}_2$  or  $\text{H}_2\text{S}$  is observed in both base materials. In the micrographs of both materials, material A in Figure 35 and material B in Figure 36, some small corrosion pits are evident. Such corrosion attacks are not characterized as SSC, however, SSC may initiate from these corrosion pits due to local acidification in the corrosion pits and increased stress intensity. In both micrographs, a deeper, crack-like attack is also observed. The width of these areas are relatively large which may indicate that these attacks are a result of SSC taking place at the same time as corrosion caused by  $\text{CO}_2$  and/or  $\text{H}_2\text{S}$ . This large width makes it difficult to characterize the attack and to determine whether SSC has played a role and if so whether the attack follows an intergranular or transgranular path. In contrast to material A, the corroded areas of material B appear as deeper and more branched. There were also more positions where the corrosion had taken place in material B than material A. Micrographs of the core section of all further specimens of both base materials and the HAZ are found in Appendix F. Unless otherwise stated all micrographs in these sections present the core section of the specimens.

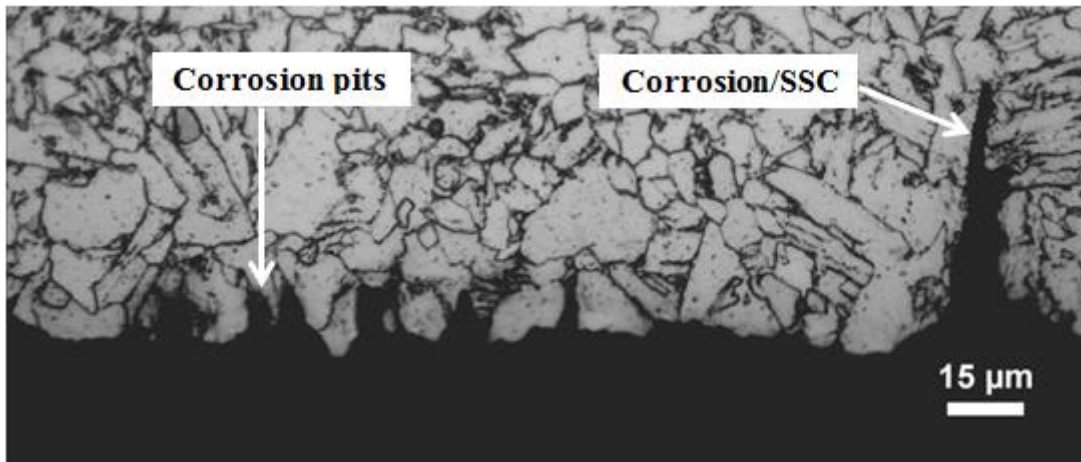


Figure 35: Corrosion attacks along the stressed side of the core section of base material A, 500X.

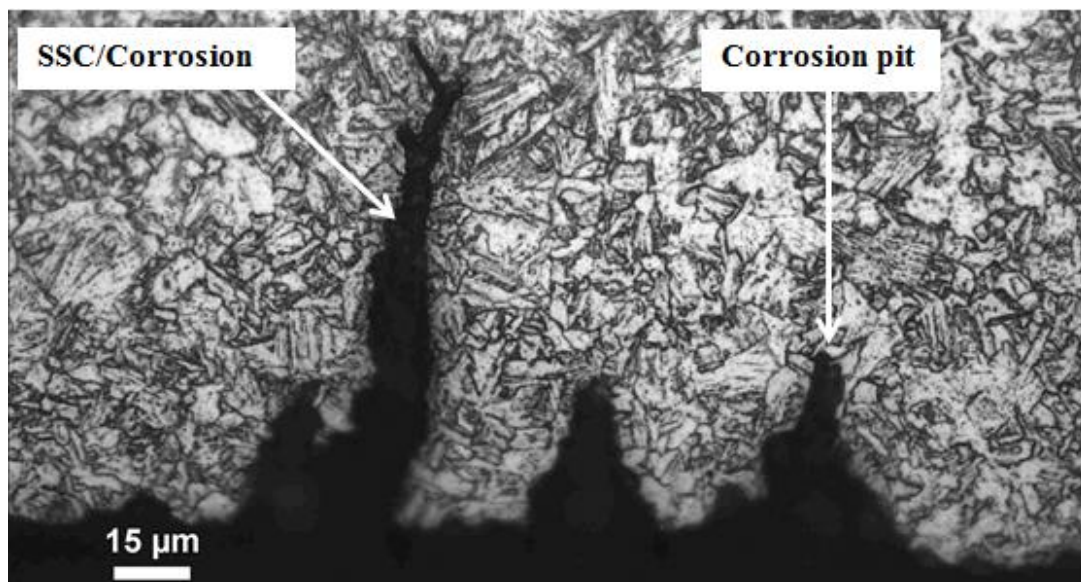


Figure 36: Corrosion attacks along the stressed side of the core section of base material B, 500X.

### Heat-affected zone

Severe cracking occurred after test 1 in the thermal weld simulated and notched specimens of both materials. In Figure 37, a specimen of material B is shown. However, it represents the appearance of all the thermal weld simulated specimens of both material A and material B from test 1. The primary crack initiated in the notch and propagated throughout almost the entire specimen thickness. Further macro photos of the cracked specimens are found in appendix F. The primary cracks, initiated from the notches in the HAZ, were studied in the polished condition by light microscopy, providing the micrographs at 6X magnification of both material A and material B in Figure 38. Some branching is observed from the primary crack, close to the notch. There are also some shorter secondary cracks initiated at the notches.



Figure 37: Macro photo of cracked specimen of simulated material B from test 1, crack lengths of 6.5 to 6.85 mm.

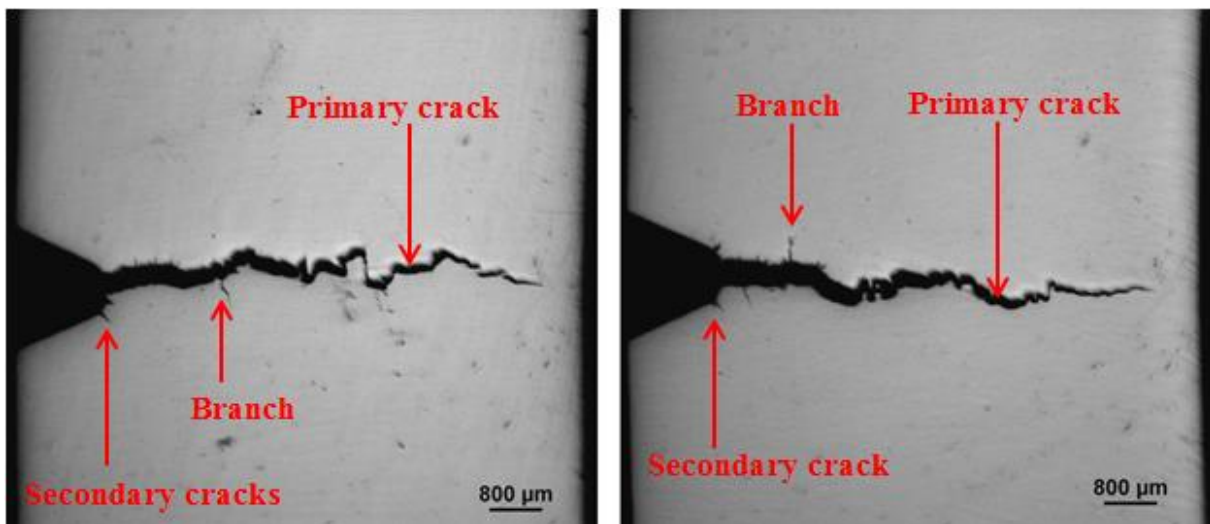
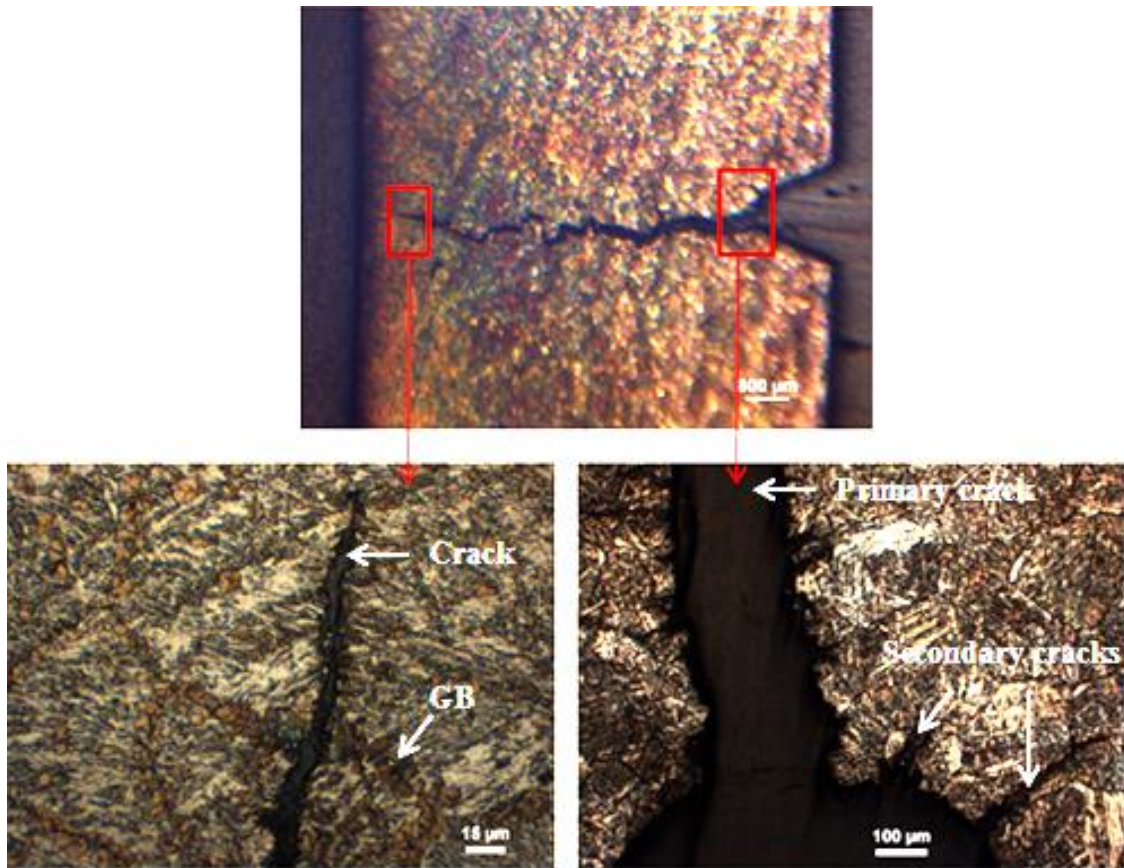


Figure 38: Cracks initiated at the notches in the thermal weld simulated specimens of material A (left) and material B (right) at 6X magnification. Crack lengths of approximately 6.5 mm.

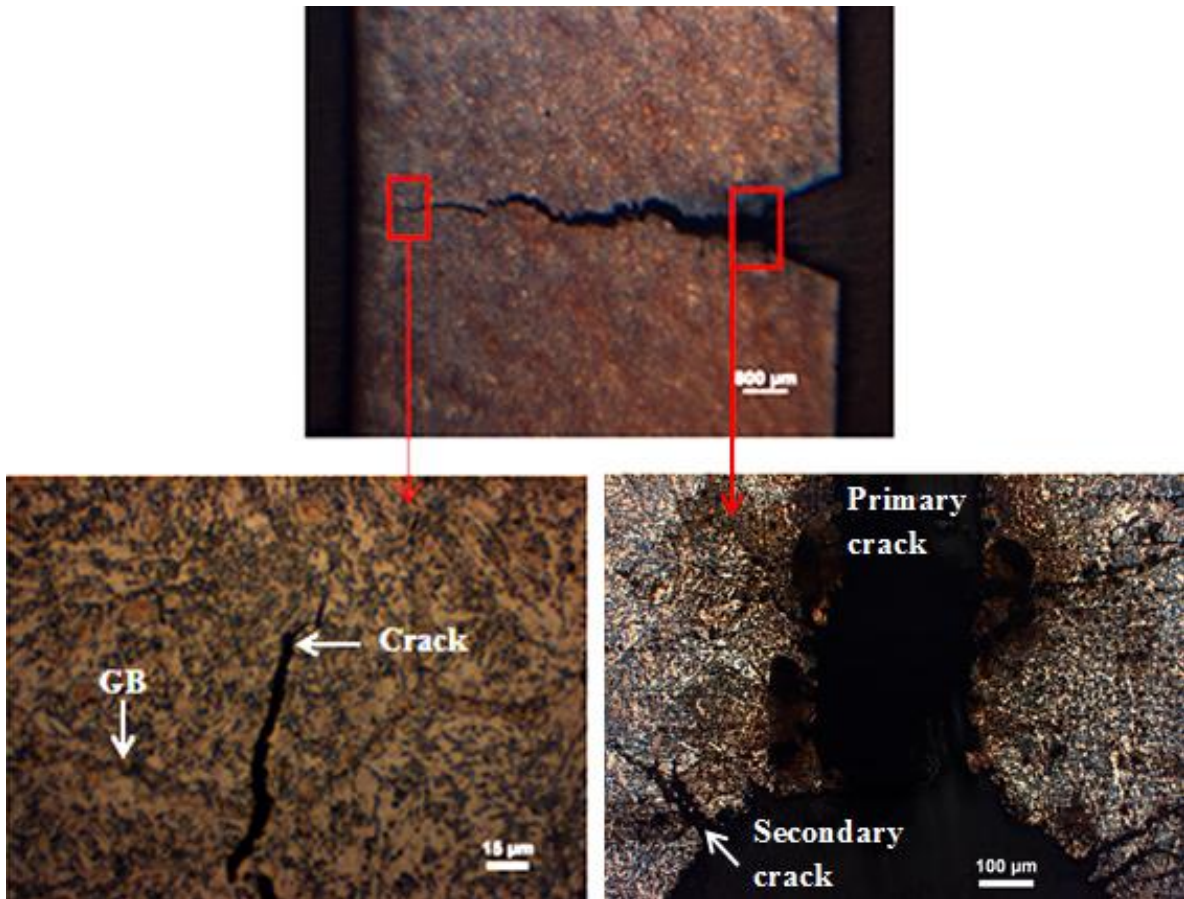
In Figure 39, an overview of the primary crack of material A is presented. In the upper micrograph of the figure, the entire specimen thickness is imaged, in the etched condition. The red squares points out which positions of the crack which are magnified in the micrographs below. In the lower left micrograph the crack end reveals that the cracking is transgranular, not following the prior austenite grain boundaries with M-A constituents along them. The SSC propagate in the direction perpendicular to the applied stress. To the right, the area where the crack initiated is magnified, showing the width of the primary crack and two secondary cracks also initiated at the notch. The secondary cracks also follow a transgranular path. The most important features, such as the primary crack, the secondary cracks and the grain boundaries (GB) are pointed out in the figure.



**Figure 39: Overview of SSC initiated at the notch in the HAZ in material A in test 1. End of crack (left) and initiation point with both primary and secondary cracks (right).**

In Figure 40, an equivalent overview of the primary crack, initiated at the notch, of material B is presented. In the upper micrograph of the figure, the entire specimen thickness is imaged, revealing that the crack propagate throughout most of the specimen thickness. The red squares points out which positions of the crack which is magnified. In the lower left micrograph, the end of the crack reveals that the cracking follows a transgranular path. To the right, the initiation point of the primary crack is magnified, showing the width of the primary crack and the secondary cracks, initiated at the notch, at both sides of the primary crack. The secondary cracks also follow a transgranular path. The most important cracks and microstructural features, such as the primary and secondary cracks and the grain boundaries (GB), are pointed out in the figure.





**Figure 40: Overview of SSC initiated at the notch in the HAZ of material B in test 1. End of crack at the left and initiation point of both primary and secondary cracks to the right.**

In the HAZ of material A, crack-like attacks with a larger width than the SSC attacks of material B occurred. This is illustrated in Figure 41 for material A and Figure 42 for material B. These localized corrosion attacks and cracks were observed along the stressed side of the specimen outside the notch. The attacks of material A appear to be caused by both SSC and localized corrosion caused by  $H_2S$  or  $CO_2$ , even though the appearance of the attacks are crack-like the width of the attacks are relatively large. The attacks on material B appear to be SSC. When comparing all the parallel specimens, it was observed that more and deeper corrosion attacks and cracks were observed along the stressed side of the specimens in material B than in material A. The crack paths appear to be transgranular in both materials. Some of the corrosion attacks seem to have initiated at the M-A constituents along the prior austenite grain boundaries, while only some of them seem to have propagate along these grain boundaries.

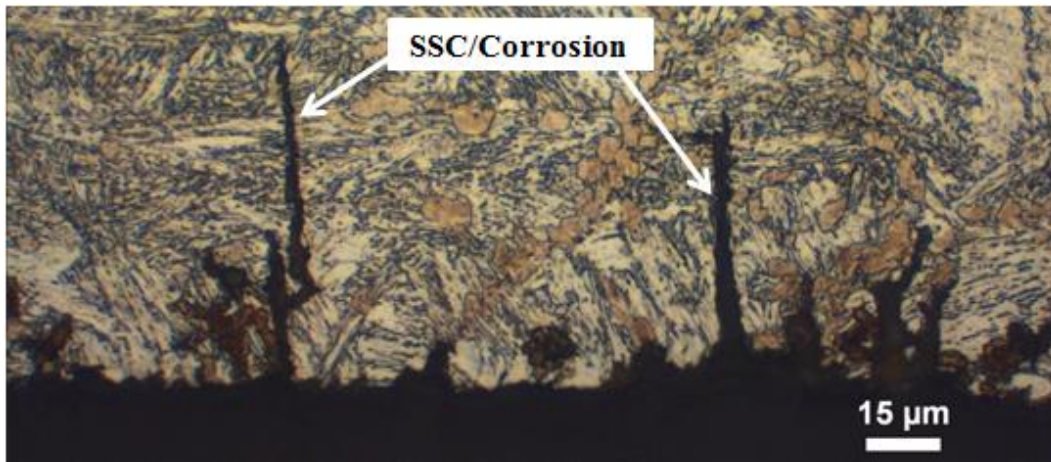


Figure 41: SSC at the core section along the stressed side of thermal weld simulated material A in test 1.

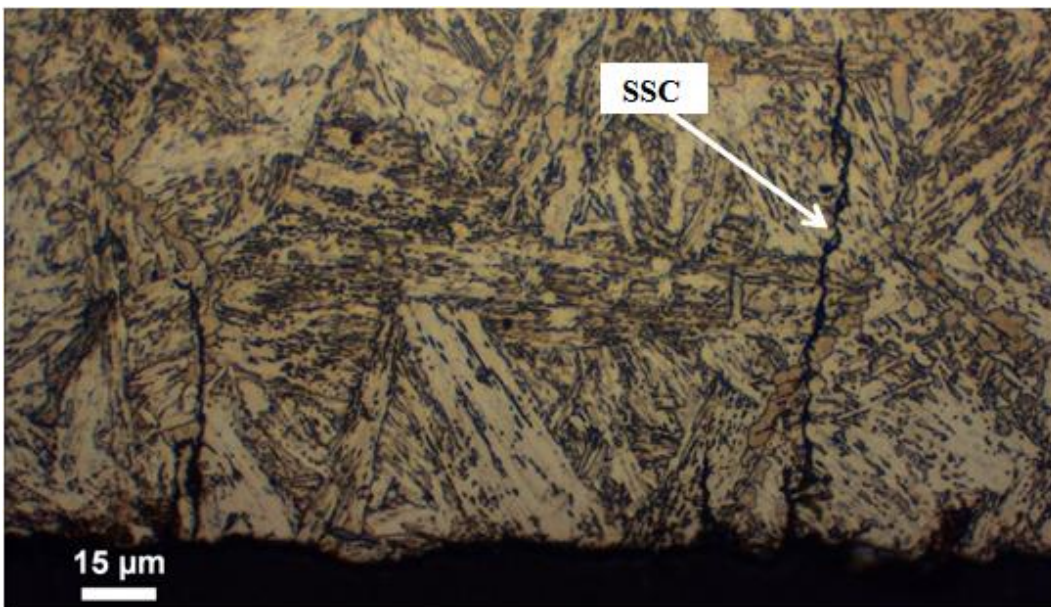


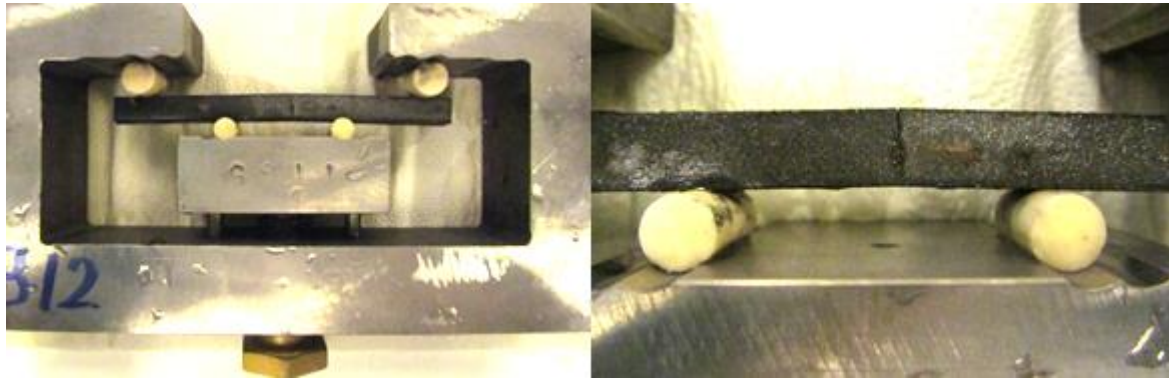
Figure 42: SSC at the core section along the stressed side of thermal weld simulated material B in test 1.

The observations reveal that material A, both in the base material condition and in the HAZ, was less severely attacked by corrosion and SSC than material B. In material B, several more and deeper localized corrosion attacks had occurred. Some of the attacks along the stressed side of the specimen in the HAZ of material B was also more clearly caused by SSC, while the attacks in material A were dominated by localized corrosion caused by CO<sub>2</sub> and H<sub>2</sub>S.

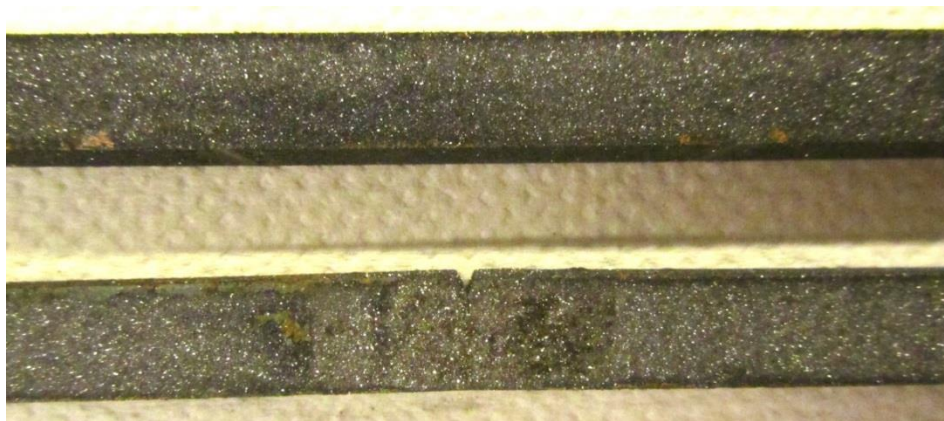
#### 4.4.2. Test 2: Sour service region

The conditions in test 2 made this test a severe test, in the sour service region. An as received base material specimen, still under stress in the jig is presented in Figure 43. The photos illustrate the bending stress which the specimens were subjected to and the severity of the cracking. Specimens as received from the autoclave of both materials are presented in Figure

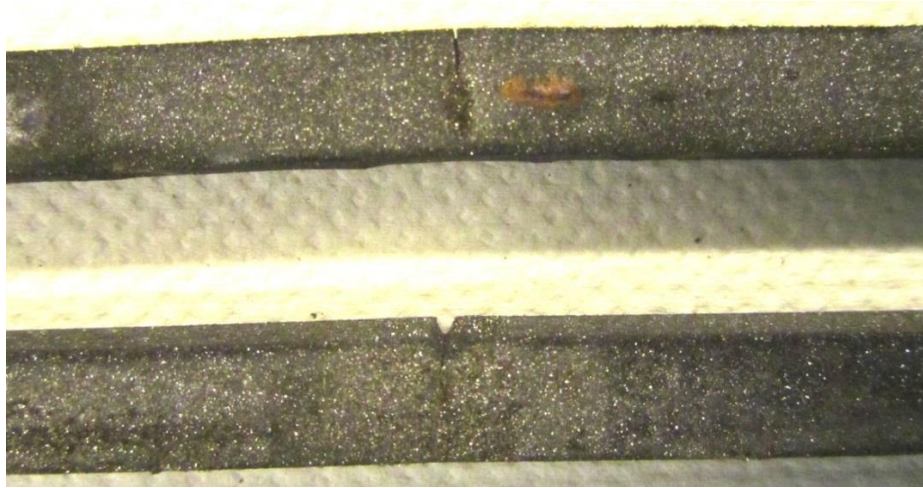
44 and Figure 45. The four specimens in the two images represent the four cases investigated in test 2. In Figure 44, a specimen of base material A and a specimen of the HAZ of material A are presented. The black corrosion product deposited on the specimens makes it difficult to see the cracks. In Figure 45, the two equivalent cases of material B are presented. The cracks, both in the base material and in the HAZ, can be observed more clearly.



**Figure 43: Specimens as received from the autoclave still under stress in the jig.**



**Figure 44: Specimens as received from the autoclave in test 2. Base material A (upper specimen), HAZ of material A (lower specimen).**



**Figure 45: Specimens as received from the autoclave in test 2. Base material B (upper specimen), HAZ of material B (lower specimen).**

Sever cracking and corrosion attacks were observed in all specimens. The appearance of the cracks in the two base materials was somewhat different. In base material A, there was a high density of cracks along the stressed side of the specimen when, studied by visual observation. In base material B, the density of cracks was smaller, while one deep crack, which had propagated throughout most of the specimen thickness, was observed. In both materials, corrosion pits and cracks with depths of 200  $\mu\text{m}$  to 300  $\mu\text{m}$  were observed. The deep cracks in the specimens of material B were approximately 7.0 mm long.

All thermally weld-simulated and notched specimens, of both material A and material B were fully separated by the cracks initiated at the notches. Along the stressed side of the specimens, on each side of the notch, localized and general corrosion was observed with a depth into the material of up to 200  $\mu\text{m}$ . Observations made by visual examinations and by optical light microscopy are summarized in Table 12. Also in this test, all micrographs, crack lengths and corrosion depths are based upon the most severe attacks observed in the core sections of the specimens.

The fracture paths in the specimens which experienced SSC were characterized as transgranular. Besides the SSC, both materials were subjected to corrosion, both general and localized, caused by  $\text{CO}_2$  and/or  $\text{H}_2\text{S}$ .

Table 12: Results matrix for test 2, material A and B in the sour service region.

| Material A        | Thermal weld simulated/ Notch | Crack lengths [mm]      | Corrosion depths [ $\mu\text{m}$ ] | Fracture morphology                                |
|-------------------|-------------------------------|-------------------------|------------------------------------|--|
| 3a                | Yes                           | Full specimen thickness | -                                  | Transgranular path and general/localized corrosion |
| 3b                |                               |                         | -                                  |  |
| 3c                |                               |                         | 160                                |  |
| 4a                | No                            | 2.5                     | 280                                | Localized corrosion                                |
| 4b                |                               | 2.5                     | 280                                |  |
| 4c                |                               | 2.0                     | 240                                |  |
| <b>Material B</b> |                               |                         |                                    |  |
| 3a                | Yes                           | Full specimen thickness | -                                  | Transgranular path and general corrosion           |
| 3b                |                               |                         | -                                  |  |
| 3c                |                               |                         | 200                                |  |
| 4a                | No                            | 7.05                    | 200                                | Transgranular path and localized corrosion         |
| 4b                |                               | 7.45                    | 380                                |  |
| 4c                |                               | 7.40                    | 300                                |  |

### Base materials

Corrosion and cracking were observed in both base materials on a macro level. Base material A in Figure 46, has a high density of cracks initiated at the stressed side, while base material B in Figure 47, has experienced cracking where one deep crack initiated at the center, with some localized corrosion attacks along the stressed side. Both materials are severely attacked, however it appears as the SSC attack of material B is more severe than the corrosion attacks of material A. This is based on the crack in the center of material B which has propagated throughout most of the specimen thickness. Macro photos of the further specimens are found in Appendix F.

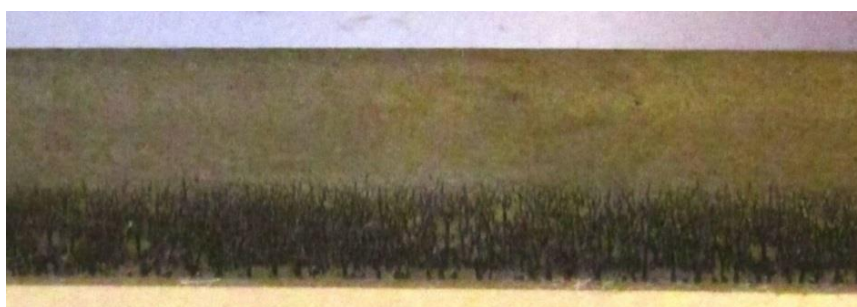
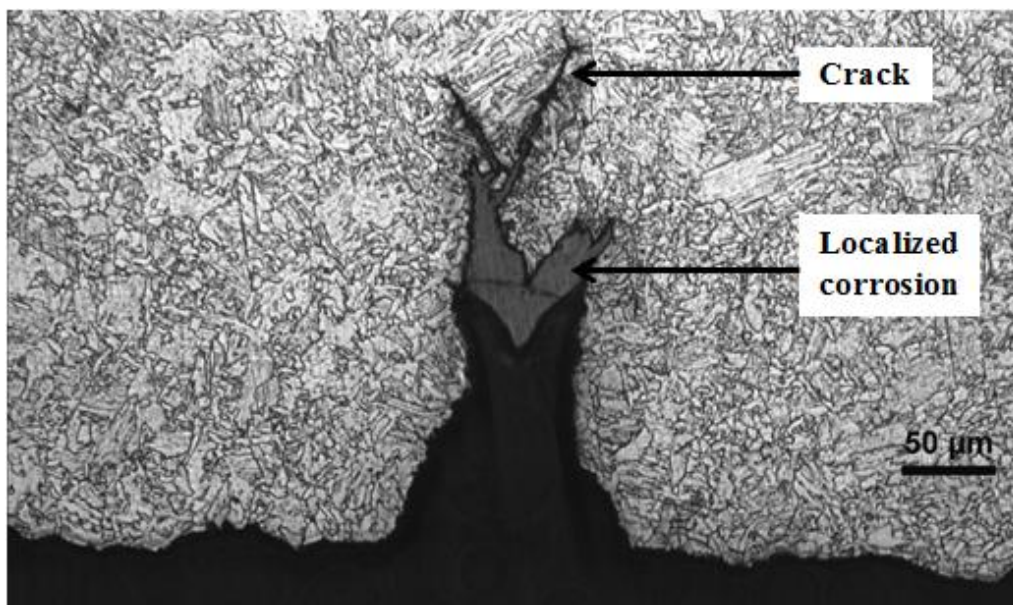


Figure 46: Macro photo of base material A, specimen from test 2. Severe cracking observed.

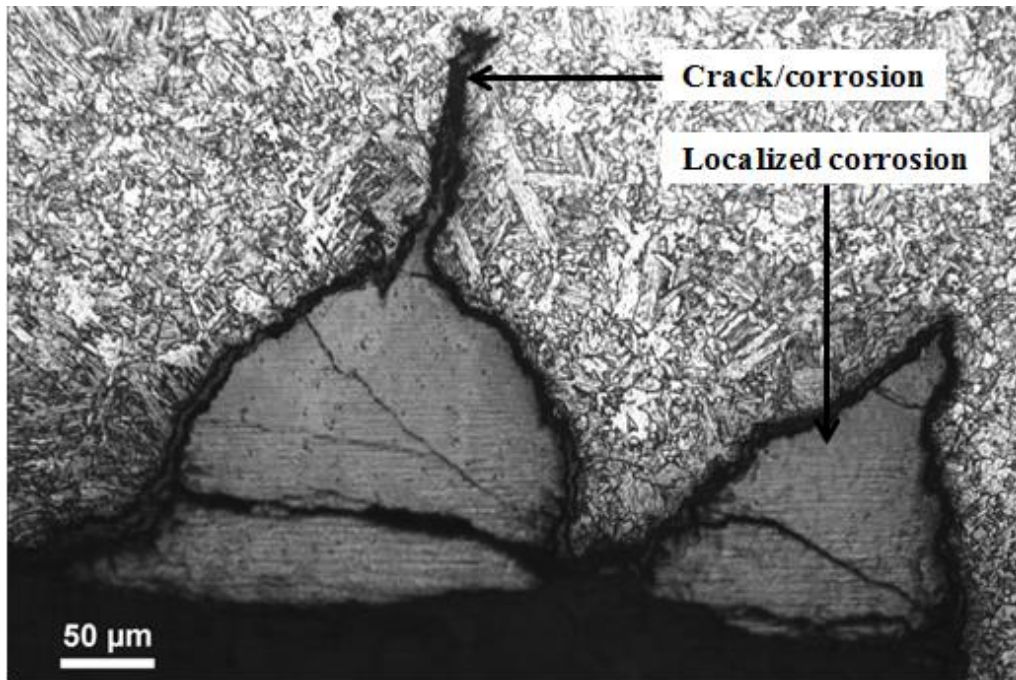


**Figure 47: Macro photo of base material B, specimen from test 2. Severe cracking observed.**

General and localized corrosion caused by  $H_2S$  and/or  $CO_2$  and some cracking initiated in the corrosion pits are observed in both base material A in Figure 48 and in base material B in Figure 49. Such corrosion and cracking as in the micrographs appeared along the entire stressed side of the specimen in the core sections. The appearance of the corrosion attacks along the stressed sides of the material B specimens were more rounded and blunt than for material A.

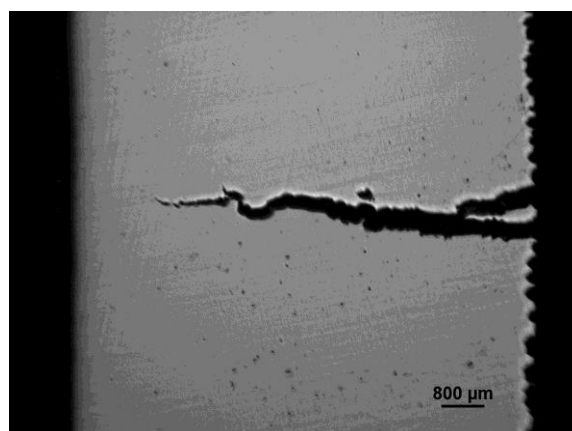


**Figure 48: Localized corrosion at the core section of base material A along the stressed side in test 2.**

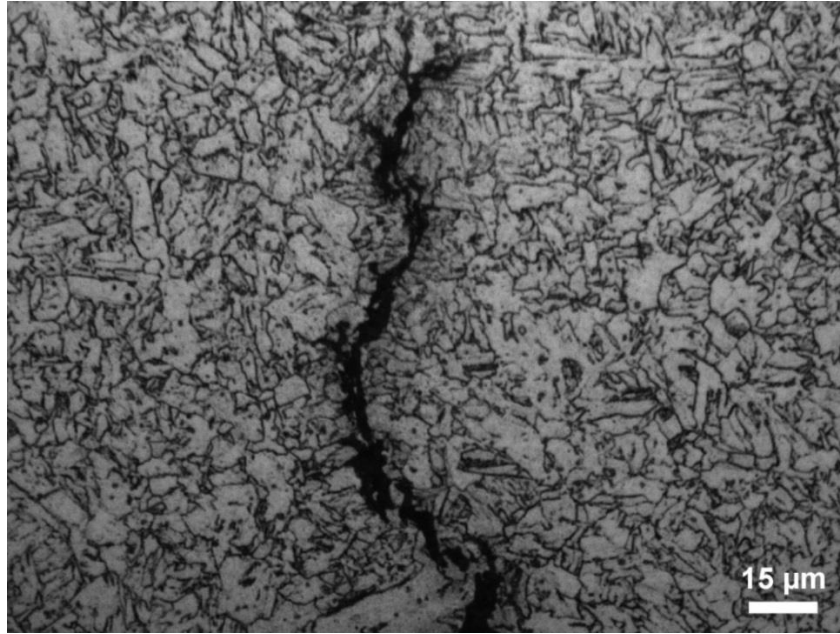


**Figure 49: Localized corrosion at the core section of material B along the stressed side, in test 2.**

An overview of the primary crack of base material B in test 2 is presented in Figure 50. The specimens experienced localized severe cracking even though they were un-notched. The cracks had a length of 7.05 mm to 7.45 mm. The photo also reveals that the material has been exposed to corrosion along the stressed side of the specimen on each side of the primary crack, as described and illustrated above. Based on the micrograph of the end of the primary crack of base material B in Figure 51 it is difficult to determine the fracture morphology. The difficulties in determining the fracture morphology is caused by the fine-grained microstructure and the relatively thick crack. However, the crack path is more likely to be transgranular.



**Figure 50: Overview of base material B specimen. Crack length of approximately 7 mm.**



**Figure 51: End of primary crack in base material B in test 2, transgranular fracture path.**

### **Heat-affected zone**

The cracks initiated at the notch, of all thermally weld simulated specimens of both material A in Figure 52 and material B in Figure 53, had propagated throughout the entire specimen thickness, separating all specimens into two. The specimens are black as a result of the corrosion product deposited at the surfaces. Since the specimens failed the tests, the microscopy examinations were reduced to one specimen of each material.



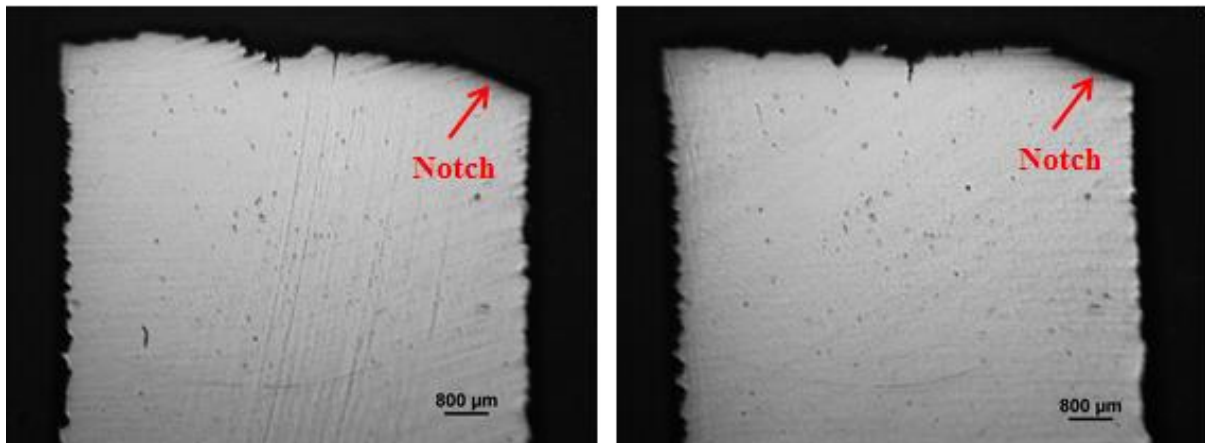
**Figure 52: Macro photo of the HAZ of material A from test 2. Specimen fully separated by cracking.**





**Figure 53: Macro photo of the HAZ of material B from test 2. Specimen fully separated by cracking.**

The notched intercritically reheated CGHAZ of both materials were, as described above, fully separated in test 2. The cross-section of the full thickness fracture of both material A and material B in Figure 54 reveals some branching from the primary crack. The branches were studied to provide information about the fracture path of the primary cracks.



**Figure 54: Fully separated specimens of material A (left) and material B (right) at 6X magnification.**

As the specimens of the HAZ of both material A and material B were fully separated by cracking in the sour service test it was difficult to determine the fracture morphology of the primary cracks. It appeared as the fracture morphology of the branching from the primary cracks corresponded to the fracture morphology of the primary crack. The branched cracks had propagated in a transgranular manner in both material A as illustrated in Figure 55 and material B as in Figure 56. The cracks have propagated across the prior austenite grain boundaries.

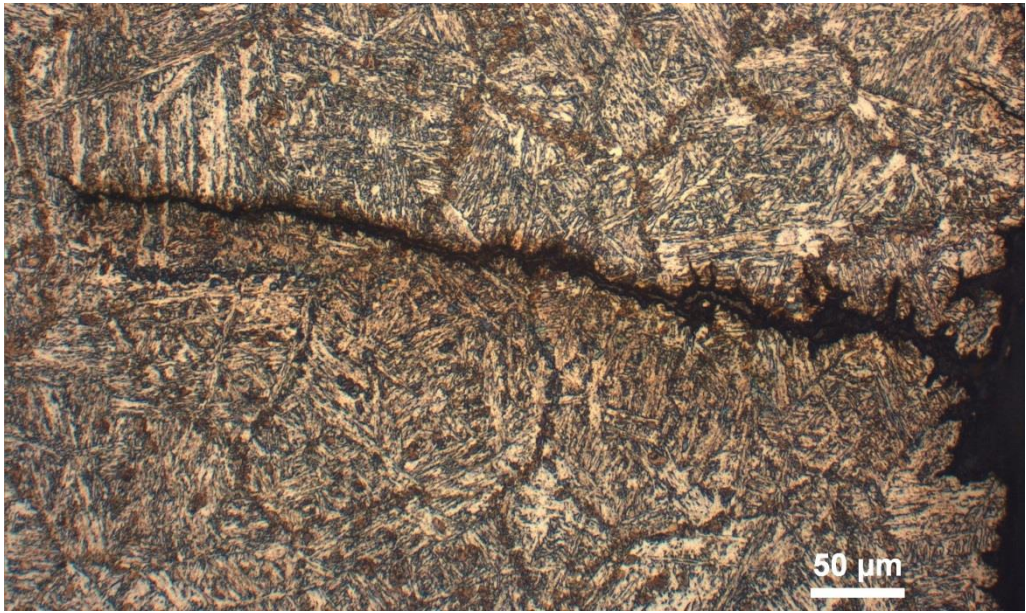


Figure 55: Transgranular branching from the primary crack of the HAZ of material A in test 2.

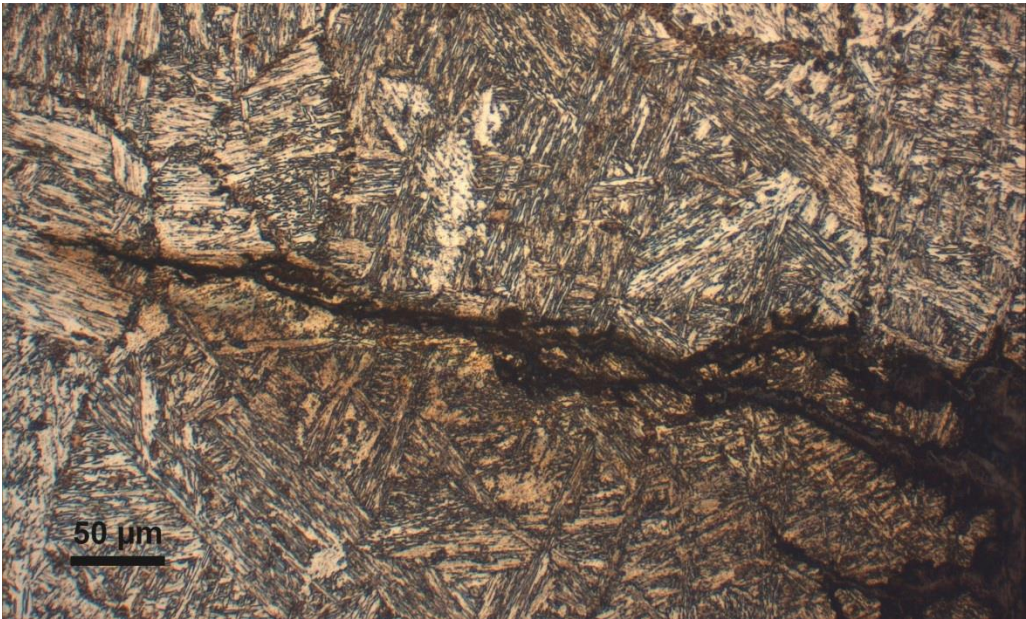


Figure 56: Transgranular branching from the primary crack of the HAZ of material B in test 2.

In the HAZ of material A, corrosion products are observed along the entire stressed side of the specimen as in Figure 57, in addition to the primary crack initiated at the notch. According to the appearance of the corrosion products along the stressed side of the materials, the corrosion of material A appears as general/localized corrosion caused by CO<sub>2</sub> and/or H<sub>2</sub>S. For material B in Figure 58, corrosion products were deposited along the entire stressed side of the specimen. The corrosion attacks are assumed to be general corrosion caused by CO<sub>2</sub> and/or H<sub>2</sub>S.

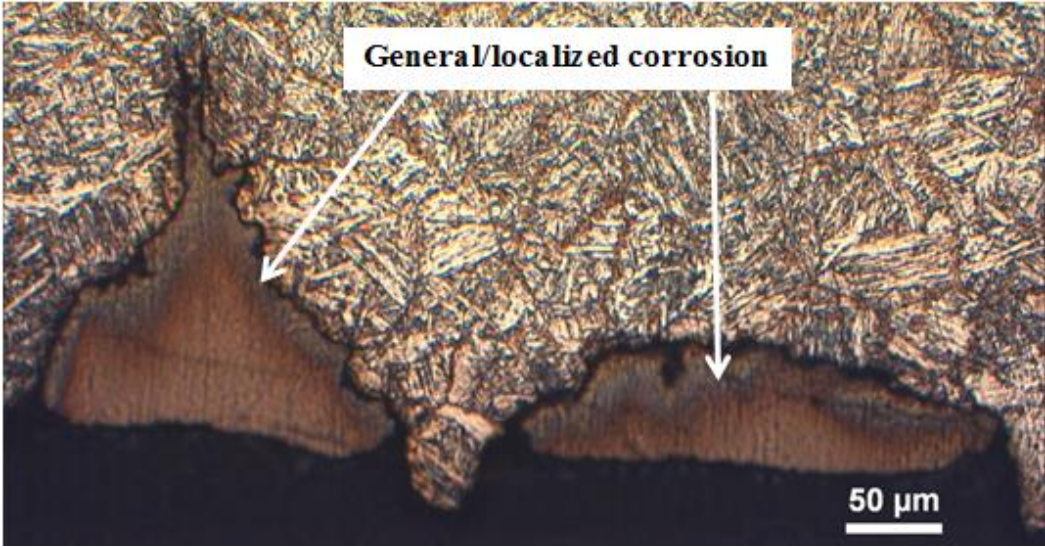


Figure 57: General/localized corrosion attacks along the stressed side of the core section of HAZ A, test 2.

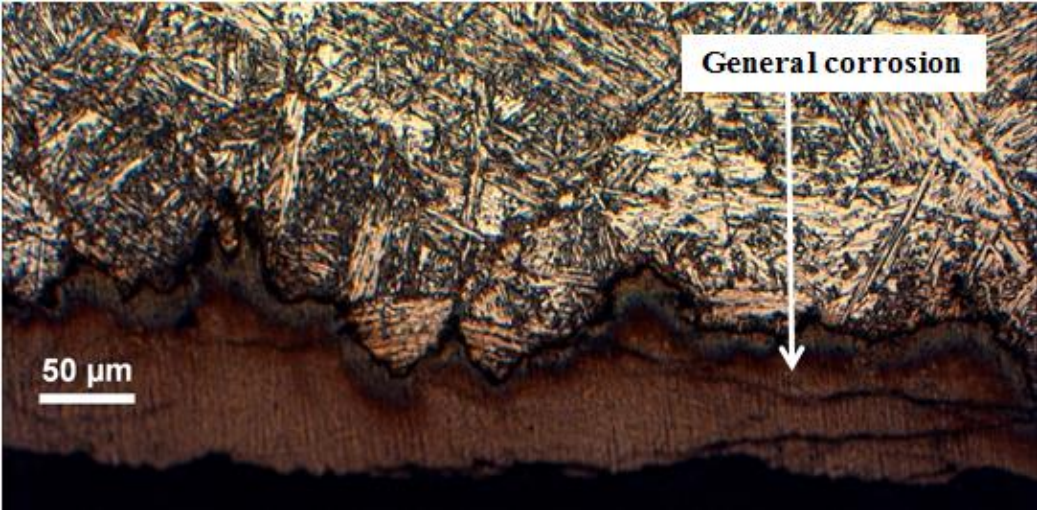


Figure 58: General corrosion attacks along the stressed side of the core section of HAZ B, test 2.



## **5. Discussion**

### **5.1. General discussion**

#### **5.1.1. Yield point phenomena**

The yield point phenomenon is commonly observed in mild steels. The results from the tensile test showed that the yield point phenomenon only exists in material A, while material B has a smooth transition from elastic to plastic deformation. This may be a result of the variations in microstructure components between the two materials as the yield point phenomena is observed in materials with low dislocation density. Material A consists of more ferrite than material B, which consists mainly of acicular ferrite. Ferrite has a lower dislocation density than acicular ferrite. These microstructural differences may have caused the yield point phenomena in material A, and not in material B. [55]

#### **5.1.2. Hardness**

There were some large variations in hardness values of the equivalent positions in the HAZ of both materials. This may be a result of the brittle phases (M-A constituents) which exists along the prior austenite grain boundaries and some along the bainite lath-boundaries inside the prior austenite grains. However, the results reveal the trend of the hardness profile over the entire HAZ and are representative for the actual HAZ hardness of the steels. The additional micro-hardness measurements provided complementary information of the hardness. It is reasonable to assume that the hard M-A constituents have affected the hardness measurements and also affects the SSC resistance of the materials.

The micro-hardness measurements revealed that the hardness of the areas assumed to be M-A constituents in the HAZ is at about 450 HV to 600 HV for both materials. This is in consistence with the hardness of M-A constituents which usually exists between 400 HV and 600 HV. This confirms that the constituents along the prior austenite grain boundaries are M-A constituents. The variations in the measured hardness values may be a result of the size of the M-A constituents, where the impressions were made and at what position in the M-A constituent the impression was made. If the impression is made at the surface of the constituent and not at the center, this may affect the recorded hardness value. An impression made at the center of a constituent is less affected by the hardness of the surrounding matrix. An impression at the surface may be affected by the lower hardness of the matrix surrounding the M-A constituent which may have yielded due to the impression. Variations in hardness values may also be a result of variations in carbon content in the M-A constituents of various steels. The carbon content is affected by the peak temperature of the second thermal cycle. A high peak temperature would, according to the iron carbon phase diagram, provide a lower carbon content and thereby lower hardness.

## **5.2. SSC resistance**

For carbon and low alloy steels it can be difficult to distinguish SSC from localized corrosion caused by CO<sub>2</sub> and/or H<sub>2</sub>S. The acceptance criteria stated in ISO 15156-2 only says that, “No cracks in accordance with NACE TM0177 assessment method” are accepted. This criterion is the basis for the evaluations of SSC resistance in the various conditions in this report. Neither ISO 15156-2 nor NACE TM0177 provides any definitions or examples of cracks and pits which makes the SSC resistance assessments more difficult. There are several factors that influence the SSC resistance, making the assessment of SSC of the materials a complex issue. It is also difficult to separate the effect of the various parameters. [7]

### **5.2.1. Base materials**

Base material A is not considered highly susceptible to SSC under the mild conditions in test 1. The corrosion attacks observed, in base material A, are mostly considered as localized corrosion caused by CO<sub>2</sub> and/or H<sub>2</sub>S. However, some deeper attacks which indicate the combined action of SSC and corrosion makes it necessary to make modifications or precautions before these materials are applied to such environments as tested. The localized corrosion attacks may also evolve over time, and SSC may initiate in the pits as a result of local acidification and increased stress intensity in the pits. This may be affected by whether the local corrosion attacks have a sharp or blunt end. Therefore the corrosion attacks cannot be neglected.

Base material B experienced more corrosion damage than material A, in test 1. There were more corrosion attacks along the stressed side of the specimens and the localized corrosion attacks were deeper than for material A. Also for material B, the deepest attacks indicate that SSC and corrosion has taken place at the same time. The deepest attacks also revealed some branching and sharper ends of the pits which may evolve further into the material. The more severe corrosion attacks of material B, when compared to material A, may be a result of the higher hardness of material B than material A and the microstructural differences. These effects are further discussed in section 5.4.1 and section 5.4.2.

In test 2, the appearance of the corrosion attacks on the two materials are quite dissimilar. Material B is considered to be more severely attacked due to the deep primary crack approximately at the center of the specimens. Material A however, experience more attacks along the stressed side of the specimens relative to material B. The attacks of material A are mostly localized corrosion caused by CO<sub>2</sub> or H<sub>2</sub>S and some cracks have initiated in the corrosion pits. The severity of the attacks makes both materials considered unsuitable for sour service applications. The differences in the severity of the corrosion and SSC attacks may be a result of the variations in hardness and microstructure of the two materials, these two factors are closely related to each other.

The corrosion attacks observed in both base materials after test 1 are small relative to the attacks in test 2. This is reasonable as test 2 provides a much more severe environment than test 1. The corrosion attacks and cracks cannot be neglected on the basis of that a laboratory test only simulates the field conditions, and fails to reproduce every factor from the actual

service. Any evidence of SSC and severe localized corrosion in the tests is an indication of the possibility for further cracking, which may eventually cause catastrophic results. On the other hand, many small blunt cracks and localized corrosion attacks may not be detrimental to the materials. Small blunt cracks may rather provide a stress relief contributing to decreased global stress in the materials. Such a stress relief would reduce the risk for SSC as the applied stress is a factor affecting the SSC resistance. Small blunt cracks may therefore, in some cases, have a beneficial effect on the SSC resistance of the materials.

Material B is more susceptible to corrosion caused by CO<sub>2</sub> and/or H<sub>2</sub>S than material A, this is revealed for the base materials in both tests. This is based on the observations of several more and longer corrosion attacks in material B than in material A. This will be discussed in the following sections.

### **5.2.2. Heat-affected zone**

The thermal weld simulated specimens may be considered as fully separated by cracking in test 1, although they were not fully separated. The most probable reason why the cracks of the thermal weld simulated specimens are of the same length and why the cracks did not actually propagate throughout the whole specimen thickness is that there was no more load on the specimens at the end of the test period. In test 2 the specimens were fully separated by SSC. Based on these results it is clear that the materials are not suitable for sour service applications when a notch or equivalent weld defect is present in the intercritically reheated CGHAZ. It is evident that the hardness of the HAZ is in significant noncompliance with the specified maximum hardness requirements for steels exposed to H<sub>2</sub>S rich environments. The severe cracking is therefore not an unexpected result for the HAZ specimens. This will be discussed further in section 5.4.1.

The thermally weld simulated specimens of both materials behaved similar and provided the same results regarding the primary cracks initiated at the notches. This indicates that material A and material B may be equally susceptible to SSC in the thermal weld simulated condition. This is reasonable since the materials exhibit the same hardness profiles and seemingly the same microstructural properties in the HAZ. All the specimens were also subjected to the same environment. However, some differences in corrosion attacks were observed in the core sections along the stressed side of the specimens on both sides of the notches. This revealed more and longer crack-like attacks on material B than on material A. Since the hardness and microstructural parameters are the same, some other parameters have affected the corrosion resistance of the materials. It is assumed that the applied stress may be the reason for the observed differences, as the specimens were subjected to a stress level relative to the AYS of the base materials. The yield strength of the materials has been affected by the thermal weld cycles. As strength is related to hardness, it can be assumed that the ratio of strength between the two materials have been altered by the thermal weld cycles. The hardness and strength of base material B is higher than the hardness and strength of base material A, while the hardness, and presumably the strength, of the two HAZ are equal. When the yield strength ratios between the two materials were altered the percentage of stress the specimens were subjected to, were also altered. As a result of this the HAZ of material A was subjected to a

lower stress relative to the HAZ of material B because of the higher AYS of base material B than of base material A. The same observations and assumptions can be made for the HAZ of material A and material B in test 2. The actual effect of this cannot be assessed as the yield strength of the thermally weld simulated specimens is unknown. It is also reasonable to assume that there are some other metallurgical factors which may have affected the SSC resistance of the two materials.

### **5.3. Fracture morphology**

For the base materials it is difficult to assess the fracture morphology as crack-like attacks appears to be dominated by localized corrosion caused by CO<sub>2</sub> or H<sub>2</sub>S. The fine-grained microstructure of the two materials, with a high degree of disorder, also makes it difficult to determine whether the attacks are transgranular or intergranular.

Most of the observed cracks in both materials in the HAZ condition had propagated in a transgranular path. This is in consistence with what is expected for low alloy steels with yield strength less than 700 MPa, as for these steels.[11] Some of the cracks may have followed a mixed path which also takes place below this yield strength. It was observed that some of the cracks in the core section of the HAZ, outside the notches, often had initiated at the grain boundaries, while they seldom grew in an intergranular path. It has been difficult to assess the fracture morphology of the cracks as some corrosion also takes place during cracking of low alloy steels.

The reason for the initiation of cracks at grain boundaries in the HAZ may be twofold. It may be a result of the increased hardness along the grain boundaries, as brittle M-A constituents existed along them. However, it may also be a result of hydrogen diffusion to microstructural sites such as grain boundaries where the hydrogen becomes trapped and causes cracking.

### **5.4. Effect of various factors on SSC resistance**

The various factors which may have affected the SSC resistance of the materials are discussed in the following sections. Factors such as hardness, microstructure and the test environment have affected the SSC resistance. However, it can be difficult to separate and isolate the effect of each factor on the SSC resistance as several of them vary in the different cases studied.

#### **5.4.1. Hardness and strength**

According to the maximum hardness requirement for SSC resistance of 250 HV for materials exposed to sour environments, material A would be resistant to SSC, while material B might be somewhat susceptible as the hardness is more or less equal to the maximum hardness requirement. It is therefore assumed that the difference in hardness between the two base materials affects the SSC resistance. The corrosion attacks of the base materials are in consistence with this. However, in test 2, the materials experienced severe cracking, especially material B. The hardness may have had an effect on the relative susceptibility of the two materials. However, there are also other factors such as microstructural variations, strength and localized corrosion which may have affected the susceptibility as some cracks are observed in material A, in test 2.



The maximum acceptable hardness requirement for carbon and low alloy steels of 250 HV, according to ISO 15156-2, is also applicable to welds. The hardness of the thermally weld simulated regions in both materials does not reflect these requirements, as the focus when selecting thermal weld simulation parameters was on the achieved microstructure. The hardness of the thermally weld simulated region is well above the maximum hardness limit for SSC resistance. This has affected the susceptibility to SSC of the weld simulated materials. However, since no thermally weld simulated specimens without notches were tested, it is not possible to determine whether the severe cracking only is a result of the high hardness level or because of the increase in stress intensity at the notch. It would be beneficial to investigate thermally weld simulated specimens without a notch to isolate the effect of these two important factors. On the other hand, a weld without any defects is not considered a realistic case. As both base materials in the sour service test experienced such severe cracking, it reveals that a lower hardness of the HAZ probably would not have increased the SSC resistance of the HAZ significantly.

According to Y. Kobayashi *et. al*, researches have been concerned with whether the maximum hardness criteria of 250 HV applies to welded materials consisting of localized hard regions. The effect of M-A constituents on SSC resistance is not fully understood. According to the results of this project, it appears as SSC is more easily initiated at M-A constituents along the stressed side. [56]

The tensile strength of both steels is above 504 MPa, which in the theory is stated as a stress level in which SSC is rarely observed below. The higher strength level of material B than material A is in consistence with the hardness levels of the two materials. The strength levels affect the SSC resistance, indicating that material B is more susceptible to SSC than material A. The hardness and strength have similar effects on the SSC resistance.

Due to the maladjusted hardness of the HAZ region, relative to the maximum hardness requirements for SSC resistance in ISO 15156-2, it is recommended that further testing of HAZ regions of the materials is performed, with HAZ hardness within the requirements.

#### **5.4.2. Microstructure**

The hardness dependency of SSC susceptibility cannot explain all cracking of welded low alloy steels. Metallurgical factors, such as microstructure, also influence the SSC resistance. The microstructural features are closely related to the hardness level of the materials. In earlier studies, referred to in the theory, it has been found that acicular ferrite, which is the main microstructure constituent of base material B, possesses better SSC resistance than both bainite and ferrite/pearlite which are the main microstructural constituents of base material A. This may provide an explanation to why material A has experienced some cracking even though the hardness level indicated that the material is resistant to SSC. The severe cracking of base material B, on the other hand, does not confirm the results of other studies which indicated that acicular ferrite possesses a better resistance to SSC than bainite and ferrite/pearlite.

The microstructures of the two HAZ are seemingly equivalent, and it is therefore most likely that the two materials experience SSC resistance or susceptibility to the same extent. A possible reason why this is not observed was discussed in section 5.2.2. The effect of small M-A constituents in the HAZs on the SSC susceptibility is not well understood. In the specimens from test 1, it appears that a great part of the localized corrosion attacks have initiated at the prior austenite grain boundaries, where the M-A constituents exist. This is not as easily observed in test 2, as the corrosion attacks are larger than in test 1. The increased hardness of the M-A constituents may be a reason for initiation of cracks in these positions of the surface. On the other hand, the microstructural features of the M-A constituents may be more susceptible to SSC than the bainite matrix inside the prior austenite grains. The M-A constituents have a high hardness and there are residual stresses surrounding them.

It is difficult to assess the effect of the variations in the microstructures of the base materials versus the HAZ because the hardness levels are very different.

#### **5.4.3. Stress level**

The specimens were subjected to the same level of stress relative to the actual yield strength of the base materials. The stress level was kept the same for the base materials, while it was reduced for the HAZ from test 1 to test 2. The decrease in applied stress on the thermally weld simulated specimens in test 2 relative to test 1, did not compensate for the increased severity of the environment. The results of these tests only revealed that the materials cannot be subjected to that specific stress or higher stresses in an equivalently sour environment. It is therefore not possible to say whether the materials can withstand the same environment at lower stresses. Based on the severity of the attacks, especially in test 2, it is assumed that the stress level applied to the materials is far too high for this environment. For a wider understanding of the resistance of the materials to SSC it would be beneficial to investigate the SSC resistance of the two materials at lower stress levels. By testing at various stress levels, it would be possible to map the resistance and to determine the highest no-failure stress over 720 hours.

#### **5.4.4. Environmental parameters**

The effect of temperature cannot be assessed as both tests were carried out at the same temperature. The test temperature is expected to be the “worst case” temperature for low alloy steels, therefore testing may also be performed at temperatures expected in service, if those differs significantly from room temperature.

The results from the two tests are in consistence with the severity of the two environments based on the solution pH and the H<sub>2</sub>S partial pressure (pH<sub>2</sub>S). All specimens tested under the conditions of test 2 had experienced far more severe corrosion attacks and SSC compared to test 1. However, on the thermally weld simulated specimens in test 2, a layer of corrosion product was formed on the surface. According to theory, FeS scales may protect steels from SSC depending on the environmental parameters. The composition of the corrosion product was not investigated and it is therefore difficult to assess the effect of the layer in test 2.

#### **5.4.5. Other factors**

It would be beneficial to be able to study the effect of exposure time on SSC resistance. Knowledge about when the crack initiated and at what rate it grew would be beneficial as it may provide a better understanding of the mechanisms of SSC for the particular material, and it would provide a better overview of the test and the results. However, in this project, testing at 10 bars pressure in an autoclave; constant or regular monitoring would be difficult.

The two low alloy steels tested are produced by two different manufacturers. The manufacturing methods may have had an effect on the SSC resistance as the manufacturing method affects the microstructure and the hardness of the steels. Differences in main constituents and grain size between the two microstructures may be affected by the manufacturing method. However, according to theory and earlier research, the effect of grain size on SSC resistance is not completely understood and the effect may vary from one alloy to another which makes it reasonable to assume that this is related to differences from the manufacturing processes.



## 6. Conclusions

The resistance to SSC of two modified F60 low-alloy steels, named material A and material B, was tested and evaluated. The materials were tested in the base material condition and in the intercritically reheated CGHAZ, obtained by thermal weld simulations. Based on the two corrosion tests performed, it was found that:

- In the sweet-transition region, the corrosion attacks of the base materials were mostly characterized as general and localized corrosion caused by CO<sub>2</sub> and/or H<sub>2</sub>S.
- Based on the depth of the corrosion attacks, some SSC may have taken place at the same time as the localized corrosion, therefore modifications or precautions should be taken before the materials are applied to H<sub>2</sub>S-containing environment.
- Material A was less severely attacked by SSC and general or localized corrosion caused by CO<sub>2</sub> and H<sub>2</sub>S than material B.
- The higher susceptibility to SSC and corrosion caused by H<sub>2</sub>S and CO<sub>2</sub> of material B relative to material A is assumed to be a result of the variations in microstructure constituents in the two materials and with that the higher hardness of material B than material A, as hardness and microstructure are two important factors in SSC resistance of steels.
- The intercritically reheated CGHAZ, produced in this work, is considered unsuitable for environments in the sweet-transition region. The high susceptibility of the HAZ in the mild environment is assumed to be a result of the high hardness of the HAZ and the increased stress intensity caused by the notch.
- In congruence with the severity of the two test environments, the SSC and corrosion attacks of both materials were deeper and more severe in the sour-service test than in the sweet-transition test.
- Because of the general and localized corrosion caused by CO<sub>2</sub> and/or H<sub>2</sub>S, it was difficult to determine the fracture morphology of the SSC. However, the SSC mostly appeared as transgranular. In the HAZ, the localized corrosion attacks and cracks often initiated at the prior austenite grain boundaries near the M-A constituents.
- Both materials are considered unsuitable for sour-service applications.
- Based on the severity of the corrosion attacks and cracking of the materials, it is recommended that the materials are further tested and reviewed before applied to “sour service” application or only applied to environments free of H<sub>2</sub>S.



## 7. References

1. Kane, R.D. and M.S. Cayard, *Roles of H<sub>2</sub>S in the Behavior of Engineering Alloys: A Review of Literature and Experience*. CORROSION 98, 1998.
2. Omweg, G., et al., *Effect of Welding Parameters and H<sub>2</sub>S Partial Pressure on the Susceptibility of Welded HSLA Steels to Sulfide Stress Cracking*. Welding journal, 2003. **82**(6): p. 136.
3. EFC, *Guidelines on Materials Requirements for Carbon and Low Alloy Steels for H<sub>2</sub>S-containing Environments in Oil and Gas Production* 2009: The European Federation of Corrosion.
4. Asahi, H., et al., *Effects of Mn, P, and Mo on sulfide stress cracking resistance of high strength low alloy steels*. Metallurgical and Materials Transactions A, 1988. **19**(9): p. 2171-2177.
5. Zhao, M.-C., et al., *Role of microstructure on sulfide stress cracking of oil and gas pipeline steels*. Metallurgical and Materials Transactions A, 2003. **34**(5): p. 1089-1096.
6. Turconi, G.L., et al., *Improvement of resistance to SSC Initiation and propagation of high strength OCTG through microstructure and precipitation control*. CORROSION 2001, 2001.
7. ISO, *15156-2: Petroleum and natural gas industries—Materials for use in H<sub>2</sub>S-containing environments in oil and gas production—Part 2: Cracking-resistant carbon and low alloy steels and the use of cast irons*, 2009.
8. Huang, H. and W. Shaw, *Cold work effects on sulfide stress cracking of pipeline steel exposed to sour environments*. Corrosion science, 1993. **34**(1): p. 61-78.
9. Beidokhti, B., A. Dolati, and A. Koukabi, *Effects of alloying elements and microstructure on the susceptibility of the welded HSLA steel to hydrogen-induced cracking and sulfide stress cracking*. Materials Science and Engineering: A, 2009. **507**(1): p. 167-173.
10. Radkevych, O. and V. Pokhmurs'kyi, *Influence of hydrogen sulfide on serviceability of materials of gas field equipment*. Materials Science, 2001. **37**(2): p. 319-332.
11. Kane, R., *Roles of H<sub>2</sub>S in behaviour of engineering alloys*. International Metals Reviews, 1985. **30**(1): p. 291-301.
12. M.R. Louthan, J., *Role of Hydrogen in Stress Corrosion Cracking*, in *Stress Corrosion Cracking*, A.A. J. Yahalom, Editor 1980, Freund. p. 39 - 55.
13. Scully, J.C., *Stress Corrosion Cracking: Introductory remarks in Nato Science Committee Research Evaluation Conference*1971: Portugal.
14. Pourbaix, M., *Electrochemical Aspects of Stress Corrosion Cracking in Nato Science Committee Research Evaluation Conference*1971: Portugal.
15. Swann, P.R., *Morphological Aspects of Stress Corrosion Failure*, in *Nato Science Committee Research Evaluation Conference*1971: Portugal.
16. Ifezue, D. and F. Tobins, *Failure Investigation of a Gate Valve Eye Bolt Fracture During Hydrotesting*. Journal of Failure Analysis and Prevention, 2013: p. 1-8.
17. Onsøien, M.I., *Spenningskorrosjon av sveist stål i H<sub>2</sub>S-miljø*, 1986, SINTEF. p. 1-26.
18. Mendibide, C. and T. Sourmail, *Composition optimization of high-strength steels for sulfide stress cracking resistance improvement*. Corrosion science, 2009. **51**(12): p. 2878-2884.
19. ISO, *21457: Petroleum, Petrochemical and Natural Gas Industries - Materials Selection and Corrosion Control for Oil and Gas Production Systems* 2010, ISO.

20. Adams, M. and J.L. Gossett, *Sulfide Stress Cracking and the Commercial Application of NACE MR0175-84*, 1999, Technical Monograph 34, Fisher.
21. Rhodes, P., L. Skogsberg, and R. Tuttle, *Pushing the limits of metals in corrosive oil and gas well environments*. Corrosion, 2007. **63**(1): p. 63-100.
22. NACE, *TM0177: Laboratory Testing of Metals for Resistance to Sulfide Stress Cracking and Stress Corrosion Cracking in H<sub>2</sub>S Environments*, 2005, NACE International.
23. Gojić, M., L. Kosec, and L. Vehovar, *The susceptibility to sulphide stress cracking of low alloy steels*. Materials and Corrosion, 1998. **49**(1): p. 27-33.
24. Smith, S.N. and M.W. Joosten, *Corrosion of carbon steel by H<sub>2</sub>S in CO<sub>2</sub> containing oilfield environments*. CORROSION 2006, 2006.
25. Ren, C., et al., *Corrosion behavior of oil tube steel in simulant solution with hydrogen sulfide and carbon dioxide*. Materials chemistry and physics, 2005. **93**(2): p. 305-309.
26. Kobayashi, K., et al., *Effect of Testing Temperature on SSC Properties of Low Alloy Steel*. CORROSION 2006, 2006.
27. Asahi, H., et al., *Metallurgical factors controlling SSC resistance of high-strength, low-alloy steels*. Corrosion, 1989. **45**(6): p. 519-527.
28. Haq, A.J., et al., *Effect of microstructure and composition on hydrogen permeation in X70 pipeline steels*. International Journal of Hydrogen Energy, 2013. **38**(5): p. 2544-2556.
29. Albarran, J., H. Lopez, and L. Martinez, *Crack growth in a welded microalloyed steel under sulfide stress cracking conditions*. Journal of materials engineering and performance, 1998. **7**(6): p. 777-783.
30. Yurioka, N. and H. Suzuki, *Hydrogen assisted cracking in C-Mn and low alloy steel weldments*. Int. Mater. Rev., 1990. **35**(1): p. 217-249.
31. Edmonds, D. and R. Cochrane, *Structure-property relationships in bainitic steels*. Metallurgical and Materials Transactions A, 1990. **21**(6): p. 1527-1540.
32. H.K.D.H. Bhadeshia, R.W.K.H., *The embrittlement and fracture of steels in Steels microstructure and properties* 2006, Elsevier Ltd. . p. 235-258.
33. Lee, S., B.C. Kim, and D. Kwon, *Correlation of microstructure and fracture properties in weld heat-affected zones of thermomechanically controlled processed steels*. Metallurgical Transactions A, 1992. **23**(10): p. 2803-2816.
34. Akselsen, O.M., *Transformation Behaviour*, 2012, NTNU. p. 15.1-15.19.
35. H.K.D.H. Bhadeshia, R.W.K.H., *Weld microstructures*, in *Steels Microstructure and Properties* 2006, Elsevier Ltd. p. 287-306.
36. Moeinifar, S., A. Kokabi, and H. Madaah Hosseini, *Influence of peak temperature during simulation and real thermal cycles on microstructure and fracture properties of the reheated zones*. Materials & Design, 2010. **31**(6): p. 2948-2955.
37. Shi, Y. and Z. Han, *Effect of weld thermal cycle on microstructure and fracture toughness of simulated heat-affected zone for a 800MPa grade high strength low alloy steel*. Journal of Materials Processing Technology, 2008. **207**(1): p. 30-39.
38. King, J., *Cleavage initiation in the intercritically reheated coarse-grained heat-affected zone: Part I. Fractographic evidence*. Metallurgical and Materials Transactions A, 1994. **25**(3): p. 563-573.
39. Davis, C. and J. King, *Effect of cooling rate on intercritically reheated microstructure and toughness in high strength low alloy steel*. Materials science and technology, 1993. **9**(1): p. 8-15.
40. Anderson, T.L., *Application to Structures*, in *Fracture Mechanics Fundamentals and Applications* 2005. p. 423-428.



41. ASTM, *ASTM A694/A694M-08 Standard Specifications for Carbon and Alloy Steel Forgings for Pipe Flanges, Fittings, Valves, and Parts for High-Pressure Transmission Service* 2008.
42. Balcar, M., et al., *HEAT TREATMENT AND MECHANICAL PROPERTIES OF HEAVY FORGINGS FROM A694–F60 STEEL*. *Materiali in tehnologije*, 2011. **45**(6): p. 619-622.
43. *Various E-mails and conversations with GE Oil & Gas*, Fall 2012.
44. Rossoll, A., C. Berdin, and C. Prioul, *Determination of the fracture toughness of a low alloy steel by the instrumented Charpy impact test*. *International Journal of Fracture*, 2002. **115**(3): p. 205-226.
45. Haušild, P., et al., *The influence of ductile tearing on fracture energy in the ductile-to-brittle transition temperature range*. *Materials Science and Engineering: A*, 2002. **335**(1): p. 164-174.
46. ASTM, *E8: Standard Test Methods for Tension Testing of Metallic Materials*, 2000, ASTM International. p. 1-28.
47. ISO, *Metallic materials–Tensile testing-Part 1: Method of test at room temperature*, 2009. p. 1-72.
48. Lan, L., et al., *Analysis of microstructural variation and mechanical behaviors in submerged arc welded joint of high strength low carbon bainitic steel*. *Materials Science and Engineering: A*, 2012.
49. Sedriks, A.J., *Making and Using Bent-Beam Specimens*, in *Stress Corrosion Cracking Test Methods* 1990, National Association of Corrosion Engineers p. 19-23.
50. Parkins, R.N., *Stress Corrosion Test Methods*, in *Nato Science Committee Research Evaluation Conference* 1971: Portugal.
51. Sedriks, A.J., *Stress corrosion cracking test methods* 1990: National Association of Corrosion Engineers.
52. ASTM, *G39: Standard Practice for Preparation and Use of Bent-Beam Stress-Corrosion Test Specimens*, 2011, ASTM International. p. 1-8.
53. Aylward, G.H. and T.J.V. Findlay, *SI chemical data*. 5 ed 1971: Wiley New York. 42-43.
54. ISO, *6507-1 Metallic materials-Vickers hardness test - Part 1: Test method*, 2005.
55. Hall, E.O., *Yield Point Phenomena in Metals and Alloys* 1970, London: Macmillian and Co Ltd.
56. Kobayashi, Y., et al., *The resistance of welded linepipes to sulfide stress cracking*. *Corrosion science*, 1987. **27**(10): p. 1117-1135.



## Appendix A: Achieved Strains Recorded by Extensometer

Documentation of achieved strains for all the separate cases tested in both test 1 and test 2 are presented in Table A-1 and Table A-2 respectively.

Table A-1: Achieved strains for the four cases tested in test 1.

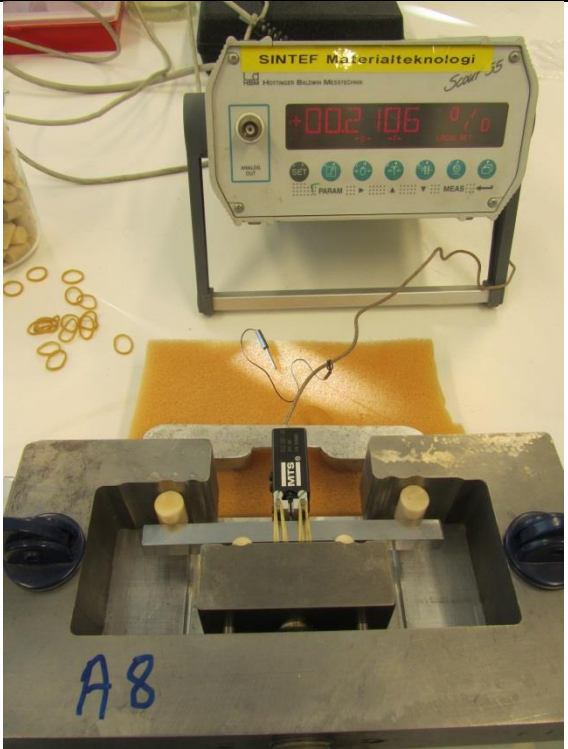

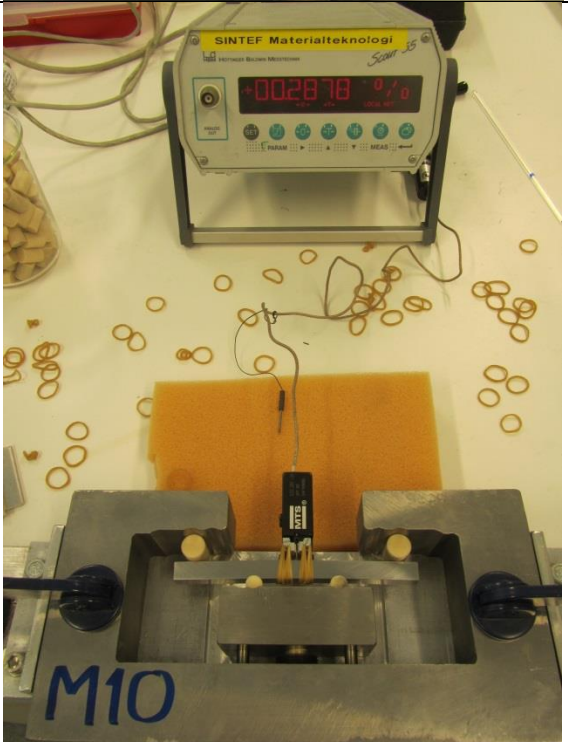
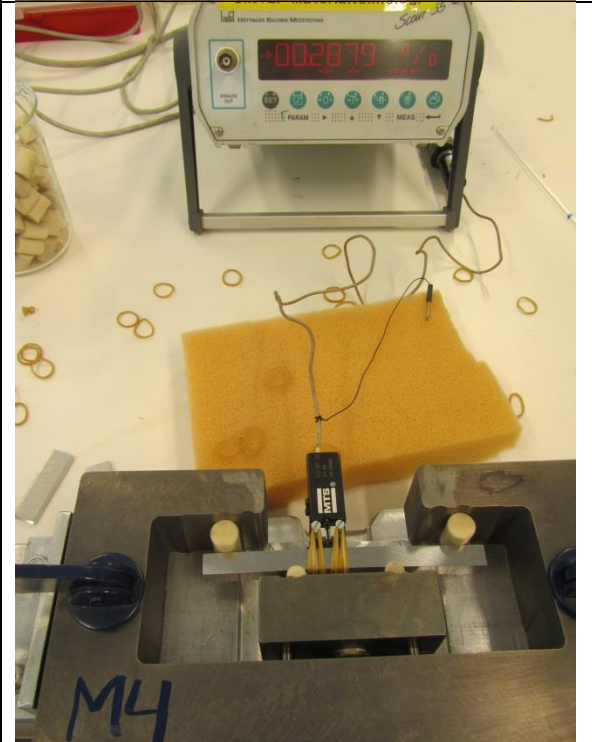
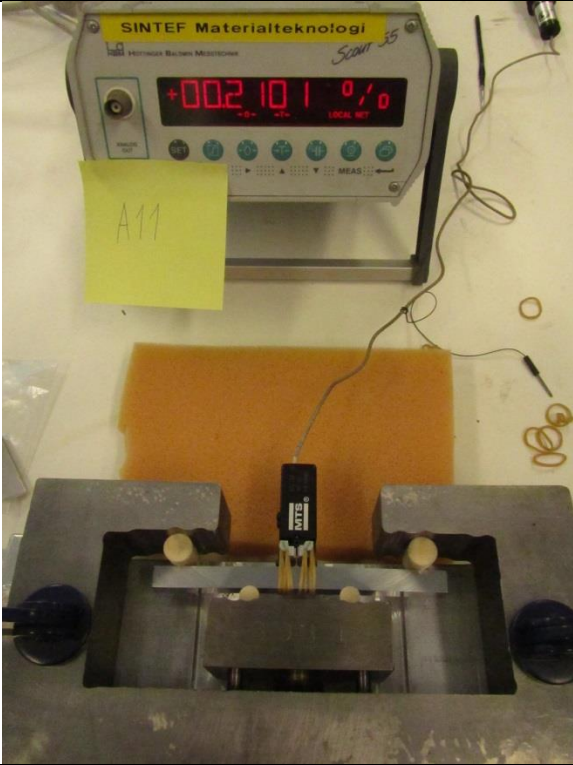



|   | Base material  | Thermal weld simulated   |
|---|--|--|
| A |  <p>A photograph showing a SINTEF Materialteknologi extensometer (Scan 35) displaying a strain of +002.106%. The device is connected to a specimen held in a metal fixture labeled 'A8'. The specimen is a yellowish material with a central weld line. The extensometer is mounted on a stand, and the specimen is held in a metal fixture with blue handles. The background shows a white surface with some small yellowish particles.</p>   |  <p>A photograph showing a SINTEF Materialteknologi extensometer (Scan 35) displaying a strain of +002.105%. The device is connected to a specimen held in a metal fixture labeled 'A2'. The specimen is a yellowish material with a central weld line. The extensometer is mounted on a stand, and the specimen is held in a metal fixture with blue handles. The background shows a white surface with some small yellowish particles.</p>  |
| B |  <p>A photograph showing a SINTEF Materialteknologi extensometer (Scan 35) displaying a strain of +002.878%. The device is connected to a specimen held in a metal fixture labeled 'M10'. The specimen is a yellowish material with a central weld line. The extensometer is mounted on a stand, and the specimen is held in a metal fixture with blue handles. The background shows a white surface with some small yellowish particles.</p> |  <p>A photograph showing a SINTEF Materialteknologi extensometer (Scan 35) displaying a strain of +002.879%. The device is connected to a specimen held in a metal fixture labeled 'M4'. The specimen is a yellowish material with a central weld line. The extensometer is mounted on a stand, and the specimen is held in a metal fixture with blue handles. The background shows a white surface with some small yellowish particles.</p> |

Table A-2: Achieved strains for the four cases tested in test 2.

|          | Base material   | Thermal weld simulated   |
|----------|---|--|
| <b>A</b> |   |   |
| <b>B</b> |  |  |

**YARAPRAXAIR**

# Sertifikat

Side 1 av 1

|  |  |   |   |
|--|--|---|---|
| <b>Kunde:</b><br>SINTEF Materialer og Kjemi    | <b>Sertifikat nr.:</b><br>82637417-01-K-138978HG | <b>Flaske vannvolum (l):</b><br>10                  | <b>Flaskenummer:</b><br>K-138978HG            |
| <b>Kunde referanse:</b><br>551579 A-K Kvernbrå | <b>Kvalitetsklasse:</b><br>2                     | <b>Anbefalt trykkregulator:</b><br>Ultraserien (SS) | <b>Flaskeventilgjenger:</b><br>DIN 477 No. 10 |
|  |  |   | <b>Fylletrykk v/20°C (bar g):</b><br>33.3     |

| Komponenter | Bestilt sammensetning<br>mol % | Sertifisert sammensetning<br>mol % | Usikkerhet<br>% relativ |
|-------------|--------------------------------|------------------------------------|-------------------------|
| H2S<br>CO2  | 1<br>Rest                      | 1.00<br>Rest                       | 2                       |

|   |  |   |   |  |
|---|--|---|---|--|
| <b>100 % LEL i luft (vol %):</b>  | <b>Konfidens intervall:</b><br>95 % (k=2)      | <b>Sporbarhet klasse 1:</b><br>SI-enhet for masse   | <b>Kondensasjonstemp.</b><br>ved fylletrykk (°C)<br>0 | <b>Stabilitetstid (måneder):</b><br>12 |
| <b>Laveste anbefalte brukstrykk (bar g):</b><br>3,3   | <b>Anbefalt lager og brukstemp. (°C)</b><br>20 | <b>Spesielle opplysninger:</b>  |   |  |
| <b>For HMS datablad, se vår hjemmeside <a href="http://www.yarapraxair.com">www.yarapraxair.com</a></b> |  | <b>Ved mistanke om utkondensering må flasken lagres horisontalt ved romtemperatur i 14 dager, eller rulles horisontalt i 8 timer ved &gt; 60 omdreininger/min før bruk.</b> |   |  |

Rjukan <sup>6/3-2013</sup> Tor Mørten Hammer  
(Produksjonssted) (Dato) (Ansvarlig)

Yara Praxair AS Fnr./Reg.No. 945 772 042

Postadr.  
P.O.Box 23, Haugenstua  
N-0915 OSLOTelefon  
+47 04 27 7Telefax:  
+47 24 15 64 29



|   |  |  |  |   |
|---|--|--|--|---|
| <b>Kunde:</b><br>Sintef Materialer og Kjemi     | <b>Sertifikat nr.:</b><br>82664535-01-K-597293 | <b>Flaske vannvolum (l):</b><br>10                 | <b>Flaskenummer:</b><br>K-597293             |   |
| <b>Kunde referanse:</b><br>551579 A-K. Kvernbrå | <b>Kvalitetsklasse:</b><br>2                   | <b>Anbefalt trykregulator:</b><br>Ultraserien (SS) | <b>Flaskeventilgjenger:</b><br>DIN 477 No. 6 | <b>Fylletrykk v/20°C (bar g):</b><br>28,5 |

| Komponenter | Bestilt sammensetning<br>mol % | Sertifisert sammensetning<br>mol % | Uslkkerhet<br>% relativ |
|-------------|--------------------------------|------------------------------------|-------------------------|
| H2S<br>CO2  | 10<br>Rest                     | 10,0<br>Rest                       | 2                       |

|   |  |   |  |  |
|---|--|---|--|--|
| <b>100 % LEL i luft (vol %):</b>  | <b>Konfidens intervall:</b><br>95 % (k=2)          | <b>Sporbarhet klasse 1:</b><br>SI-enhet for masse   | <b>Kondensasjonstemp.<br/>ved fylletrykk (°C)</b><br>0 | <b>Stabilitetstid (måneder):</b><br>12 |
| <b>Laveste anbefalte<br/>brukstrykk (bar g):</b><br>2,9   | <b>Anbefalt lager og<br/>brukstemp. (°C)</b><br>20 | <b>Spesielle opplysninger:</b>  |  |  |
| <b>For HMS datablad,<br/>se vår hjemmeside <a href="http://www.yarapraxair.com">www.yarapraxair.com</a></b> |  | <b>Ved mistanke om utkondensering må flasken lagres horisontalt<br/>ved romtemperatur i 14 dager, eller rulles horisontalt<br/>i 8 timer ved &gt; 60 omdreininger/min før bruk.</b> |  |  |

Rjukan  
(Produksjonssted)25/4-2013  
(Dato)Tor Arviden Hamme  
(Ansvarlig)

Yara Praxair AS Fnr./Reg.No. 945 772 042

Postadr.  
P.O.Box 23, Haugenstua  
N-0915 OSLOTelefon  
+47 04 27 7Telefax:  
+47 24 15 64 29



|  |  |   |  |
|--|--|---|--|
| <b>Kunde:</b><br>SINTEF Materialer og Kjemi    | <b>Sertifikat nr.:</b><br>82837417-02-K-641284 | <b>Flaske vannvolum (l):</b><br>10                  | <b>Flaskenummer:</b><br>K-541264             |
| <b>Kunde referanse:</b><br>551579 A-K Kvernbrå | <b>Kvalitetsklasse:</b><br>2                   | <b>Anbefalt trykkregulator:</b><br>Ultraserien (SS) | <b>Flaskeventilgjenger:</b><br>DIN 477 No. 6 |
|  |  |   | <b>Fylletrykk v/20°C (bar g):</b><br>28.5    |

| Komponenter | Bestilt sammensetning<br>mol % | Sertifisert sammensetning<br>mol % | Usikkerhet<br>% relativ |
|-------------|--------------------------------|------------------------------------|-------------------------|
| H2S<br>CO2  | 10<br>Rest                     | 9.97<br>Rest                       | 2                       |

|   |  |   |  |  |
|---|--|---|--|--|
| <b>100 % LEL i luft (vol %):</b>  | <b>Konfidens Intervall:</b><br>95 % (k=2)          | <b>Sporbarhet klasse 1:</b><br>SI-enhet for masse   | <b>Kondensasjonstemp.<br/>ved fylletrykk (°C)</b><br>0 | <b>Stabilitetstid (måneder):</b><br>12 |
| <b>Laveste anbefalte<br/>brukstrykk (bar g):</b><br>2.9   | <b>Anbefalt lager og<br/>brukstemp. (°C)</b><br>20 | <b>Spesielle opplysninger:</b>  |  |  |
| <b>For HMS datablad,<br/>se vår hjemmeside <a href="http://www.yarapraxair.com">www.yarapraxair.com</a></b> |  | <b>Ved mistanke om utkondensering må flasken lagres horisontalt<br/>ved romtemperatur i 14 dager, eller rulles horisontalt<br/>i 8 timer ved &gt; 60 omdreininger/min før bruk.</b> |  |  |

Rjukan 7/3-2013 Tor Morten Hammel  
(Produksjonssted) (Dato) (Ansvarlig)

Yara Praxair AS Fnr./Reg.No. 945 772 042

Postadr.  
P.O.Box 23, Haugenstua  
N-0915 OSLO

Telefon  
+47 04 27 7

Telefax:  
+47 24 15 64 29

### Appendix C: pH Calibration Curve for SSC Test 2.

A graphical plot of the pH versus volume of HCl is presented in Figure C-1. The curve was obtained by adding small portions of HCl (10 %) by a pipette to a predetermined volume of electrolyte from the test autoclave in test 2. Totally 0.18 ml HCl was added to 40 ml of electrolyte. The curve was applied to pH adjustments of test 2.

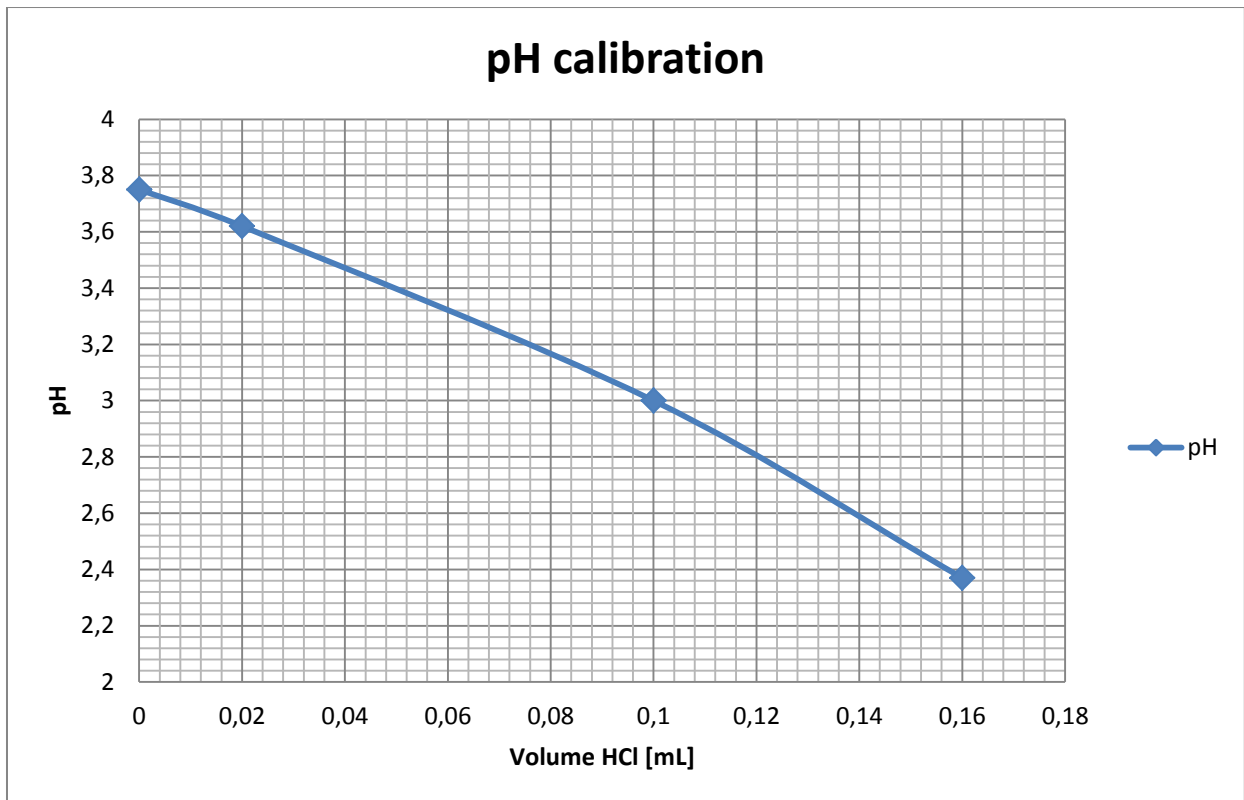


Figure C-1: pH versus volume of HCl added, for calibration of pH adjustments of test 2.



## Appendix D: Stress-Strain Curves from Tensile Testing

The stress-strain curves of all three parallels of both material A and material B are presented in the figures below. Stress-strain curves for material A are presented in Figure D-1 through Figure D-3, while stress-strain curves for material B are presented in Figure D-4 through Figure D-6.

### Material A

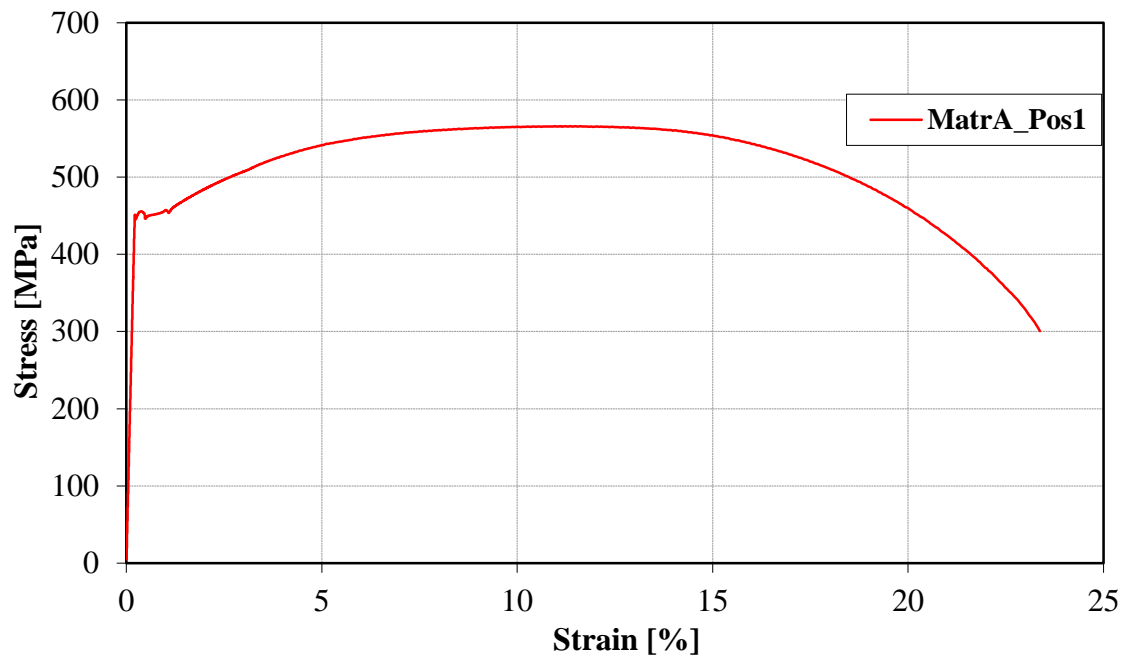


Figure D-1: Stress-strain curve for material A, parallel 1.

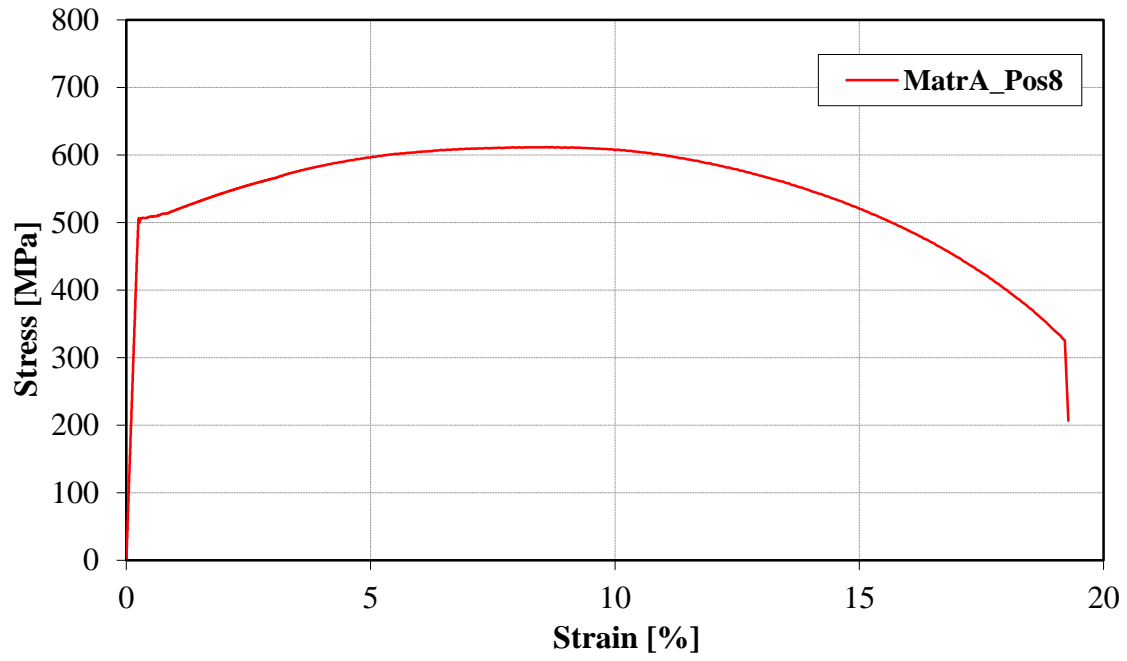


Figure D-2: Stress-strain curve for material A, parallel 2.

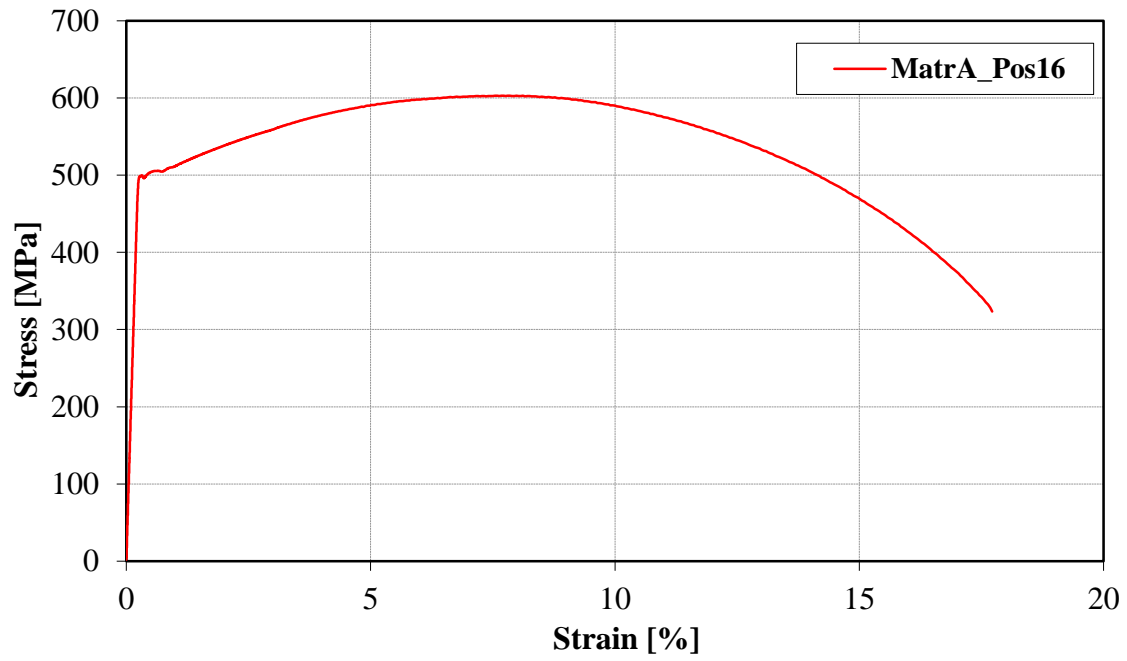


Figure D-3: Stress-strain curve for material A, parallel 3.

## Material B

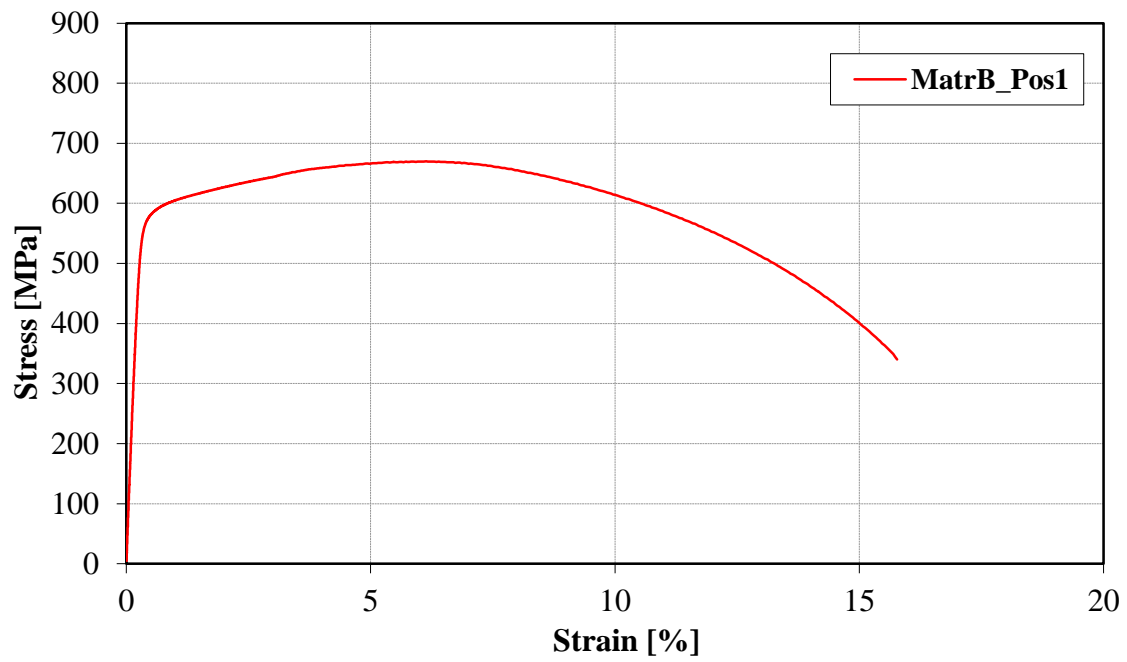


Figure D-4: Stress-strain curve for material B, parallel 1.

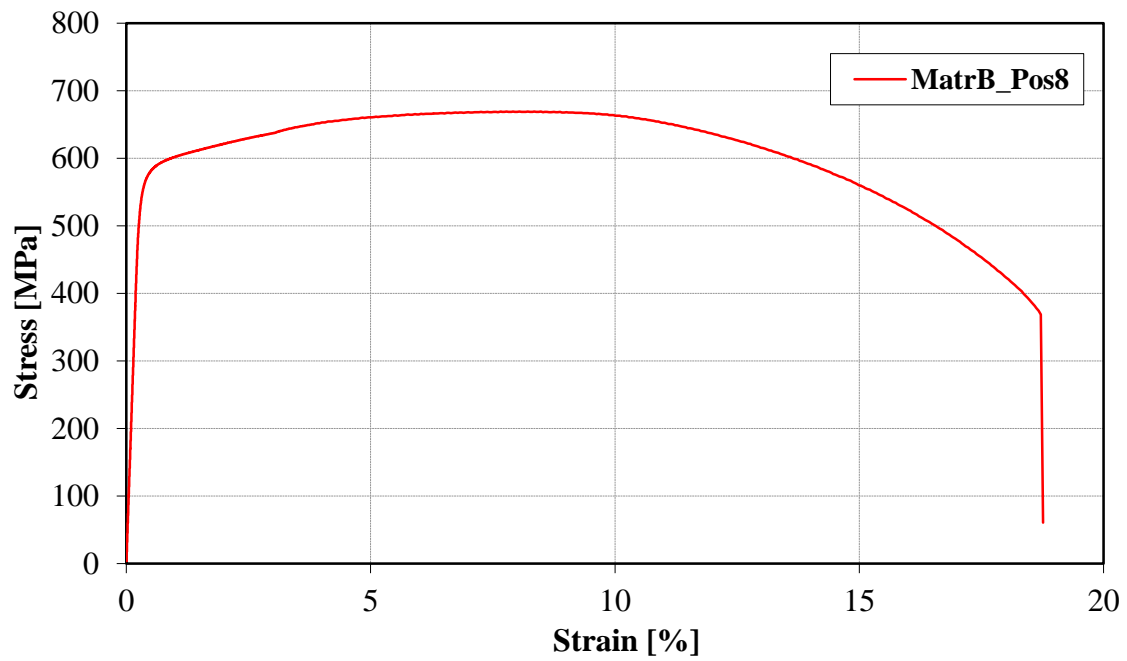


Figure D-5: Stress-strain curve for material B, parallel 2.

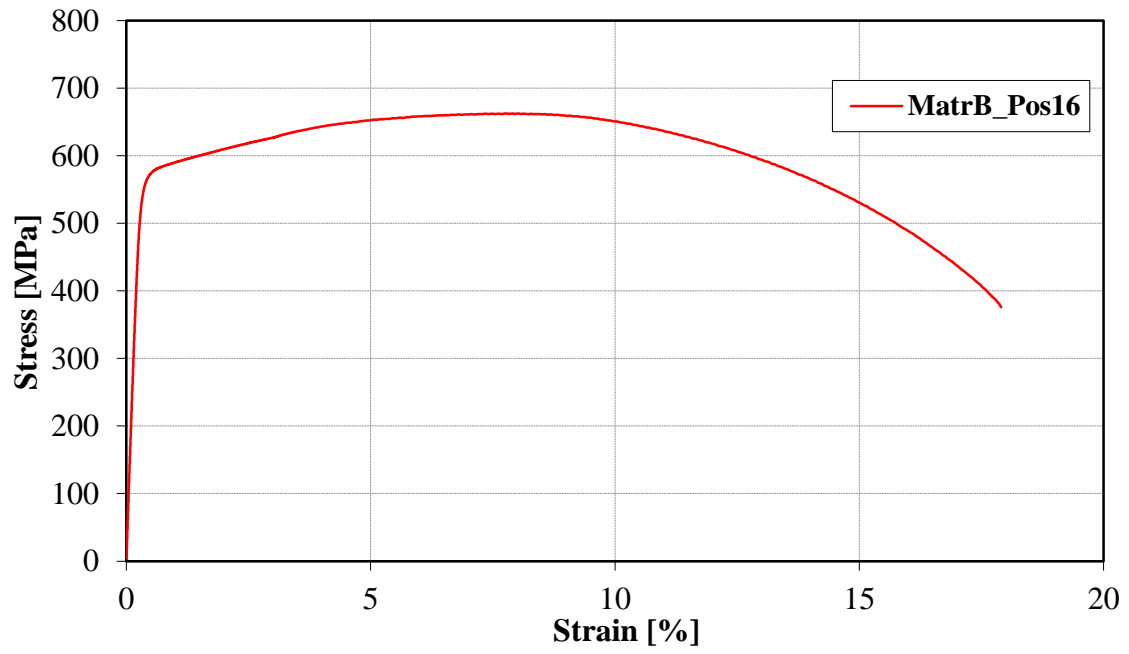


Figure D-6: Stress-strain curve for material B, parallel 3.

## Appendix E: Results from Vickers Hardness Measurements

Results from all the parallel Vickers hardness measurements and the average of the parallels, of material A are presented in Table E-1.

Table E-1: All values of Vickers hardness measurements of the heat affected zone of material A.

| Position | Parallel 1 [HV] | Parallel 2 [HV] | Parallel 3 [HV] | Average [HV] |
|----------|-----------------|-----------------|-----------------|--------------|
| -12      | 230.4           | -               | 245.6           | 238.0        |
| -11      | 245.5           | 253.6           | 215.3           | 238.1        |
| -10      | 276.3           | 236.6           | 242.3           | 251.7        |
| -9       | 243.3           | 252.7           | 235.3           | 243.8        |
| -8       | 146.7           | 259.3           | 262.6           | 256.2        |
| -7       | 257.1           | 294.6           | 271.6           | 274.4        |
| -6       | 316.0           | 307.0           | 282.7           | 301.9        |
| -5       | 325.4           | 304.7           | 316.7           | 315.6        |
| -4       | 256.6           | 310.5           | 351.1           | 339.4        |
| -3       | 330.5           | 311.6           | 337.9           | 326.7        |
| -2       | 319.5           | 362.2           | 310.2           | 330.6        |
| -1       | 322.7           | 323.5           | 369.1           | 338.4        |
| 0        | 419.0           | 359.5           | 347.9           | 375.5        |
| 1        | 422.7           | 396.9           | 375.4           | 398.3        |
| 2        | 399.2           | 346.4           | 316.3           | 354.1        |
| 3        | 320.6           | 364.5           | 315.8           | 333.6        |
| 4        | 299.3           | 347.9           | -               | 323.6        |
| 5        | 280.7           | 321.0           | 327.7           | 309.8        |
| 6        | 263.7           | 308.6           | 299.3           | 290.5        |
| 7        | 244.8           | 250.9           | 310.0           | 268.6        |
| 8        | 239.4           | 296.0           | 281.8           | 272.4        |
| 9        | 253.2           | 296.6           | 308.7           | 286.2        |
| 10       | 244.3           | 248.4           | 265.4           | 252.7        |
| 11       | 235.3           | 263.7           | 267.9           | 255.6        |
| 12       | 233.2           | 234.2           | 248.1           | 241.5        |
| 13       | 217.8           | 242.8           | 244.0           | 234.9        |
| 14       | 208.9           | 242.8           | 250.2           | 234.0        |

Results from all the parallel Vickers hardness measurements and the average of the parallels, of material B are presented in Table E-2.

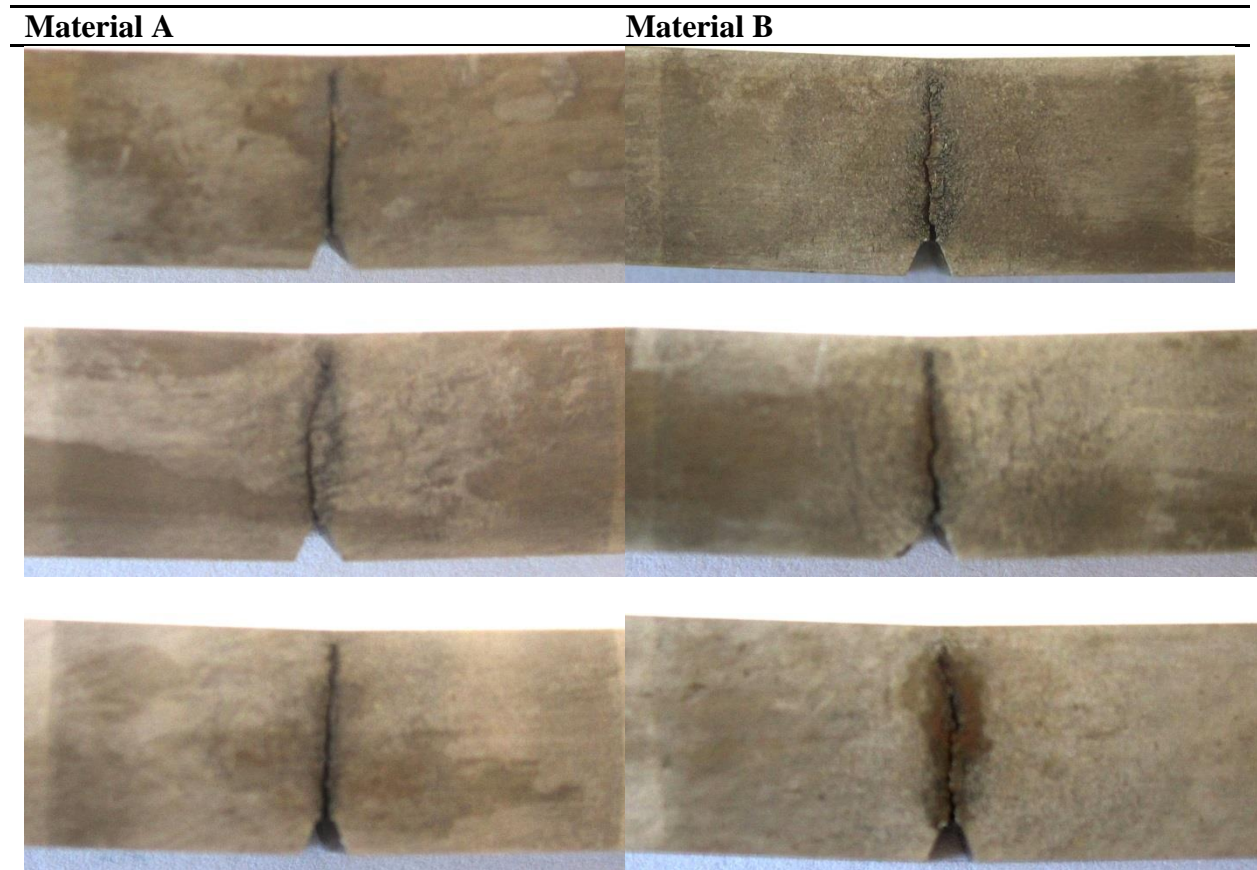
**Table E-2: All values of Vickers hardness measurements for the heat affected zone of material B.**

| <b>Position</b> | <b>Parallel 1 [HV]</b> | <b>Parallel 2 [HV]</b> | <b>Parallel 3 [HV]</b> | <b>Average [HV]</b> |
|-----------------|------------------------|------------------------|------------------------|---------------------|
| -12             | 265.7                  | 242.1                  | 241.1                  | 249.6               |
| -11             | 240.9                  | 232.4                  | 229.6                  | 234.3               |
| -10             | 261.4                  | 247.4                  | 231.8                  | 246.9               |
| -9              | 272.5                  | 246.1                  | 231.9                  | 250.2               |
| -8              | 270.6                  | 252.7                  | 244.6                  | 256.0               |
| -7              | 289.4                  | 266.4                  | 257.2                  | 271.0               |
| -6              | 338.5                  | 274.8                  | 278.8                  | 297.4               |
| -5              | 243.1                  | 297.1                  | 290.8                  | 277.0               |
| -4              | 344.3                  | 304.3                  | 308.9                  | 319.2               |
| -3              | 389.7                  | 314.5                  | 335.5                  | 346.6               |
| -2              | 360.2                  | 369.1                  | 325.2                  | 351.5               |
| -1              | 446.5                  | 383.5                  | 320.8                  | 383.6               |
| 0               | 327.3                  | 328.3                  | 322.3                  | 326.0               |
| 1               | 403.4                  | 328.7                  | 359.7                  | 363.9               |
| 2               | 368.6                  | 329.3                  | 334.1                  | 344.0               |
| 3               | 414.8                  | 330.9                  | 308.4                  | 351.4               |
| 4               | 383.0                  | 294.3                  | 291.5                  | 322.9               |
| 5               | 304.5                  | 272.7                  | 309.3                  | 295.5               |
| 6               | 315.2                  | 265.7                  | 299.3                  | 293.4               |
| 7               | 314.1                  | 260.0                  | 252.0                  | 275.4               |
| 8               | 272.7                  | 361.5                  | 241.9                  | 292.0               |
| 9               | 278.4                  | 246.4                  | 240.7                  | 255.2               |
| 10              | 287.6                  | 250.5                  | 250.5                  | 262.9               |
| 11              | 280.8                  | 274.8                  | 279.3                  | 278.3               |
| 12              | 279.5                  | 266.4                  | 276.7                  | 274.2               |
| 13              | 273.6                  | 268.6                  | 245.9                  | 262.7               |
| 14              | 263.6                  | -                      | 240.0                  | 251.8               |

## Appendix F: Macro Photos of Cracked Specimens.

Photos of all specimens where cracks were observed on a macro level are presented in Table F-1. Cracks were only observed on a macro level in HAZ specimens.

Table F-1: Macro photos of cracked HAZ specimens from test 1.



In test 2, cracks were observed in both the base material specimens and the HAZ specimens. Macro photos of all the base material specimens and HAZ specimens from test 2 are presented in Table F-2 and Table F-3 respectively.

**Table F-2: Macro photos of cracked base material specimens from test 2.**







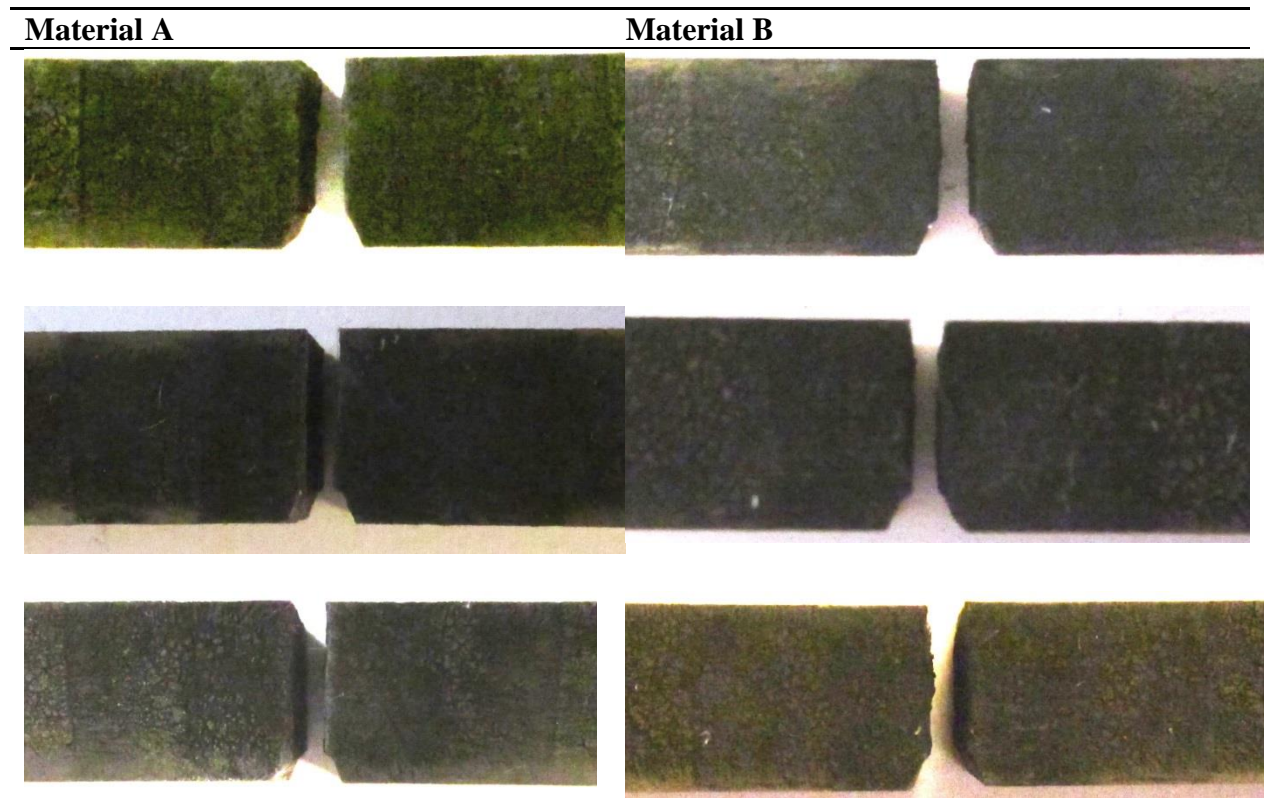
| <b>Material A</b>   | <b>Material B</b>   |
|---|---|
|    |   |
|    |   |
|  |  |



Table F-3: Macro photos of cracked HAZ specimens from test 2.



## **Appendix G: Micrographs of All SSC Specimens, Test 1 and 2**

Micrographs of all specimens from both test 1 and test 2 are presented at the magnifications of either 100X or 300X. The first three tables consist of micrographs from test 1. In Table G-1, micrographs of cracking observed in the core section of the base materials are presented at 100X magnification. This magnification is selected to provide better overview of the stressed surface of the specimens. In Table G-2, micrographs of the core section of the equivalent specimens are presented at 300X magnification. This is to provide more detailed micrographs of the corrosion attacks. In Table G-3, micrographs of cracks observed in the core section of the heat affected zone of the specimens of both material A and material B are presented at 300X. These micrographs are only presented at this magnification as the 100X micrographs did not provide any additional information.

In Table G-4, micrographs of all base material specimens from test 2 are presented at 100X magnification. There are no HAZ specimen micrographs in this appendix as only one specimen of each material was investigated; those micrographs are presented in the report. The micrographs of test 2 are only presented at one magnification because the attacks were so severe that a larger magnification is not suitable.

Table G-1: Micrographs of all FPB specimens of base material and B in test 1.

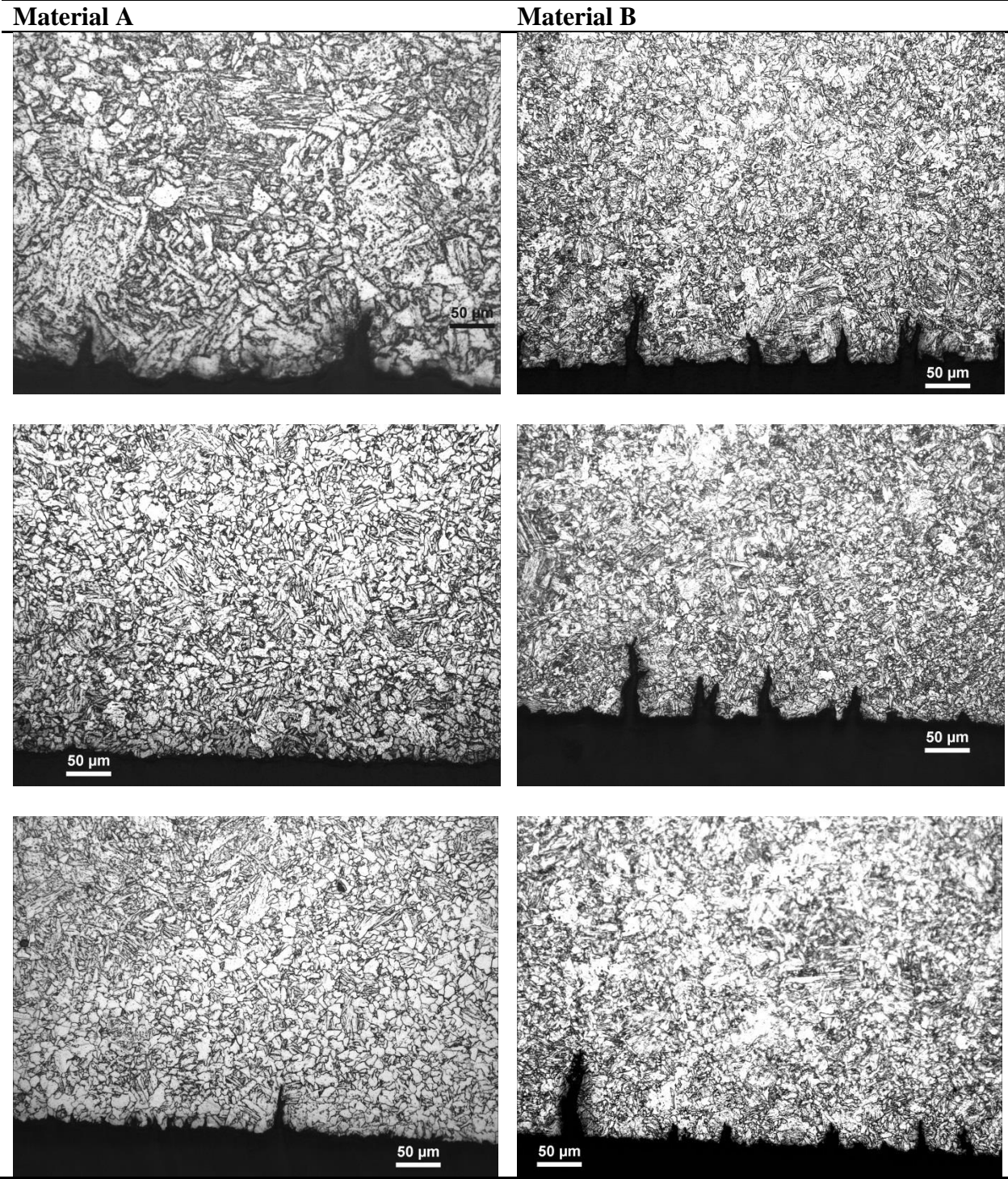


Table G-2: Micrographs of all FPB specimens of base material A and B in test 1.

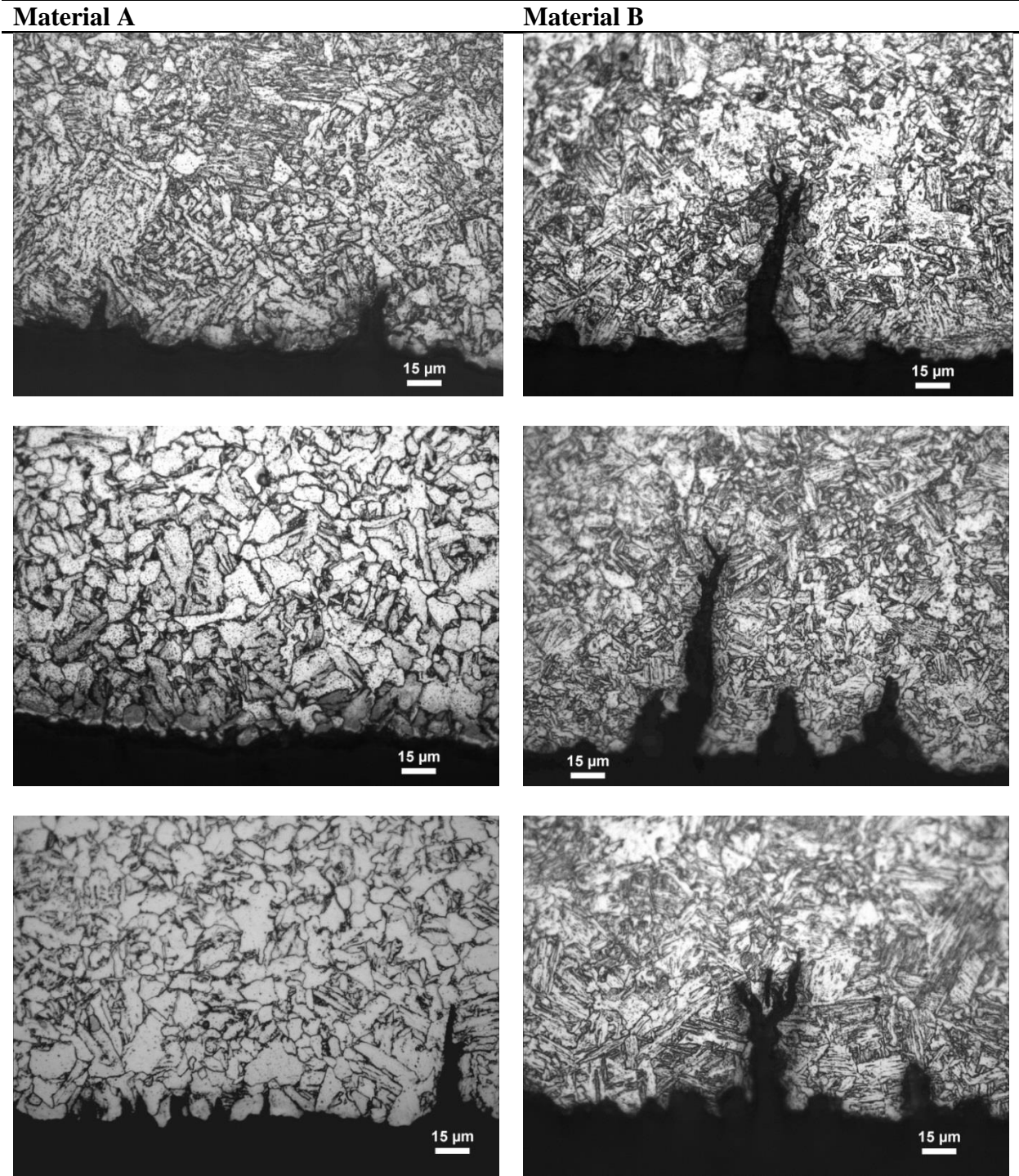


Table G-3: Micrographs of all FPB specimens of the HAZ of material A and B in test 1.

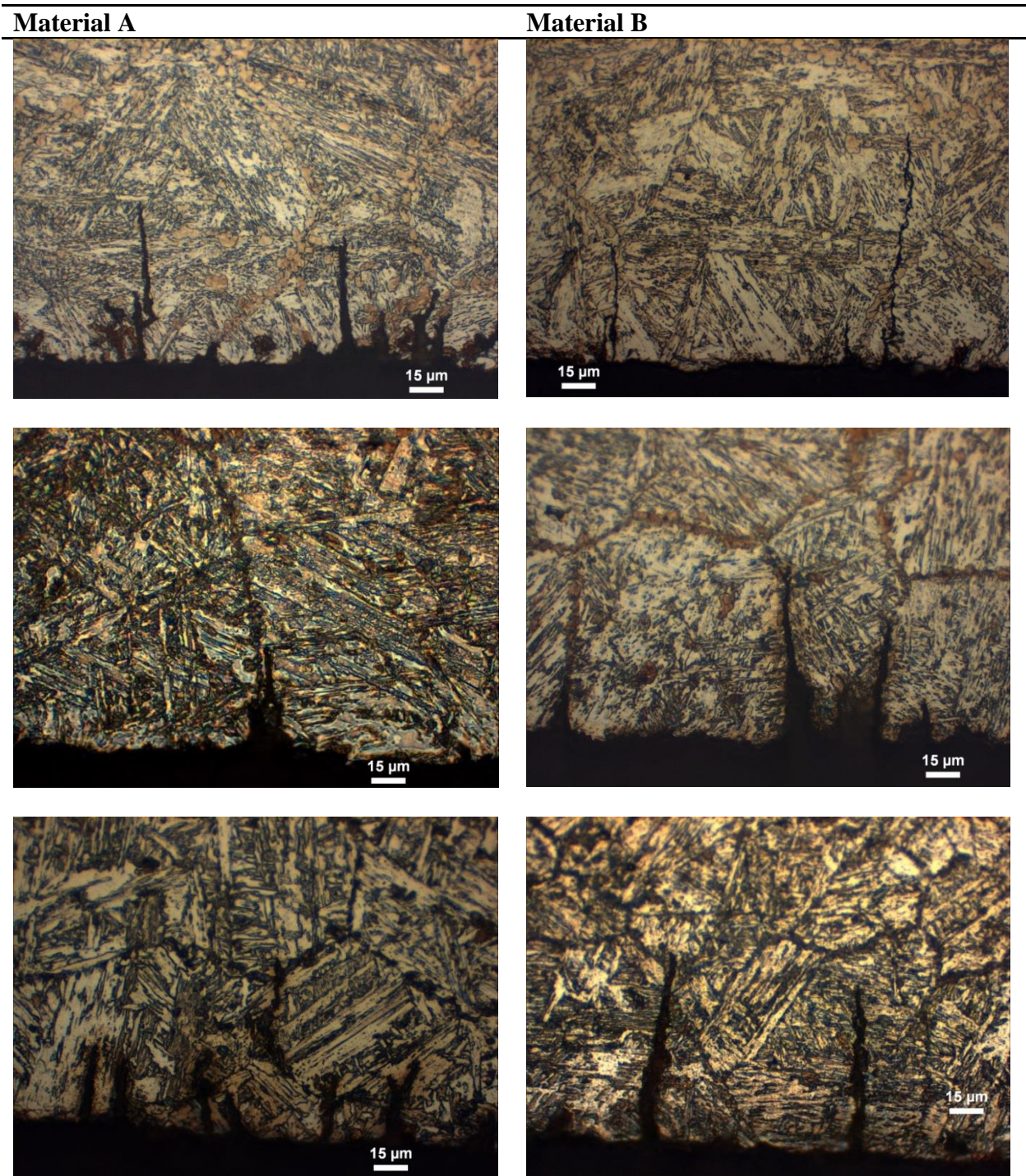


Table G-4: Micrographs of all FPB specimens of base material A and B in test 2.

